A STUDY OF SOLID-VAPOR EQUILIBRIUM IN THE HELIUM-KRYPTON AND HELIUM-XENON BINARY SYSTEMS

By

FREDERICK HENRY KATE, JR.

Bachelor of Science
Oklahoma State University
Stillwater, Oklahoma
1966

Master of Science
Oklahoma State University
Stillwater, Oklahoma
1968

Submitted to the Faculty of the Graduate College
of the Oklahoma State University
in partial fulfillment of the requirements
for the Degree of
DOCTOR OF PHILOSOPHY
May, 1972

A STUDY OF SOLID-VAPOR EQUILIBRIUM IN THE HELIUM-KRYPTON AND HELIUM-XENON BINARY SYSTEMS

Thesis Approved:

Robert S. Robinson, Jr.
Thesis Adviser

Leonard M. Raff

John B. West

B. L. Crynes

D. Durham
Dean of the Graduate College

PREFACE

An apparatus was constructed for making solid-vapor and liquid-vapor equilibrium measurements over a temperature range of 90 to 300° K. and a pressure range of 0 to 150 atm. Solid-vapor equilibrium measurements were made at temperatures of 90, 95, 100, 105, 110, and 115° K. for the helium-krypton system and temperatures of 120, 130, 140, and 155° K. for the helium-xenon system. A pressure range of 10 to 120 atm. was covered for both systems. Second interaction virial coefficients were determined from the experimental data and compared with data of other investigators. Combining rules for predicting interaction intermolecular potential parameters were tested using all the available second interaction virial coefficient data for the two systems studied in this work.

I am deeply indebted to my thesis adviser, Dr. R. L. Robinson, Jr., for his patient and intelligent guidance, his willing helpfulness, and his continued interest in the project. Discussions with other faculty members and my fellow graduate students, especially Mr. J. W. Coryell, were also of considerable help.

A special note of thanks is due Dr. M. J. Hiza of the National Bureau of Standards at Boulder, Colorado, and Dr. J. J. Martin of the Department of Physics at Oklahoma State University for information and assistance received during the construction of the experimental apparatus.

Financial support and equipment funds for the duration of the project were gratefully received from the National Science Foundation (Grant No. GK-2807) and the School of Chemical Engineering. The United States Bureau of Mines generously donated the high purity helium used in this work.

Finally, I cannot fully express the tremendous debt of gratitude that I owe to my wife, Ann, and to my parents for their constant support and encouragement throughout my entire graduate studies.

TABLE OF CONTENTS

LIST OF TABLES

LIST OF FIGURES

Figure Page

CHAPTER I

INTRODUCTION

Numerous advances in solution thermodynamics have been made in recent years including several theoretical means of describing gaseous and liquid mixtures from a molecular standpoint. All transport and equilibrium properties of both pure substances and mixtures can be determined from an accurate knowledge of the intermolecular interactions among the molecules within the system.

In pure substances, only interactions between like molecules occur, whereas in mixtures, unlike molecular interactions occur in addition to like interactions. Unfortunately, no really satisfactory means is available for determining the unlike molecule pair potential of even the most simple molecular pairs. Even when the pure species obey classical or quantum-mechanical corresponding state behavior, no existing theory has proven completely successful in predicting interaction pair potentials from known properties of the constituent molecules. Before progress can be made in predicting mixture properties from molecular considerations, improved mixing rules for predicting interaction intermolecular potential parameters must be developed.

The development and testing of interaction pair potential models are presently hindered by a lack of appropriate data. One suitable kind of data for this type of study is interaction virial coefficient data. However, much of the existing virial data has been taken on

systems containing components possessing polar or nonsymmetrical potentials. These effects complicate conclusions as to whether a theory is basically inadequate or has simply been applied to a system where the theoretical assumptions have been violated. Therefore, data on binary rare gas mixtures would be helpful because the assumption of a spherically-symmetrical potential is valid for the pure components.

In order to determine meaningful intermolecular potential parameters from interaction virial coefficients, data over a wide temperature range are necessary. Because conventional PVT methods are not applicable at low reduced temperatures, other methods must be used to determine interaction virial data at these temperatures. One quite simple and useful technique is solid-vapor equilibrium data, where the condensed phase may be considered to be essentially pure.

Therefore, the specific goals of this work were

(1) to design and build a cryostat and phase equilibrium cell which could be used to make both solid-vapor and liquid-vapor equilibrium measurements over a temperature range of 90 to 300° K and a pressure range of 0 to 150 atm.,

(2) to make solid-vapor equilibrium measurements on the helium-krypton and helium-xenon binary systems,

(3) to determine second interaction virial coefficients from the solid-vapor equilibrium data using conventional techniques, and

(4) to determine intermolecular potential parameters from the second interaction virial coefficients and use these parameters to test existing mixing rules.

In the following chapters, the procedures used to accomplish these goals and the results of this study are presented.

CHAPTER II

REVIEW OF PREVIOUS WORK

A complete survey of all solid-vapor equilibrium measurements has been presented previously by Hiza (21). Of particular interest to this work are solid-vapor equilibrium measurements on binary rare gas systems. Mullins and Ziegler (43) made both solid-vapor and liquid-vapor equilibrium measurements on the helium-argon system over a temperature range of 68 to 108° K and a pressure range of 20 to 120 atmospheres. Ewald (13) studied the helium-xenon system at 155° K over a pressure range of 4 to 108 atmospheres. Co-currently with this work, Hiza and co-workers have made both solid-vapor and liquid-vapor equilibrium measurements on the helium-krypton system (28) and the neon-krypton system (41) over a temperature range of 100 to 150° K and a pressure range of 3 to 120 atmospheres. These investigators have reported that, in general, their composition analyses have an imprecision of ± 2 or 3% in the mole fraction of the trace component of the binary vapor mixture.

Also of interest to this work are experimental second interaction virial coefficients on the helium-krypton and helium-xenon binaries. Brewer (2) has reported second interaction virial coefficient data for all ten of the binary mixtures of the rare gases helium through xenon. In Brewer's work, the quantity actually measured was the excess virial coefficient,

$$E = B_{12} - (B_{11} + B_{22})/2 \qquad (1)$$

The excess virial coefficient of Equation (1) was determined by a differential technique which involves measurement of the pressure change that accompanies the mixing of two gases at constant temperature and volume. Brewer reported an imprecision in his measurements of the excess virial coefficient of ± 0.1 cc/g mole.

A knowledge of reliable pure component virial coefficient data is necessary to determine the interaction virial coefficient, B_{12}, from the experimentally determined values of E. Brewer reported second interaction virial coefficients for the helium-krypton system at six different temperatures between -125° and 50° C, and for the helium-xenon system at five different temperatures between -100° and 50° C.

Recently, second interaction virial coefficients were determined for the helium-krypton system at temperatures of -50°, 0°, and 50°C in this laboratory by Dillard (11). These interaction virials were obtained from PVT measurements made using a Burnett-type apparatus. Dillard's interaction virials have an estimated imprecision of approximately ± 1 cc/g mole.

CHAPTER III

THEORETICAL CONSIDERATIONS

In this chapter, the equations necessary for the reduction of solid-vapor equilibrium data to obtain interaction virial coefficients are developed. A discussion of the combination rules to be tested for predicting interaction intermolecular potential parameters is also presented.

Data Reduction

The criteria for solid-vapor equilibrium in a binary system may be written as

$$\hat{f}_{2V} = \hat{f}_{2S}$$

where $\hat{f}_{2V}$ = fugacity of component "2" in the vapor phase

$\hat{f}_{2S}$ = fugacity of component "2" in the solid phase

and component "2" is the less volatile component. If the solid phase is assumed to be essentially pure, then the fugacity of component "2" in the solid phase is equal to the pure component fugacity of the solid at the temperature and pressure of the system, f_{2S}. Therefore,

$$\hat{f}_{2V} = f_{2S} \tag{2}$$

The fugacity of a pure component in the solid phase may be expressed as

$$\ln(f_{2S}/f_{2S}^{V.P.}) = (1/RT) \int_{P_2^o}^{P} \bar{V}_{2S}\, dP \tag{3}$$

where P_2^o = vapor pressure of pure component "2"

$\bar{V}_{2S}$ = solid molar volume of pure component "2"

$f_{2S}^{V.P.}$ = fugacity of solid component "2" at its vapor pressure

P = system pressure.

For a pure component below its triple point

$$f_{2S}^{V.P.} = f_{2V}^{V.P.} \tag{4}$$

The pure component vapor fugacity of component "2" is given by

$$\ln(f_{2V}^{V.P.}/P_2^o) = (1/RT) \int_0^{P_2^o} [\bar{V} - \frac{RT}{P}]\, dP \tag{5}$$

Combining Equations (3), (4) and (5) yields

$$\ln(f_{2S}/P_2^o) = (1/RT) \int_{P_2^o}^{P} \bar{V}_{2S}\, dP + (1/RT) \int_0^{P_2^o} [\bar{V} - RT/P]\, dP \tag{6}$$

In the solution of Equation (6) in this work, $\bar{V}_{2S}$ is assumed to be independent of pressure and the Berlin form of the virial equation is applied to the vapor phase. The Berlin form of the virial equation is given by

$$Z = 1 + B'P + C'P^2 + \ldots$$

which can be rearranged to

$$\bar{V} = RT/P + B'RT + C'RTP + \ldots \tag{7}$$

Substituting Equation (7) truncated after the second virial term (valid because P_2^o is very low) into Equation (6) and integrating we obtain

$$\ln(f_{2S}/P_2^o) = \bar{V}_{2S}(P - P_2^o)/RT + B_{22}P_2^o/RT \tag{8}$$

The fugacity of component "2" in the vapor phase is given by

$$\ln (\hat{f}_{2V}/Py_2) = (1/RT) \int_V^\infty [(\partial P/\partial n_2)_{T,V,n_1} - RT/V] \, dV - \ln Z \quad (9)$$

where n_1, n_2 = moles of component "1" and component "2", respectively

y_2 = mole fraction of component "2".

Assuming that the Leiden form of the virial equation truncated after the third virial term applies to the vapor phase, i.e.,

$$Z = 1 + B/\bar{V} + C/\bar{V}^2 + \ldots$$

or

$$P = nRT/V + n^2BRT/V^2 + n^3CRT/V^3 + \ldots$$

Then $(\partial P/\partial n_2)_{T,V,n_1}$ may be evaluated from the virial equation

where $$B = \frac{n_1^2B_{11} + 2n_1n_2B_{12} + n_2^2B_{22}}{(n_1 + n_2)^2}$$

and

$$C = \frac{n_1^3C_{111} + 3n_1^2n_2C_{112} + 3n_1n_2^2C_{122} + n_2^3C_{222}}{(n_1 + n_2)^3}$$

Thus

$$(\partial P/\partial n_2)_{T,V,n_1} = RT/V - (2n_1B_{12} + 2n_2B_{22})(RT/V^2) + (3n_1^2C_{112} + 6n_1n_2C_{122} + 3n_2^2C_{222})(RT/V^3) \quad (10)$$

Substituting Equation (10) into Equation (9) and integrating yields

$$\ln (\hat{f}_{2V}/Py_2) = (2y_1B_{11} + 2y_2B_{22})/\bar{V}_m + (3y_1^2C_{112} + 6y_1y_2C_{122} + 3y_2^2C_{222})/2\bar{V}_m^2 - \ln Z_m \quad (11)$$

where $\bar{V}_m$ = molar volume of gas mixture

Z_m = compressibility factor of gas mixture

Combining Equations (2), (8), and (11), we obtain

$$\ell n\ (f_{2S}/P_2^o) - \ell n\ (\hat{f}_{2V}/Py_2) = \ell n\ (Py_2/P_2^o) \equiv \ell n\ \phi_2$$

where Py_2/P_2^o is defined to be the enhancement factor, ϕ_2, of component "2". Thus

$$\ell n\ \phi_2 = \bar{V}_{2S}(P - P_2^o)/RT + B_{22}P_2^o/RT + \ell n\ Z_m \qquad (12)$$

$$- (2y_1B_{12} + 2y_2B_{22})/\bar{V}_m - (3y_1^2C_{112} + 6y_1y_2C_{122} + 3y_2^2C_{222})/2\bar{V}_m^2$$

Equation (12) is one of the basic data reduction equations used in this work. For consistency, Z_m and $\bar{V}_m$ must be determined from the virial equation. The regression of the interaction virial coefficients, B_{12} and C_{112}, from Equation (12) requires an iterative procedure which will be discussed in more detail in a later chapter.

If the vapor phase is assumed to be essentially pure (i.e., $y_1 \to 1$, $y_2 \to 0$, $Z_m \to Z_1$, and $\bar{V}_m \to \bar{V}_1$), then Equation (12) reduces to

$$\ell n\ \phi_2 = \bar{V}_{2S}(P - P_2^o)/RT + B_{22}P_2^o/RT + \ell n\ Z_1$$

$$- 2B_{12}/\bar{V}_1 - 3C_{112}/2\bar{V}_1^2 \qquad (13)$$

The interaction virial coefficients, B_{12} and C_{112}, can be obtained from Equation (13) by a straightforward linear regression requiring no iteration. Unfortunately, Equation (13) is not applicable for data taken at temperatures close to the triple point of component "2" because the vapor phase can no longer be considered pure due to the higher concentrations of component "2" in it. The historical development of the

above equations is given in a review by Rowlinson and Richardson (52).

Chiu and Canfield (7) have used a similar analysis to develop the following equation:

$$(1/y_1^2P)[RT\ \ell n\ \phi_2 - \bar{V}_{2S}(P - P_2^o) + (1 - y_1^2)B_{22}P - B_{22}P_2^o - (C_{222} - B_{22}^2)(P_2^o)^2/2RT]$$

$$= (B_{11} - 2B_{12}) + (P/2RTy_1^2)\,[-3C_{112}y_1^2 - 6C_{122}y_1y_2 - 3C_{222}y_2^2$$

$$+ (2C_{111} + 4B_{11}B_{12})y_1^3 + (6C_{112} + 8B_{12}^2 + 4B_{11}B_{12})y_1^2y_2 \qquad (14)$$

$$+ (12B_{12}B_{22} + 6C_{222})y_1y_2^2 + (2C_{222} + 4B_{22}^2)y_2^3 - 3B_{11}^2y_1^4$$

$$- 12\,B_{11}B_{12}y_1^3y_2 - (12B_{12}^2 + 6B_{11}B_{22})y_1^2y_2^2 - 12B_{22}B_{12}y_1y_2^3 - 3B_{22}^2y_2^4]$$

where the following assumptions apply:

(1) the solid phase is essentially pure;

(2) $\bar{V}_{2S}$ is independent of pressure;

(3) the virial equation truncated after two virial terms is adequate to describe the vapor phase.

The basic difference between Equations (12) and (14) is that in Equation (14) the fugacity of component "2" in the vapor phase, $\hat{f}_{2V}$, was determined from the pressure explicit expression rather than the volume explicit expression presented in Equation (9).

If the left-hand side of Equation (14) is defined as

$$ERT \equiv (1/y_1^2P)[RT\ \ell n\ \phi_2 - \bar{V}_{2S}(P - P_2^o) + (1 - y_1^2)B_{22}P - B_{22}P_2^o$$

$$- (C_{222} - B_{22}^2)(P_2^o)^2/2RT] \qquad (15)$$

then we can write Equation (14) in the form

$$ERT = (B_{11} - 2B_{12}) + \bar{F}P \qquad (16)$$

where F is a function of composition and the virial coefficients. A tempting procedure would be to extrapolate a plot of ERT versus pressure to zero pressure to obtain $(B_{11} - 2B_{12})$, but this is invalid because two-phase equilibrium cannot exist below the vapor pressure of component "2". Therefore, the plot of ERT versus P must be extrapolated to some pressure equal to or above P_2^o. Chiu and Canfield suggested that an optimum extrapolation pressure, P_{oe}, be used. This pressure is defined as that pressure at which the absolute value of FP/ERT is a minimum subject to the restriction, $P_{oe} \geq P_2^o$. Thus, Equation (16) represents a simple graphical technique of analyzing solid-vapor equilibrium data to obtain the second interaction virial coefficient. This technique will be considered in more detail in a later chapter.

Discussion of Combination Rules for Interaction Intermolecular Potential Parameters

The combination rules to be tested in this work are presented in Table I. The theoretical bases for these rules have been discussed in some detail by other investigators (14, 49).

The commonly used, semi-empirical form of intermolecular potential between two molecules is given by

$$U(r) = - A/r^n + C/r^m \tag{17}$$

where the A/r^n is the attractive force term of the potential and C/r^m is the repulsive force term. Although considerable theoretical work has provided valuable information on the specific portions of the potential (1, 10, 48, 49), empirical models are still required for the complete description of the potential curve. One commonly used empirical form is the Lennard-Jones 12-6 potential (33),

TABLE I

COMBINATION RULES FOR THE INTERACTION ENERGY PARAMETER ε_{ij}

Rule No.	Rule	Reference
I	$\varepsilon_{ij} = (\varepsilon_{ii}\varepsilon_{jj})^{\frac{1}{2}}$	17, 50
II	$\varepsilon_{ij} = 2\varepsilon_{ii}\varepsilon_{jj}/(\varepsilon_{ii} + \varepsilon_{jj})$	14
III	$\varepsilon_{ij} = (\varepsilon_{ii}\sigma_{ii}^6\varepsilon_{jj}\sigma_{jj}^6)^{\frac{1}{2}}(1/\sigma_{ij}^6)$	51
IV	$\varepsilon_{ij} = (\varepsilon_{ii}\sigma_{ii}^3\varepsilon_{jj}\sigma_{jj}^3)^{\frac{1}{2}}(1/\sigma_{ij}^3)$	51
V	$\varepsilon_{ij} = (\varepsilon_{ii}\varepsilon_{jj})^{\frac{1}{2}}(\sigma_{ii}\sigma_{jj}/\sigma_{ij}^2)^3[2(I_iI_j)^{\frac{1}{2}}/(I_i + I_j)]$	26
VI	$\varepsilon_{ij} = [2\varepsilon_{ii}\varepsilon_{jj}/(\varepsilon_{ii} + \varepsilon_{jj})](\sigma_{ii}\sigma_{jj}/\sigma_{ij}^2)^6 \times \left[\frac{(\varepsilon_{ii} + \varepsilon_{jj})\sigma_{ij}^6/\chi_i\chi_j}{(\varepsilon_{ii}\sigma_{ii}^6/\chi_i^2 + \varepsilon_{jj}\sigma_{jj}^6/\chi_j^2)}\right]$	38
VII	$\varepsilon_{ij} = [2\varepsilon_{ii}\varepsilon_{jj}/(\varepsilon_{ii} + \varepsilon_{jj})](\sigma_{ii}\sigma_{jj}/\sigma_{ij}^2)^6 \times \left[\frac{(\varepsilon_{ii} + \varepsilon_{jj})\sigma_{ij}^6/\alpha_i\alpha_j}{(\varepsilon_{ii}\sigma_{ii}^6/\alpha_i^2 + \varepsilon_{jj}\sigma_{jj}^6/\alpha_j^2)}\right]$	42
VIII	$\varepsilon_{ij} = (\varepsilon_{ii}\varepsilon_{jj})^{\frac{1}{2}}[4I_iI_j/(I_i + I_j)^2] \times \left\{\frac{[(\frac{1}{6}k_iI_i\sigma_{oii}^{12} + \frac{3}{4}I_i\alpha_i^2\sigma_{oii}^6)(\frac{1}{6}k_jI_j\sigma_{ojj}^{12} + \frac{3}{4}I_j\alpha_j^2\sigma_{ojj}^6)]^{\frac{1}{2}}}{2^{-13}[(\frac{1}{6}k_iI_i\sigma_{oii}^{12})^{1/13} + (\frac{1}{6}k_jI_j\sigma_{ojj}^{12})^{1/13}]^{13} + \frac{3}{2}[I_iI_j/(I_i + I_j)]\alpha_i\alpha_j\sigma_{oij}^6}\right\}$	56

ε = energy parameter

σ, σ_o = distance parameters (where $\sigma_o \simeq \sigma/4$)

I = ionization potential

χ = diamagnetic susceptibility

α = static polarizability

k = empirical constant

$$U(r) = 4\varepsilon[(\sigma/r)^{12} - (\sigma/r)^{6}] \tag{18}$$

where

$$A = 4\varepsilon\sigma^{6} \tag{19a}$$

$$C = 4\varepsilon\sigma^{12} \tag{19b}$$

and ε and σ are the intermolecular energy and distance parameters, respectively.

If the attractive potential term constant, A, is expressed in terms of the London theory (36) of the dispersion force, then

$$A_{ii} = \frac{3}{4}\alpha_i^2 I_i \; ; \; A_{ij} = \frac{3}{2}\alpha_i\alpha_j[I_iI_j/(I_i + I_j)] \tag{20}$$

where α is the static polarizability and I is the ionization potential. The static polarizabilities can be eliminated from Equation (20) by combining the A's in the following manner.

$$A_{ij}/(A_{ii}A_{jj})^{\frac{1}{2}} = 2(I_iI_j)^{\frac{1}{2}}/(I_i + I_j) \tag{21}$$

By combining Equations (19a) and (21), an expression suggested by Hudson and McCoubrey (26) is obtained.

$$\varepsilon_{ij} = (\varepsilon_{ii}\varepsilon_{jj})^{\frac{1}{2}}(\sigma_{ii}\sigma_{jj}/\sigma_{ij}^2)^3[2(I_iI_j)^{\frac{1}{2}}/(I_i + I_j)] \tag{22}$$

which is Rule V in Table I. Rules I and III are direct simplifications of Rule V. Rule III is obtained by assuming $I_i \simeq I_j$ and Rule I is obtained by further assuming that $\sigma_{ii} \simeq \sigma_{jj}$. Rule IV is an empirical modification of Rule III.

An equally valid basis for developing combining rules is to use the Kirkwood-Muller theory (30) by equating the attractive form of the Lennard-Jones 12-6 potential to the K-M formula.

$$A_{ii} = 3mc^2\alpha_i\chi_{ij}; \quad A_{ij} = 6mc^2\alpha_i\alpha_j/(\alpha_i/\chi_i + \alpha_j/\chi_j) \tag{23}$$

where χ is the diamagnetic susceptibility, m is the electronic mass, and c is the velocity of light. A combining rule independent of the static polarizability and consistent with Equation (23) is given by

$$A_{ij} = 2A_{ii}A_{jj}/[(\chi_j/\chi_i)A_{ii} + (\chi_i/\chi_j)A_{jj}] \tag{24}$$

By combining Equations (19a) and (24),

$$\varepsilon_{ij} = (2\varepsilon_{ii}\varepsilon_{jj}/\chi_i\chi_j)(\sigma_{ii}\sigma_{jj}/\sigma_{ij})^6/(\varepsilon_{ii}\sigma_{ii}^6/\chi_i^2 + \varepsilon_{jj}\sigma_{jj}^6/\chi_j^2) \tag{25}$$

which can be expanded to

$$\varepsilon_{ij} = [2\varepsilon_{ii}\varepsilon_{jj}/(\varepsilon_{ii}+\varepsilon_{jj})](\sigma_{ii}\sigma_{jj}/\sigma_{ij}^2)^6\left[\frac{(\varepsilon_{ii} + \varepsilon_{jj})\sigma_{ij}^6/\chi_i\chi_j}{(\varepsilon_{ii}\sigma_{ii}^6/\chi_i^2 + \varepsilon_{jj}\sigma_{jj}^6/\chi_j^2)}\right] \tag{26}$$

Equation (26) is Rule VI in Table I and Rule II is a direct simplification for which the following assumptions apply: $\sigma_{ii} \simeq \sigma_{jj}$ and $\chi_i \simeq \chi_j$.

A combining rule that is consistent with both the London and Kirkwood-Muller approximations is given by

$$A_{ij} = 2A_{ii}A_{jj}/[(\alpha_j/\alpha_i)A_{ii} + (\alpha_i/\alpha_j)A_{jj}] \tag{27}$$

This expression was originally proposed by Moelwyn-Hughes (42) and has been recently tested by Kramer and Herschbach (31). Substituting Equation (19a) into Equation (27) yields

$$\varepsilon_{ij} = (2\varepsilon_{ii}\varepsilon_{jj}/\alpha_i\alpha_j)(\sigma_{ii}\sigma_{jj}/\sigma_{ij})^6/(\varepsilon_{ii}\sigma_{ii}^6/\alpha_i^2 + \varepsilon_{jj}\sigma_{jj}^2/\alpha_j^2) \tag{28}$$

which can be rearranged to

$$\varepsilon_{ij} = [2\varepsilon_{ii}\varepsilon_{jj}/(\varepsilon_{ii} + \varepsilon_{jj})](\sigma_{ii}\sigma_{jj}/\sigma_{ij}^2)^6 \times \left[\frac{(\varepsilon_{ii} + \varepsilon_{jj})\sigma_{ij}^6/\alpha_i\alpha_j}{(\varepsilon_{ii}\sigma_{ii}^6/\alpha_i^2 + \varepsilon_{jj}\sigma_{jj}^6/\alpha_j^2)} \right] \quad (29)$$

Equation (29) is Rule VII in Table I and can be reduced to Rule II by assuming $\sigma_{ii} \simeq \sigma_{jj}$ and $\alpha_i \simeq \alpha_j$.

Rules I through VII were derived by considering only the attractive force term of the intermolecular potential function. Recently, however, Sikora (56) has proposed a combining rule (Rule VIII) for which both the attractive and the repulsive terms of the intermolecular potential are considered. The London theory is applied to the attractive force term of the potential and the repulsive force term is associated with the energy of the distortion of the outermost electron shell of a molecule. From the nature of the derivation of Rule VIII, the expression of Hudson-McCoubrey (Rule V) should be a limiting case. This is true if the k's in Rule VIII vanish and σ_o is replaced by σ which produces no numerical changes since σ_o/σ does not vary significantly from system to system.

An empirical mixing rule for the interaction energy parameter is

$$\varepsilon_{ij} = (1 - k_{ij})(\varepsilon_{ii}\varepsilon_{jj})^{\frac{1}{2}} \quad (30)$$

where k_{ij} is the "geometric-mean correction factor" and is directly obtainable from experimental data. Recently, Hiza and Duncan (22) have proposed an empirical correlation for k_{ij}, which is given by

$$k_{ij} = 0.17(I_i - I_j)^{\frac{1}{2}}\ln(I_i/I_j) \quad (31)$$

In order to test the combining Rules III through VII, some know-

ledge of the interaction distance parameter, σ_{ij}, is necessary. Either the experimental value of σ_{ij} must be used, or some combining rule to obtain σ_{ij} from the pure component parameters must be assumed. One commonly used mixing rule is the "hard-sphere" model.

$$\sigma_{ij} = \frac{1}{2}(\sigma_{ii} + \sigma_{jj}) \tag{32}$$

but recently Good and Hope (15) have proposed the rule

$$\sigma_{ij} = (\sigma_{ii}\sigma_{jj})^{\frac{1}{2}} \tag{33}$$

with the contention that this rule is more physically sound than the "hard-sphere" model. All three of these means for obtaining σ_{ij} will be used in this work when testing the combining rules in Table I.

CHAPTER IV

EXPERIMENTAL APPARATUS

The experimental apparatus of several investigators (23, 29, 40, 57) who have made solid-vapor equilibrium measurements were carefully considered before the apparatus used in this study was designed.

A cryostat quite similar to that of Hiza and Herring (23) was designed and constructed to fulfill the following requirements:

(1) the operating temperature range of the equilibrium cell should be 90° to 300° K (the lower temperature limit was set by the fact that 90° K is the lowest temperature at which good temperature control of the cell could be maintained using atmospheric liquid nitrogen cooling);

(2) the pressure range of the equilibrium cell should be 0 to 150 atm.;

(3) the cell assembly should be applicable to both liquid-vapor and solid-vapor equilibrium studies.

General Description

The detailed arrangement of the phase equilibrium cell is presented in Figure 1. Essentially, the equilibrium cell (A) is a large hollow copper block which contains a removable section of five equilibrium trays (C) packed with steel wool. The cell is charged with the component to be solidified through a fill line [1] at the top of the cell

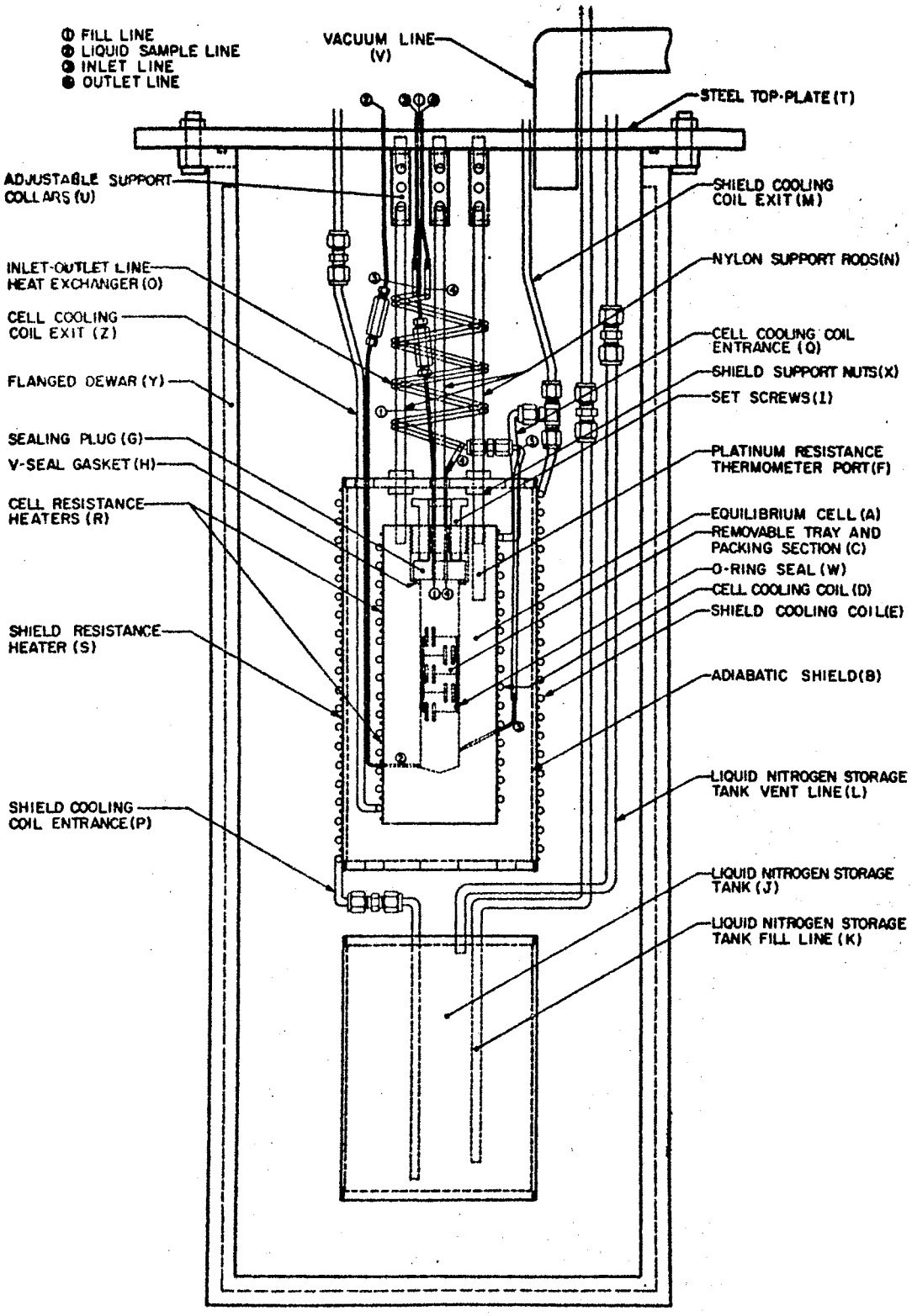

Figure 1. Schematic Diagram of the Phase Equilibrium Cell

cavity. The lighter gaseous component enters the cell cavity through an inlet line [3] near the bottom of the cell and is removed from an exit line [4] at the top of the cell cavity adjacent to the fill line [1]. The other transfer line attached to the cell is located at the very bottom of the cell cavity and can be used as a liquid sample line [2] in studies of liquid-vapor equilibrium.

The cell is wrapped from top to bottom with a cooling coil (D) and insulated resistance heating wires (R). Two resistance thermometers are situated in the top of the cell. One is a platinum resistance thermometer for measuring temperature and the other serves as the probe for the temperature control unit. The ends of a differential thermocouple are located at the top and bottom of the cell.

An adiabatic shield (B) which is also wrapped with a cooling coil (E) and heating wire (S) surrounds the cell. The purpose of the adiabatic shield is to minimize the heat losses from the cell due to convection and radiation to the surroundings of the cryostat. In this manner, the amount of input cooling and heating necessary to maintain temperature control of the cell could be minimized. The entire cell and shield assembly are supported from the top-plate (T) of the cryostat by three nylon rods (N).

A liquid nitrogen storage vessel (J) is located at the bottom of the cryostat. This storage vessel is supported by its inlet, exit, and vent lines. A heat exchanger (O) is situated above the cell which is used for the countercurrent exchange of heat between the inlet and outlet vapor streams.

A stainless steel dewar (Y) flanged to the supporting top-plate of the cryostat encloses the entire cell assembling. The dewar can be

evacuated through a vacuum line (V) in the top plate. Vacuum serves as a very good insulation because convection and conduction from the cell assembling to the surroundings of the cryostat are quite small in a system which is evacuated below a pressure of 10^{-5} torr. The liquid nitrogen storage tank and adiabatic shield are wrapped with aluminum foil and the entire cell assembled is surrounded with a radiation shield of aluminum foil to minimize the radiant heat transfer.

A schematic diagram of the entire phase equilibrium equipment is presented in Figure 2. The equipment contains several key features, all of which will be discussed in detail later. The main component of the equipment is the cryostat and phase equilibrium cell which has already been mentioned. Another feature is the vapor flow system which includes all the pressure measuring and pressure control apparatus.

A third element of the phase equilibrium equipment is the gas analysis system in which an ultrasonic detector is utilized to analyze the vapor phase. This relatively new means of gas analysis proved quite successful in this work. Other features of the equipment include the shield and cell cooling control system, the cell temperature control unit, the liquid nitrogen transfer system, and the insulating vacuum system.

Equilibrium Cell Description

The phase equilibrium cell (A) was prepared from a solid copper rod 9 inches long and 3 inches in diameter. A cavity $6\frac{1}{2}$ inches long and 1 inch in diameter was drilled out of the center of the cell. At the top of the cell, the cavity was enlarged to $1\frac{1}{2}$ inches in diameter. The cavity was extended to a depth of $1\frac{1}{2}$ inches and was threaded to a

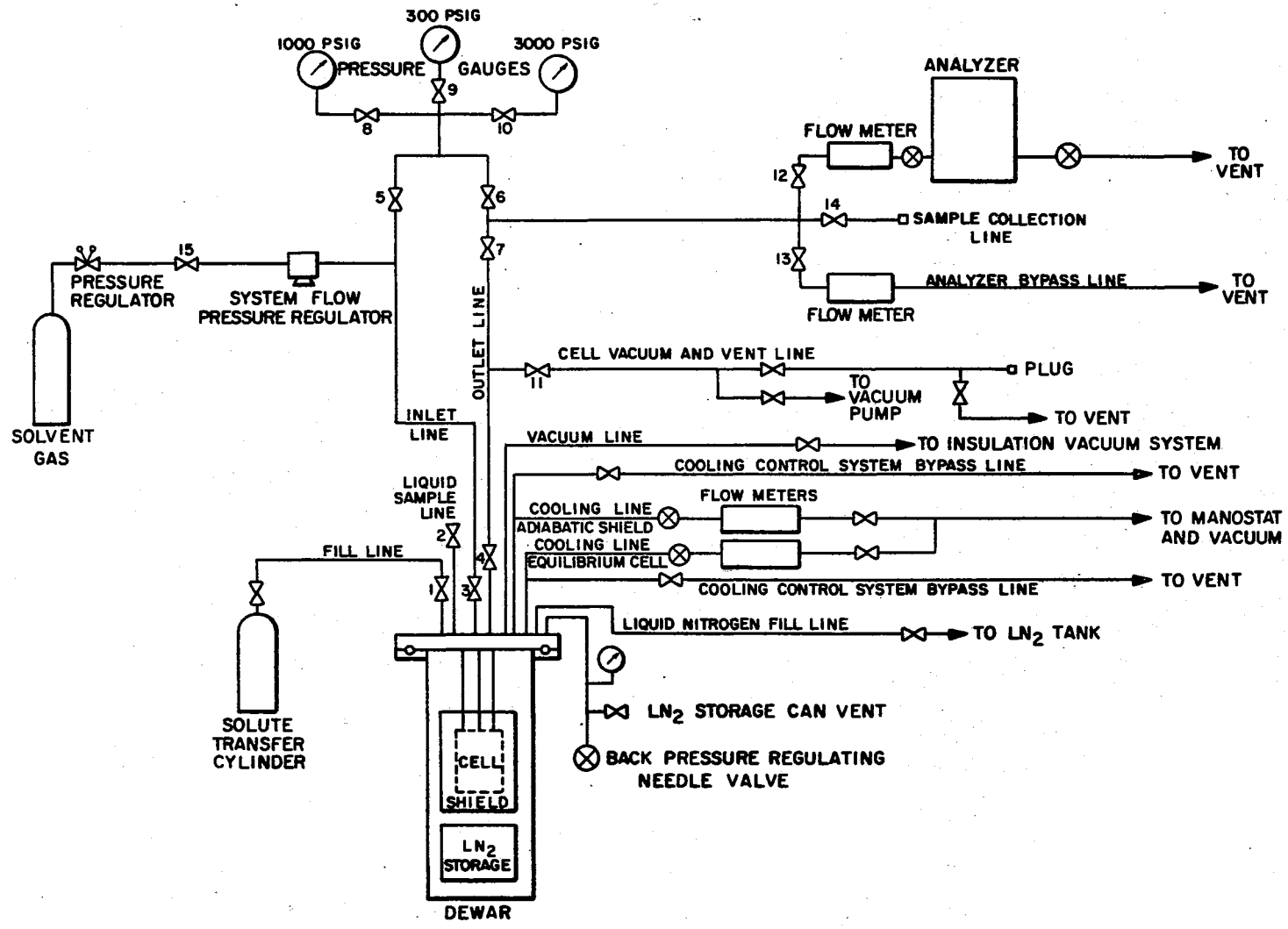

Figure 2. Schematic Diagram of the Phase Equilibrium Equipment

depth of approximately $1\frac{1}{4}$ inches.

As shown in Figure 1, the cell is sealed by a gasket, plug, and set screw assembling. A $\frac{3}{4}$-inch brass rod $1\frac{1}{2}$ inches in diameter was threaded and a $\frac{1}{2}$-inch hole was drilled through its center. Three $\frac{1}{4}$-inch bolt holes, evenly spaced, were drilled and threaded in the remainder of the brass rod. A solid copper plug (G) $\frac{1}{2}$-inch thick by $1\frac{3}{8}$ inches in diameter was used in conjunction with the brass plug and three $\frac{1}{4}$-inch brass bolts to produce a compressive force on the gasket. The brass bolts serve as set screws (I). The gasket (H) used in this work is a Parker Metal V-Seal made of inconel coated with Teflon. The gasket has a nominal O.D. of $1\frac{1}{4}$ inches, a nominal I.D. of $1\frac{1}{16}$ inches, and a free height of 0.089 to 0.092 inch. The compresion seal obtained by the above means performed satisfactorily under both high pressures and extreme temperature cycling.

At the top of the cell, five vertical ports were drilled in the cell and are located between the outside edge of the cell and the cell cavity. Three of these holes are $\frac{1}{4}$-inch in diameter and $\frac{1}{2}$-inch deep. They are threaded and serve as anchor holes for three threaded nylon rods (N) from which the entire cell and shield assemply is suspended from the top-plate of the cryostat. The two other holes serve as thermometer ports. One hole is $\frac{5}{16}$-inch in diameter, 2 inches deep and is used to house the platinum resistance thermometer (F). The other hole, located immediately adjacent to the above port, is $\frac{1}{8}$-inch in diameter, 2 inches deep, and houses the temperature control probe.

Four $\frac{1}{16}$-inch, 316 stainless-steel transfer lines are attached to the cell. The liquid sample line [2] and inlet gas line [3] enter the cell near the bottom of the cell cavity on opposite sides of the cell.

These lines were attached to the cell by first drilling $\frac{1}{16}$-inch holes into the cell cavity, inserting the tubes, heating the entire copper block, and soldering the tubes into place. The gas outlet line [4] and condensation fill line [1] are located adjacent to one another and enter the cell through the copper plug (G) that compresses the sealing gasket. These lines are attached by silver solder. The two lines in the cell itself were not silver soldered because heating the entire copper cell (approximate weight of 20 lbs.) to a high enough temperature to silver solder was not feasible.

The cell is wrapped with a copper cooling coil (D) which serves as a transfer line for the cooltant. The copper tubing is thin-walled and has a $\frac{3}{16}$-inch outside diameter. Approximately 15 evenly spaced (about $\frac{1}{2}$ inch apart) loops of tubing surround the cell. The entire cooling coil was fastened to the cell by soldering the inside of the tubing (in good thermal contact) to the cell. Again, the entire copper cell had to be heated to the melting temperature of the solder and care had to be taken that the two lines soldered in the base of the cell did not come loose.

The equilibrium cell is also wrapped with two lengths of asbestos insulated chromel A wire (B & S Gauge No. 24) to serve as small wattage resistance heaters (R). Each piece of wire is approximately 5 to 6 feet long and has a resistance of about 5 ohms. The wires were wrapped between the copper cooling coil loops and are located at the top and bottom of cell. The wires are held in position by epoxy resin.

A removable tray section (C) is located in the internal cavity of the cell. The trays are thin circular steel disks slightly smaller than 1 inch in diameter. Each tray was tapped with a $\frac{1}{4}$-inch hole so that a

$\frac{1}{2}$-inch long piece of $\frac{1}{4}$-inch O.D. tubing could be soldered into place in the tray. These tubing sections allow the vapor stream to pass through the tray section. The trays are separated by $\frac{1}{2}$-inch long tray spacers made from 1-inch O.D. steel tubing. The space between the trays is packed with steel wool. The entire tray section was assembled using a $\frac{1}{4}$-inch bolt to hold it together; then the trays and tray spacers are soldered in place. A groove was lathed around the bottom of the tray section in which a 1-inch O.D. neoprene O-ring (W) was positioned. The O-ring not only holds the tray section in place but also prevents vapor bypass around the trays.

A copper-constantan differential thermocouple was originally attached to the top and bottom of the cell. The purpose of the differential thermocouple in this position is to detect temperature gradients across the length of the cell. Later, the top bead of the thermocouple was attached to the vapor outlet line about 2 inches above the top of the cell. In this position, the differential thermocouple can be used to determine if the vapor outlet line temperature is above that of the cell. This is important because condensation from the equilibrium gas mixture leaving the top of the cell must be prevented in the vapor outlet line.

Adiabatic Heat Shield

Surrounding the equilibrium cell is an adiabatic heat shield (B) designed to minimize the flow of heat from the surroundings to the cell. This heat shield is a $10\frac{1}{2}$-inch long piece of 5-inch nominal, Type L, hard copper water pipe. The pipe has an O.D. of $5\frac{1}{8}$ inches and an I.D. of $4\frac{7}{8}$ inches. Two circular $\frac{1}{4}$-inch thick pieces of brass plate, 5

inches in diameter, were used for the top and bottom of the adiabatic shield.

A 1-inch diameter hole was drilled in the center of each plate and six $\frac{1}{2}$-inch diameter holes were evenly spaced around the center hole near the outer edge of the plate. The purpose of these holes is to allow the passage of the various lines and wires from the cell through the heat shield and to allow the evacuation of the annular space between the cell and the shield. Three $\frac{1}{4}$-inch diameter holes were also drilled in the top-plate of the shield. They were positioned to correspond exactly with the anchor holes on the top of the equilibrium cell. Thus, the heat shield can be supported with the three threaded nylon support rods (N) by using hex-headed nuts (X) on either side of the top-plate to hold it firmly in position.

The bottom-plate was soldered into place in the bottom of the shield. For convenience in assembly, however, the shield is supported from its top-plate using an anchor screw assembly. Three 1-inch long pieces of $\frac{3}{4}$-inch diameter hexagonal brass bar stock were tapped and threaded for $\frac{3}{16}$-inch screws. These pieces were then attached to the inside of the shield wall at regular intervals. Three $\frac{3}{16}$-inch holes were drilled in the top-plate of the shield. Thus, the shield can be suspended from the top-plate by screwing three $\frac{3}{16}$-inch round head screws through the top-plate into the three brass stock supports.

A cooling coil (E) of $\frac{3}{16}$-inch O.D. copper tubing was soldered to the outside of the shield. The cooling coil consists of approximately 20 loops spaced approximately $\frac{1}{2}$-inch apart. A chromel resistance heating wire (S) was wrapped between the loops of the cooling coil. The wire is 24 feet long, has a resistance of approximately 24 ohms, and

was attached to the shield with epoxy resin.

Liquid Nitrogen Storage Vessel

A supply vessel (J) for liquid nitrogen cooltant to the adiabatic heat shield and equilibrium cell is located immediately under the shield and cell assembly. This vessel was constructed from the same Type L copper water pipe that was used for the shield. Two circular 5-inch diameter pieces of $\frac{1}{4}$-inch thick copper plate were soldered into the grooved ends of a 7-inch long piece of the copper pipe to complete construction of the storage vessel.

Two $\frac{1}{4}$-inch O.D. and one $\frac{3}{16}$-inch O.D. transfer lines were soldered into the top of the vessel. One of the $\frac{1}{4}$-inch lines serves as a fill line (K) and the other serves as a vapor vent line (L). A pressure gauge with a range of 0 to 100 psig and a needle valve were placed in the vent line of the storage vessel where it exits the cryostat. The pressure gauge is used to monitor the pressure in the storage vessel and the needle valve serves as a back pressure regulator to prevent a pressure "build-up". The $\frac{3}{16}$-inch line (P) is the supply line to the shield and cell. The three transfer lines serve as the only support for the vessel. The capacity of the LN_2 storage vessel is approximately 2100 cc.

Miscellaneous Cryostat Components

The two $\frac{1}{16}$-inch stainless steel transfer lines coming out of the top of the cell are the condensate fill line [1] and vapor outlet line [4]. A thermal short of copper bar stock was soldered between them to prevent subcooling of the outlet line. Later, a resistance heating

wire was wrapped around these lines and their thermal short and epoxyed into place. The wire has a resistance of approximately 2 ohms and serves as added insurance against subcooling in the vapor exit line.

Above the shield and cell assembly is a heat exchanger (O) in which heat is exchanged between the inlet and outlet vapor streams. The exchanger was constructed by soldering together two parallel segments of $\frac{1}{8}$-inch O.D. copper tubing. The exchanger is helical in shape in order to conserve space and fit around the three nylon cell support rods. The ends of the exchanger were easily connected to the $\frac{1}{16}$-inch stainless steel inlet and outlet vapor lines because the $\frac{1}{16}$-inch tubing fit into the $\frac{1}{8}$-inch tubing and could be easily soldered.

The cell and shield assembly are held in place by three $\frac{1}{4}$-inch O.D. nylon rods (N) which are threaded their entire length with right-handed threads. They are made out of nylon in order to cut down the amount of heat transferred to the shield and cell by conduction.

These nylon support rods are attached to the top-plate of the cryostat by means of adjustable collars (U) which can be used not only to support the cell but to position it as well. Three $\frac{5}{16}$-inch holes were drilled and threaded into the cryostat's top-plate corresponding to the arrangement of the support rods. Three $\frac{5}{16}$-inch bolts were made by threading one end right-handed and the other end left-handed. The right-hand threaded side of the bolt was screwed into the top-plate leaving the left-hand threaded side facing the support rods which had $\frac{1}{4}$-inch right-handed threads. The collars were made from $\frac{1}{2}$-inch O.D. steel tubing by soldering the appropriate nuts in each end ($\frac{1}{4}$-inch right-hand thread in on end and $\frac{5}{16}$-inch left-hand thread in the other). Thus, when the collar is turned in one direction the cell will be

raised and vice versa.

The shield and liquid nitrogen storage vessel were wrapped with extra-heavy aluminum foil. Likewise, a circular piece of aluminum foil large enough to surround the entire shield, cell, and LN_2 vessel was cut and fastened into place. These aluminum foil coverings serve as radiation shields and together with the radiation shields in the surrounding dewar they help to diminish the amount of heat transferred into the system by radiation.

Cryostat Dewar

Since vacuum is about the best insulation at low temperatures, some means is needed of enclosing the area surrounding the shield and cell assembly so that this space can be evacuated. In this work, a super-insulated stainless steel open dewar, manufactured by Hofman Laboratories, is used to enclose the shield and cell assembly. The dewar, $10\frac{5}{8}$ inches in diameter with an inside depth of 30 inches, is flanged at the top and is fastened to the top-plate of the cryostat with twelve $\frac{5}{16}$-inch bolts. The vacuum seal is between the flange and top-plate and is maintained with a Parker Viton O-ring which has a $11\frac{1}{2}$-inch I.D. and a $\frac{1}{8}$-inch thickness.

Cryostat Top-Plate

The top-plate (T) of the cryostat is a circular steel plate 16 inches in diameter and $\frac{1}{2}$-inch thick. In addition to the 12 bolt holes for attaching the flanged dewar and the three threaded anchor holes for attaching the nylon support rods, all the transfer lines and electrical leads to the cell, shield, and LN_2 storage vessel pass through the top-

plate.

All liquid nitrogen transfer lines through the top-plate are $\frac{1}{4}$-inch O.D. thin-walled stainless steel tubing. The equilibrium cell transfer lines are $\frac{1}{16}$-inch stainless steel tubing. The line through which the cell is evacuated (V) is $1\frac{1}{8}$-inch O.D. copper pipe. All these lines were soldered in place to the top-plate.

The electrical leads were brought through the top-plate with Style F ceramic multi-terminal headers made by Lactronics Corporation. The outer metal ring of each lead-through was soldered in a groove to the top-plate and each electrical lead was brought through one of the individual tubes in the header and soldered. Three lead-throughs were necessary. Two of them have 10 terminals and one has 8 terminals.

The cryostat top-plate is supported from a four-legged angle-iron stand. The stand is 6 feet high and is 2 feet square at the top. By suspending the entire cryostat and equilibrium cell in this manner, the cryostat dewar can be removed easily. Likewise, the cell assembly can be worked on and disassembled easily.

Vacuum System

Two vacuum systems are necessary in this work. One system serves to evacuate the cell cavity and vapor system transfer lines and pressure gauges. The other system is for evacuating the cryostat dewar and providing vacuum insulation for the equilibrium cell assembly.

The first system is a Model No. 1402B "Duo Seal" vacuum pump, a large capacity-high vacuum pump manufactured by the Welch Scientific Company. This pump can produce an ultimate vacuum of 0.1 to 1 millitorr and a free displacement of 5.6 CFM (160 liters/min). The vacuum pump

is linked to the vapor flow system by means of a toggle valve.

The second system is a high vacuum system complete with diffusion pump, fore pump, cold trap, ionization gauge, etc. The system is mounted on a mobile stand so it could be used for other applications by disconnecting the vacuum intake line from this equipment and reconnecting the line and vacuum system to another apparatus. (The disadvantages of this mobile vacuum system are discussed later).

A schematic diagram of the high vacuum system is presented in Figure 3. The fore pump for this vacuum system is a Welch Model No. 1402B pump identical to the one mentioned above. A Type EP-2A 2-inch water-cooled diffusion pump made by Veeco Instruments, Inc. is used. The pump is high speed with a constant pumping speed of 90 liter/sec when the intake pressure is below 0.1 millitorr.

Mounted on top of the diffusion pump are a water-cooled baffle and a liquid nitrogen cold trap also manufactured by Veeco. Their purposes are, respectively, to prevent oil losses from the top of the diffusion pump and to condense any heavy components out of the system being evacuated. A 60 cc pump oil charge of Veeco Type DC-704 silicon oil is used in the diffusion pump.

The valves used in the vacuum system are forged brass high vacuum bellows valves made by Veeco. All the elbows, adapters, unions, and other fittings used in the vacuum system are copper sweat fittings and all the tubing is either copper or brass. All connections were made by soldering, except the flanged connections, which use Viton O-rings to produce a seal.

An ionization gauge is located in the vacuum system, just upstream of the cold trap, to measure the vacuum. A Consolidated Vacuum Cor-

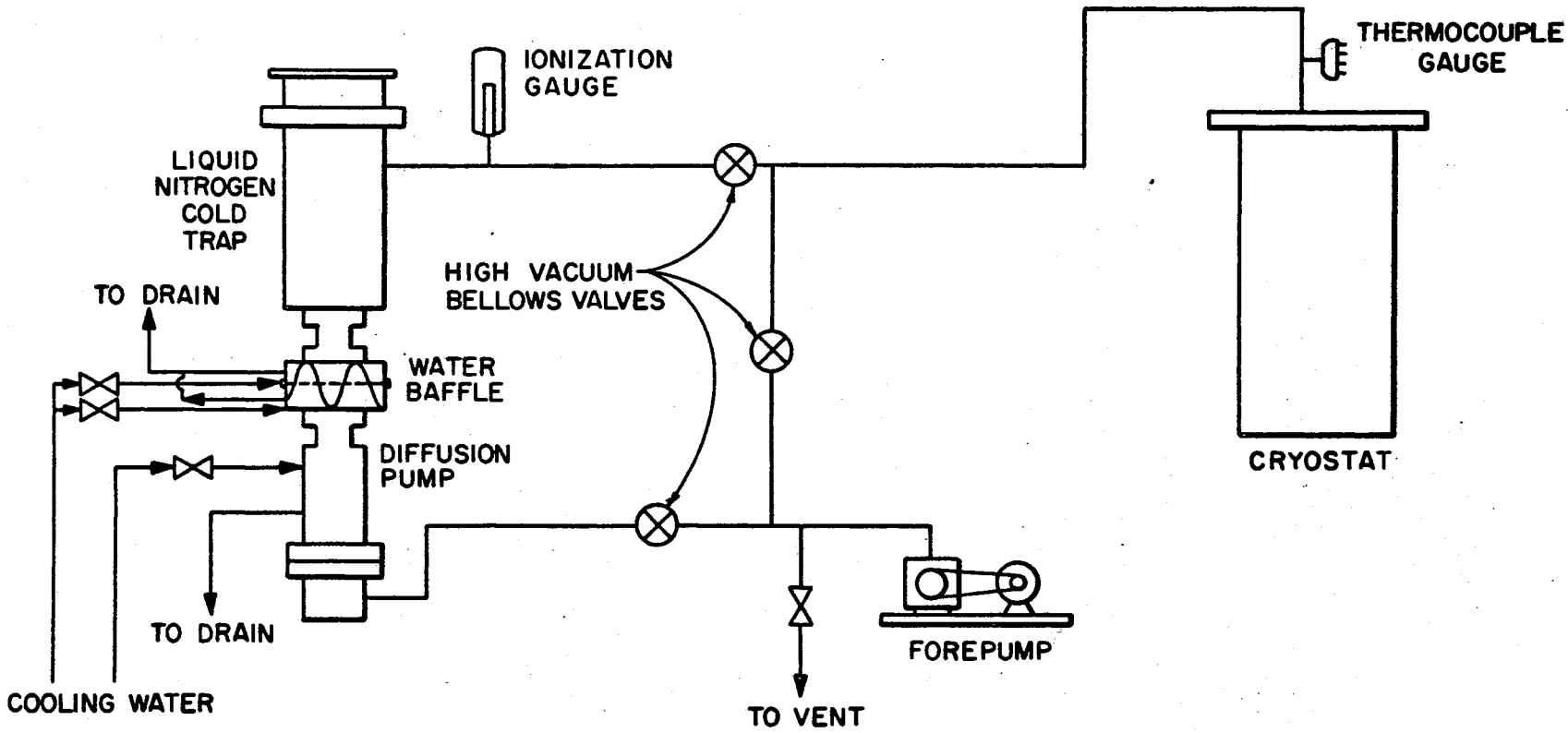

Figure 3. Schematic Diagram of the Vacuum System

poration Type GIC-110 vacuum gauge and a Type VG1A ionization tube are used in this system. The tube was installed using a CVC brass adapter which was soldered vertically onto the system tubing. This adapter uses a compressed O-ring seal to seal the glass base of the vacuum tube into the system.

Because the pressure in the vacuum system should be below 30 to 50 millitorr before turning on the diffusion pump and below one millitorr before turning on the ionization gauge, a thermocouple gauge is mounted on the vacuum transfer line immediately above the cryostat. The thermocouple gauge works very well for a pressure range of 0.001 to 1 torr and provides an easy means of measuring the pressure during the initial evacuation of the system with the forepump. The output of the thermocouple gauge is monitored on one of the thermocouple gauge channels of the GIC-110 vacuum gauge.

After the vacuum system was constructed, it was leak tested independently from the rest of the cryostat assembly. The vacuum system was flanged off with a circular steel plate into which the thermocouple gauge was mounted. When the system was tested in this manner, a pressure of less than 10^{-6} torr could be easily maintained at the vacuum gauge with the diffusion pump in service.

Temperature Measurement and Control

The temperature in the equilibrium cell is measured as near to the vapor outlet port as possible, using a Model No. 8164 platinum resistance thermometer (Serial No. 1697602) made by Leeds and Northrup. The temperature range of the thermometer is -261° to 250° C. and it was calibrated by the National Bureau of Standards over the temperature

range -183° to 250° C. After the thermometer was wired and ready to install in its cell port, the triple point of water was rechecked using a triple point cell manufactured by Trans-Sonics, Inc. The results are presented in Appendix A. The thermometer was sealed in its port (F) in the cell by wood's metal, which melts at about 60° C.

The output of the platinum resistance thermometer is monitored with a Leeds and Northrup Model No. 8069-B Type G-2 Mueller Bridge, capable of measuring resistances in the range from 0 to 111.111 ohms in increments of 0.0001 ohm. A Leeds and Northrup Model No. 9834-2 D.C. null detector is used in conjunction with the G-2 Mueller Bridge for measuring the output of the platinum resistance thermometer. The null detector has a variable sensitivity range and a meter read-out display. The temperature of the cell can be measured precisely to ±0.001° C.

The temperature of the equilibrium cell is controlled by balancing a small amount of liquid nitrogen cooling with a small heat input from the resistance heaters at the top and bottom of the cell. The heaters are regulated by a temperature control system manufactured by Leeds and Northrup. This system is pictured in Figure 4 and consists of a temperature sensing element, a set point unit, a D.C. null detector, a current adjusting controller, and a current controlled A.C. power supply. The sensing element is a three-lead 100-ohm platinum resistance thermometer which is covered with a ceramic material and epoxy resin. The setpoint unit is a Model No. 8064 Resistance Thermometer Bridge capable of measuring resistances in a range of 0 to 160.1 ohms.

The imbalance between the set point unit and resistance thermometer is detected and amplified by a D.C. Null Detector (Model No. 9834-2). This amplified signal is used as the input to the current adjusting

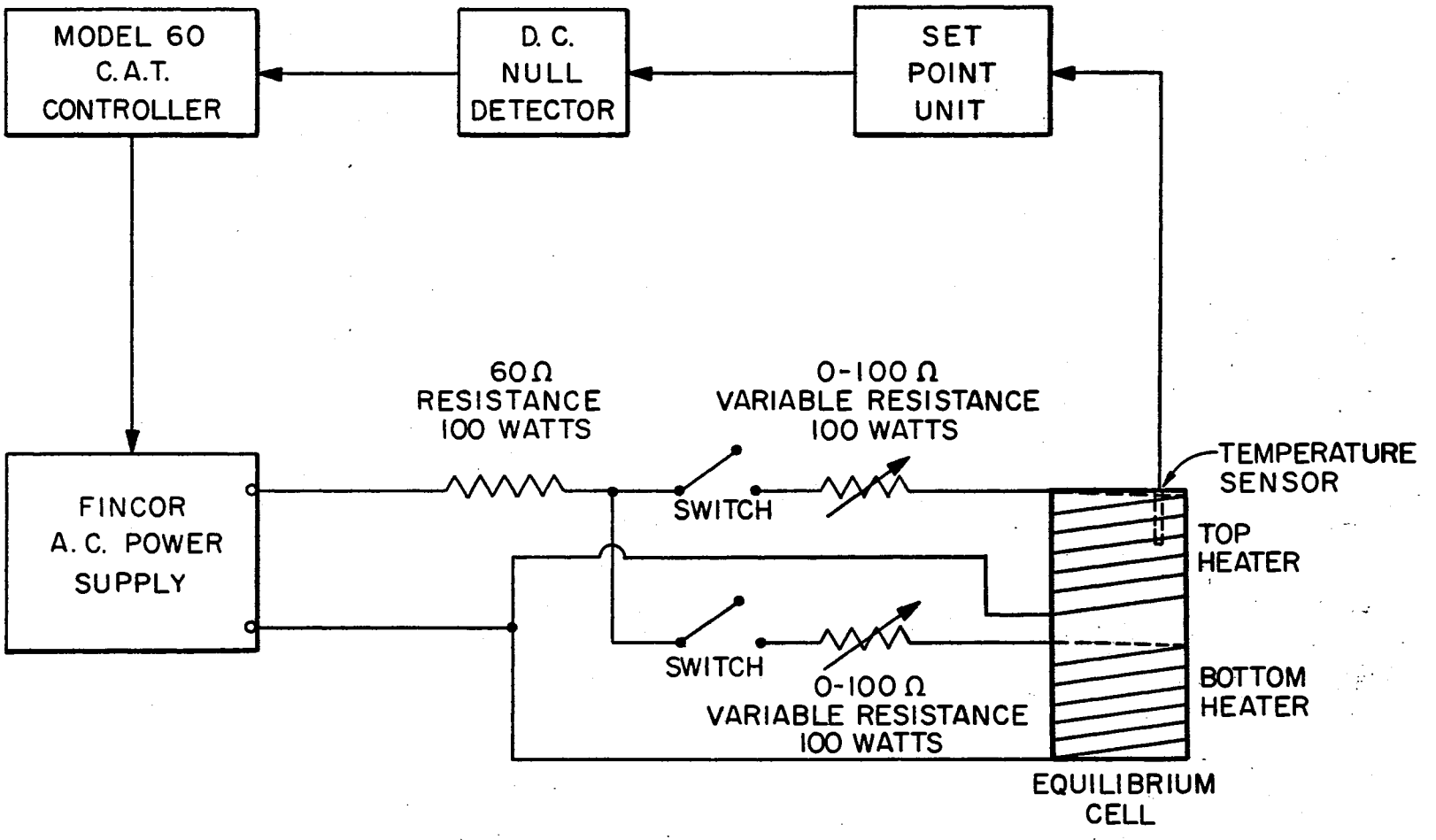

Figure 4. Schematic Diagram of the Cell Temperature Control System

controller (Model No. 60 C.A.T.) which can deliver an output current between 0 and 5.75 milliamps. The controller has three modes of control action, proportional, reset, and rate. The output of the current controller is used to control the output voltage of the A.C. power supply (Fincor Model No. 1200-2.2-11A). The power supply has two potentiometers for adjusting the upper and lower limits of the output voltage. The output voltage can be varied between 0 and 95% of line voltage. The output voltage is dropped across a series of high wattage resistances and is then applied to the cell heaters. With this system the temperature of the cell can be controlled within $\pm 0.01^{\circ}$ to $\pm 0.03^{\circ}$ C. depending upon the operating conditions.

The emf output of the differential thermocouple is measured with a Leeds and Northrup Model 7555-A Type K-5 Potentiometer. This potentiometer unit is capable of detecting emf's with a resolution of ±0.02 microvolt. The sensitivity of a copper-constantan thermocouple at 100° K is approximately 0.019 millivolt/$^{\circ}$C. Thus, temperature gradients of less than $\pm 0.01^{\circ}$C could conceivably be detected.

Liquid Nitrogen Flow Control System

Liquid nitrogen is transferred directly from its storage vessel into the cooling coil of the adiabatic shield where most, if not all, of it is vaporized. A tee (Q) was placed at the exit of the shield cooling coil enabling some of the nitrogen cooltant to be transferred into the cell cooling coil while the remainder is vented.

Tees were placed in the vent lines of both the cell and shield cooling coils. In one branch of both vent lines, a needle control valve and rotameter were installed to carefully monitor and control the

nitrogen cooltant flow to both the cell and the shield. Although the cooling coils were made from $\frac{3}{16}$-inch O.D. copper tubing, all the piping in the LN_2 flow control system outside the cryostat is $\frac{1}{4}$-inch O.D. copper tubing. The rotameter range of the shield cooltant control branch is 0 to 4600 STD cc/min while the rotameter range of the cell branch is 0 to 850 STD cc/min.

The other branch of the shield and cell cooling coil vent lines serves as the control branch bypass. A valve was placed in this branch which would allow full-open flow through the $\frac{1}{4}$-inch copper tubing. This branch of the vent lines is used during the initial cool down of the shield and cell assembly when large amounts of liquid nitrogen are vaporized and cause high vapor flow rates. The control valves will not pass enough vapor to permit reasonable cool-down times and thus, the bypass branches are needed.

Pressure Control and Measurement

The pressure is controlled using a "Mity-Mite" (Model No. 94) pressure regulator, manufactured by Grove Valve and Regulator Co., upstream of the cell. The maximum inlet pressure to the "Mity-Mite" is 5000 psi and the maximum outlet pressure that can be developed is 3000 psi. Downstream of the cell the pressure is let down to atmospheric conditions across a regular high pressure valve. Gas is supplied to the "Mity-Mite" pressure regulator from a high pressure gas bottle regulator at a pressure 50 to 100 psia greater than the desired system pressure. The dome of the "Mity-Mite" is internally loaded with system gas. During an experimental run, the pressure could always be controlled to a value less than the precision of the pressure measuring

equipment.

Three bourdon tube pressure gauges, manufactured by Heise Bourdon Tube Company, Inc., are used to measure the system pressure depending upon the operating pressure. A gauge with a pressure range of 0 to 3000 psig is used to measure all pressures above 1000 psig (68.1 atm). A gauge with a range of 0 to 1000 psig is used for system pressure between 300 and 1000 psig (20.4 and 68.1 atm) and a gauge with a range of 0 to 300 psig is used for system pressures below 300 psig (20.4 atm). The precision of these gauges is ±0.1% full scale or ±3 psig (±0.20 atm) for the high range pressure gauge, ±1 psig (±0.07 atm) for the intermediate range gauge, and ±0.3 psia (±0.02 atm) for the low range gauge. All three gauges were calibrated against a Model 2400 HL dead weight gauge manufactured by Ruska Instrument Co.; the results of these calibrations are shown in Appendix B.

The three pressure gauges are valved into the vapor flow system so that the pressure can be measured on either the upstream or the downstream side of the equilibrium cell. In this manner, any pressure drop across the cell can be detected. In this work, no detectable pressure drops in the vapor flow system, specifically across the equilibrium cell, were ever detected.

Vapor Analysis System

The vapor phase which leaves the equilibrium cell is analyzed with an ultrasonic detector and phase meter unit of a MT-150 gas chromatograph made by Tracor, Inc. The ultrasonic detector system measures changes in the speed of sound in a gas sample, due to changing gas composition, by comparing the phase angle of the received signal with that

of a reference signal. Thus, this change in phase angle due to changing gas composition provides a means of analyzing the composition of a gas mixture. Since the response (phase angle change) of the detector is a relatively linear function of composition when the composition of the component of interest is relatively small (mole fractons less than 0.01), the ultrasonic detector is an excellent technique for analyzing gas mixtures containing trace components.

The detector uses very sensitive pressure transducers in making the speed of sound measurements. The detector is constructed of corrosion resistant materials and any gas may be used as a carrier although the best carrier gases are those that lead to the largest detector response (phase angle change) when other gases are introduced. The output signal of the detector cells is very sensitive to temperature changes and thus, the temperature of these cells must be controlled to less than $\pm 0.001^{\circ}$ C. The detector cells are operated at 125° C.

A schematic diagram of the gas analysis flow scheme is presented in Figure 5 and an individual ultrasonic detector cell is shown in Figure 6. A gas sample is trapped in a sampling loop by a compressed air-activated solenoid valve and is then flushed into the carrier gas stream leading to one of the two detector cells in the system. The output signal of the detector cell is compared to a reference signal by means of a phase meter which in turn imparts a emf signal to a recorder. The recorder used in this work is made by Minneapolis-Honeywell (Model No. 15307856-01-05-0-000-715-07 009) and has a range of -0.2 to 1.0 millivolt.

Since the speed of sound is sensitive to changes in the density of the gas mixture, the temperature and pressure of the vapor samples must

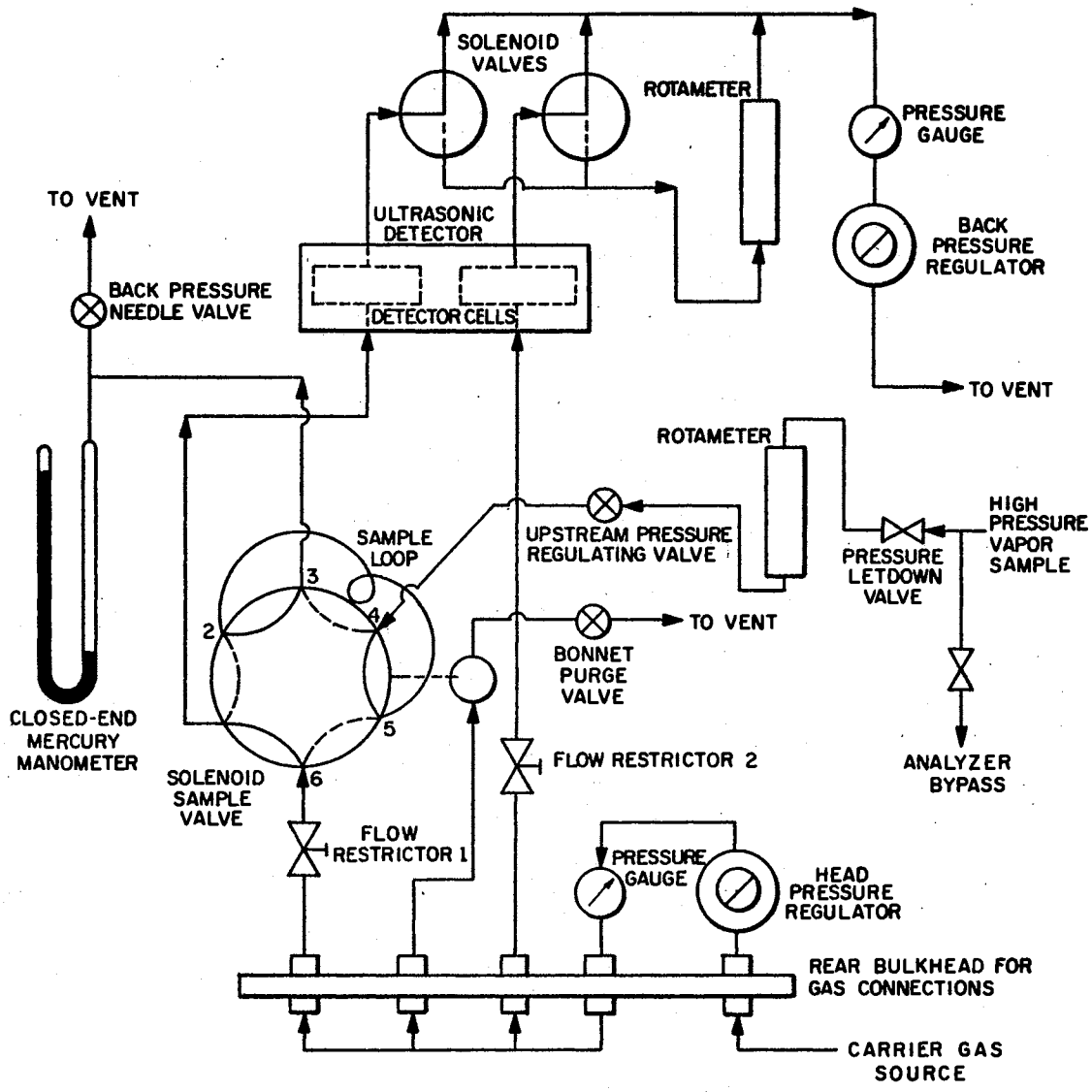

Figure 5. Schematic Diagram of the Gas Analysis System

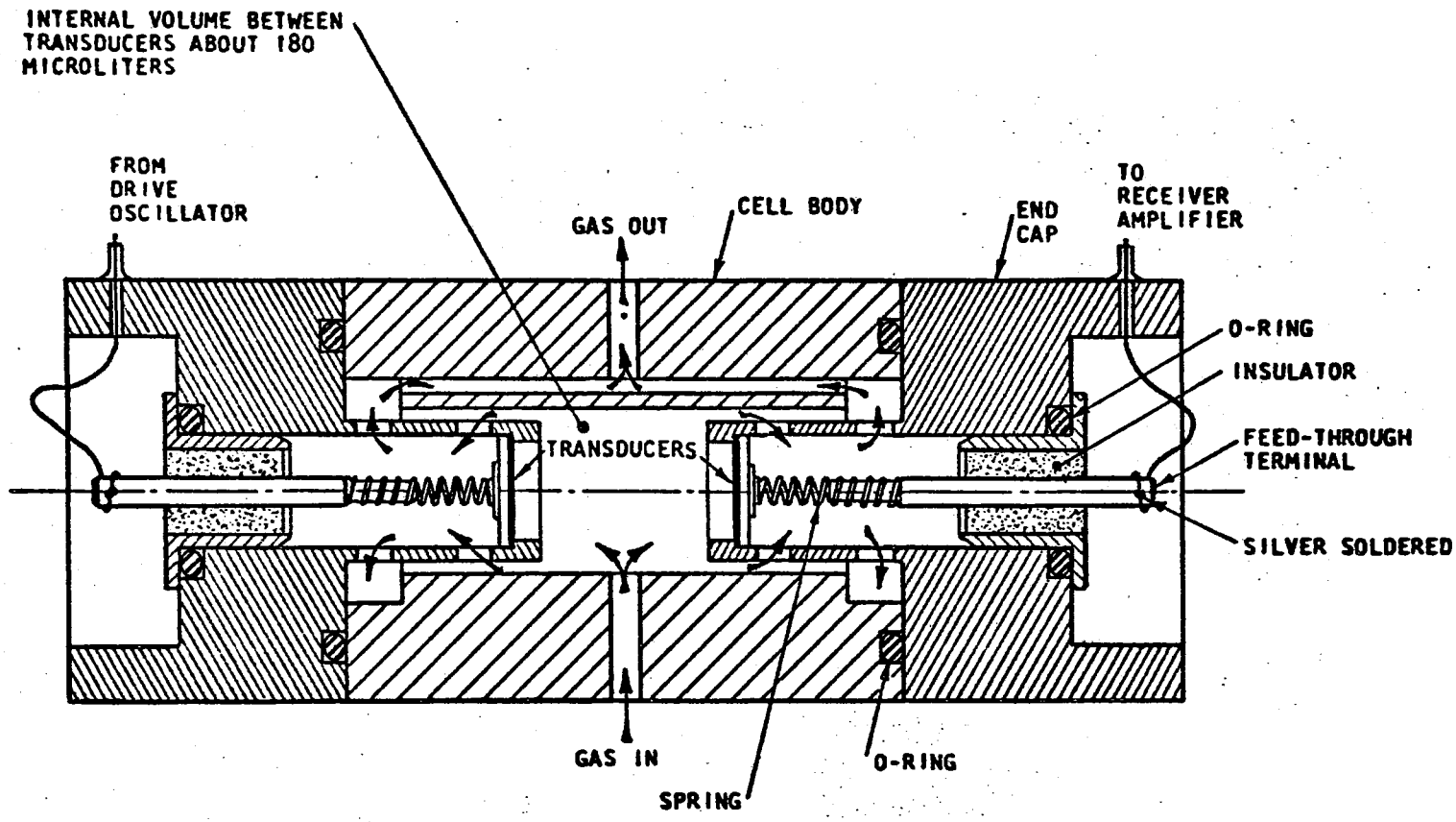

Figure 6. Schematic Diagram of an Ultrasonic Detector Cell (16)

be carefully controlled. Sampling in the manner described insures that the only variable affecting the mass density of the gas sample is composition. The sampling valve is insulated and its temperature is controlled at approximately 25° C to ±0.1° C.

After the vapor stream leaves the equilibrium cell, its pressure is dropped to slightly above atmospheric conditions across a high pressure valve. The vapor stream then passes through a line filter and into a rotameter with a range of 0 to 720 STD cc/min. The vapor is transported to the sampling section of the ultrasonic detector through thin-walled $\frac{1}{16}$-inch O.D. stainless steel tubing. The vapor stream flows continuously through the sample loop of the sampling valve and then to vent. A needle valve is located downstream of the sample loop to serve as a back pressure regulator for the sample loop vapor stream. The pressure in the sample loop is measured by a closed-end mercury manometer and is maintained at a constant value using a needle valve upstream of the sample loop. Another line filter is positioned upstream of this needle valve.

Carrier gas flows through both ultrasonic detector cells simultaneously. The carrier gas passes through a head pressure regulator and pressure gauge and is then split into two streams before entering the detector cells. A flow restrictor is located in each of the two lines upstream of the detector cells. The sampling valve is positioned between the restrictor and detector cell of one of the channels. Downstream of the detector cells, the two streams pass through solenoid switching valves which can be used to direct the flow of one or both of the streams to a rotameter. These solenoid valves as well as the sampling solenoid valve are activated by compressed air. Finally, the two

streams are rejoined and pass through a pressure gauge and back pressure regulator before being sent to vent. The back pressure on the detector cells must be maintained at a constant value in the same manner as the sample pressure in order to insure reproducible results. Carrier gas is also used to purge the bonnet of the sampling valve.

Either of the detector cells can be used individually by referencing its output signal to an electronic reference signal. A differential mode of operation which entails using the output signal of one of the detector cells as the reference signal is used in this work because of the following advantages:

(1) the problem of possible hysteresis of an electronic reference signal is eliminated,

(2) any signal due to impurities in the carrier gas will tend to be cancelled because carrier gas flows through both detector cells.

Helium is used as the carrier gas in this study and, since helium is also the major component in the binary mixtures to be analyzed, the mixture can easily be analyzed for the trace component.

No columns are needed in this work because no separation is necessary. Because the response of the detector results in a smooth, sharp peak on the recorder and since these peaks are quite reproducible, peak height rather than area is used as a measure of the response of the detector to the trace components. Trace components in a helium carrier that are heavier than helium give a positive phase shift and, therefore, a positive peak.

When using helium as a carrier gas, the response of the detector is relatively independent of the detector cell pressure when this pres-

sure is between 10 and 50 psig (16). Likewise, tests in this work showed that the detector response is approximately flow rate independent for flow rates in the range of 20 to 35 STD cc/min at a back pressure of 48 psig. During normal operation, a back pressure of 48 psig was maintained on the detector cell and a flow rate of approximately 25 to 30 STD cc/min was maintained through it.

The ultrasonic detector is the key constituent of this solid-vapor equilibrium apparatus because, with a good calibration, the detector can be used to determine the trace component composition with an imprecision of less than one percent. The calibration of the detector is discussed in the following chapter. A more complete discussion of the theoretical aspects of an ultrasonic detector is presented in Appendix C.

Equipment Deficiencies

The main problem encountered in the operation of the cryostat is the high consumption rate of liquid nitrogen. Although the liquid nitrogen storage vessel holds over 2100 cc, the cryostat can only be operated for approximately 10 to 12 hours without refilling the LN_2 storage tank. While this does not prevent operating the cryostat in a normal manner, refilling the LN_2 storage vessel every 10 to 12 hours is inconvenient.

In a high vacuum (10^{-5} torr or less), conductive and convective heat leaks through the vacuum insulation should be quite small. Radiation heat leaks should be negligible if radiation shields are used in the cryostat. Thus, the major heat leak should arise from the conduction of heat from the top-plate of the cryostat down the transfer lines

and electrical leads to the cell assembly.

Preliminary heat conduction calculations showed that the heat leak from the top of the cell by conduction is about 1.5 BTU/hr which corresponds to a liquid nitrogen loss of approximately 10 cc/hr. Theoretically, therefore, the cryostat could be operated about 200 hours without refilling the liquid nitrogen storage vessel.

Several factors probably contribute to the large discrepancy between the actual and calculated liquid nitrogen usage. One factor could be that the radiation heat loss is not negligible. Another is that the conductive heat leak from the top of the cryostat could be larger than calculated. A third factor is that a small amount of heat is being put into the cell from the temperature control heaters.

However, the most important factor contributing to the high liquid nitrogen usage is that the pressure inside the cryostat is greater than 10^{-5} torr. In reality, it is probably closer to 10^{-4} torr. When the pressure on a gas is above 1 torr, the kinetic theory of gases predicts that the thermal conductivity of the gas is independent of pressure because the mean free path of the gaseous molecules is small compared to the distance between the surfaces of the heat source and the heat sink. However, when the pressure on a gas drops below 10^{-3} torr, the thermal conductivity and thus, the transfer of heat by conducting, becomes nearly proportional to the system pressure (53). Therefore, if the vacuum pressure was 10^{-4} torr instead of 10^{-5} torr, the conductive heat leak through the vacuum insulation could be 10 times larger at the higher pressure and easily account for the major part of the heat leak problem.

The difficulty in maintaining the vacuum pressure in the cryostat

at 10^{-5} torr arises from the fact that the transfer line between the cryostat and the vacuum system is too long and contains several elbows. Thus, the diffusion pump assembly should have been mounted nearer the top of the cryostat to eliminate the long transfer line. In this manner, an adequate vacuum could probably be established inside the cryostat and liquid nitrogen usage could be diminished.

Another problem associated with cryostat operation is an inadequate level monitoring system for the LN_2 storage vessel. As attempt was made to construct a liquid level indicator using a thin platinum wire element similar to one designed and tested by Maimoni (37). However, these efforts proved fruitless when the level indicator failed to show any sensitivity to the liquid level inside the LN_2 storage tank. The insensitivity of the level indicator is probably due to the fact that the platinum wire used as the sensing element is at least an order of magnitude too large in diameter. Therefore, no level indicator was used in this study.

Another equipment deficiency is associated with the differential thermocouple located on the cell. Originally, the thermocouple beads were placed at the top and bottom of the cell in order to detect any cell temperature gradients. Then the bead at the top of the cell was relocated on the vapor outlet line so that the temperature difference between the cell and vapor outlet line could be measured. Unfortunately, when the thermocouple was relocated, no means remained of detecting cell temperature gradients. Even though no detectable temperature gradients on the cell were ever measured during cryostat operation, two differential thermocouples would be better than one. One could be used for measuring cell temperature gradients and the other for monitoring

the vapor outlet line temperature.

A further imperfection is associated with the high vacuum system and arises from the fact that the ionization gauge is located too far from the cryostat for an accurate measurement of the vacuum inside the cryostat. Therefore, the ionization gauge should be located in the vacuum transfer line where it exits the cryostat.

A problem arose from the plugging of the inlet gas transfer line when the heavy component was condensed into the equilibrium cell cavity. Helium was passed through the cell after the heavy component was condensed in the cell as a liquid to prevent plugging upon freezing. However, this did not always prevent plugging and a resistance heater was wrapped around the inlet vapor line and epoxyed in place to help eliminate the problem.

Materials

All the gases used in this work (helium, argon, krypton, and xenon) were high purity gases. The source and minimum purity of each of these gases is as follows:

Gas	Manufacturer	Minimum Purity, mole %
helium	U. S. Bureau of Mines	99.9997
	Airco Rare and Specialty Gases	99.9999
argon	Airco Rare and Specialty Gases	99.995
krypton	Air Products and Chemicals, Inc.	99.995
xenon	Air Products and Chemicals, Inc.	99.995

CHAPTER V

EXPERIMENTAL PROCEDURE

In this chapter, a detailed description of the equipment operating procedure is presented including initial start-up, temperature control, and normal operation. The procedure for calibrating the ultrasonic detector is also presented.

General Description

After the cryostat has been completely assembled, it is evacuated for several days. When the vacuum reaches a suitable level, the liquid nitrogen storage vessel is filled and the equilibrium cell assembly is cooled. The less volatile component (krypton or xenon) is condensed as a liquid on the equilibrium trays and packing inside the cell cavity. The cell is then cooled to its normal operating temperature and the condensed liquid freezes in place. Finally, temperature control is established on the cell.

After the equilibrium cell reaches its operating temperature, it is filled with the more volatile component (helium) to the highest pressure at which an experimental measurement is made. In order to accomplish this, the "Mity-Mite" pressure regulator must be set to deliver the appropriate operating pressure. In this work, measurments are made in steps of descending pressure for convenience in adjusting the "Mity-Mite".

After the cell has been pressured, a high pressure valve downstream of the cell is cracked open and a flow of vapor from the cell to the ultrasonic detector sampling valve is established. At the same time, temperature control is re-established on the cell, and time is allowed for the vapor and solid inside the cell to come to equilibrium.

After an appropriate length of time, sampling to the detector is begun. When the response of the detector is constant for a reasonable period of time, a composition measurement has been accomplished. The vapor flow rate out of the cell is increased significantly by opening another valve in the vapor effluent stream which bypasses the detector. Thus, the flow rate from the cell can be increased without changing the flow rate to the detector sampling system. Again, sampling to the detector continues until the response is constant. This procedure provides a test for equilibrium because equilibrium inside the cell is implied if the composition of the vapor phase is independent of flow rate.

After a composition measurement is completed, the pressure in the cell is adjusted (usually decreased) to a new value and another composition measurement is made. This procedure continues until the desired pressure range has been covered. Then, the cell is repressured with the lighter component (helium) of the same cell temperature and another series of pressure-composition measurements is made over the same pressure range. This procedure serves to establish the reproducibility of the measurements.

The temperature of the cell is changed to a new value and the above procedure is repeated until several isotherms of pressure-composition measurements have been completed. For convenience, the measurements are generally made in steps of decreasing temperature. Depending

upon the amount of solid originally condensed, and the amount of time required for each experimental run, five to ten isotherms of data can be taken before the cell needs to be refilled. Given below are detailed descriptions of the individual procedures which must be performed before an experimental run can be made. A detailed description of an experimental run is also presented.

Evacuation of the Cryostat

After the equilibrium cell and cryostat have been completely assembled, the forepump of the high vacuum system (Figure 3) is started. The valve in the transfer line between the cryostat and the diffusion pump, and the valve between the diffusion pump and forepump are opened. As the cryostat is evacuated, the pressure inside the cryostat is monitored with the thermocouple gauge mounted in the transfer line leaving the cryostat. The pressure range on the thermocouple gauge is 1 to 1000 millitorr.

When the pressure reaches 10 millitorr, the cold trap is filled with liquid nitrogen and the diffusion pump is turned on. Cooling water to the water baffle and diffusion pump is turned on and the rates adjusted. The water flow rate to the baffle is set as high as possible, but the water rate to the diffusion pump should be adjusted so that the effluent water stream is between 50° and 60° C. In practice, however, a higher water rate than this is often used with no apparent loss of efficiency in the diffusion pump.

The vacuum system is allowed to pump on the cryostat for several days while the equilibrium cell assembly and the inside of the cryostat "outgas". The ultimate vacuum obtainable when the cryostat is cooled

to normal operating temperatures is slightly less than 10^{-5} torr. However, this is the pressure measured at the ionization gauge. Because the ionization gauge is located some distance from the cryostat, a more realistic value of the pressure in the cryostat would be on the order of 10^{-4} torr.

The ionization gauge should never be turned on when the pressure in the system is above 1 millitorr. The hot diffusion pump oil should never come in contact with pressures higher than 50 millitorr. Therefore, when the vacuum system is turned off, the diffusion pump is valved out of the system and the bypass valve to the forepump is opened. The diffusion pump can then be turned off with no danger to the pump oil. The forepump can then be turned off and the vacuum on the cryostat released by means of the vent valve in the forepump transfer line.

Cooling of the Equilibrium Cell

When a reasonable vacuum has been established inside the cryostat, the liquid nitrogen storage vessel is filled through a $\frac{1}{4}$-inch transfer line from an LS-110 dewar of liquid nitrogen (LN_2). When a normal vacuum exists inside the cryostat (10^{-4} torr), the liquid nitrogen inside the storage tank exerts a vapor pressure of 5 to 10 psig. A needle valve is used in the vent line of the storage vessel as a back pressure regulator to prevent a pressure "build-up". The pressure on the storage vessel is monitored with a pressure gauge, located in the vent line, with a range of 0 to 100 psig.

After the LN_2 storage vessel has been filled, the bypass valves in the exit transfer lines from the cell and shield cooling coils are opened completely. This allows the liquid nitrogen to flow into the

cooling coils where it evaporates and cools the cell assembling. In this manner, the cell and shield assembling are cooled to a temperature near the cryostat's normal operating conditions. The LN_2 storage vessel has to be refilled at least once during the cool-down procedure.

After the cell and shield assembly has been cooled, the bypass valves are closed and the needle valves in the flow control loops of the cooling coil exit lines are adjusted for the proper nitrogen rates. A slight excess of nitrogen is used in normal operation so that it can be balanced by a small amount of heat input from the temperature control unit. During normal operation, the flow rate of nitrogen vapor leaving the shield cooling coil is about 1000 STD cc/min and that leaving the cell cooling coil is between 600 to 850 STD cc/min depending on the cell temperature. This corresponds to a liquid nitrogen usage of approximately 160 cc/hr.

Most if not all of the liquid nitrogen evaporates in the shield cooling coil and cold nitrogen vapor flows in the cell cooling coil. During normal cell operation, the nitrogen flow rates through the cooling coils are extremely "bumpy". This would seem to indicate that a slug of liquid somewhere in the cooling coils has flashed and caused a sudden surge of vapor to exit the coils. In practice, much better temperature control can be maintained when the nitrogen flow through the shield and cell cooling coils is "bumpy". This is probably true because the lag time in cooling cycle of temperature control is greatly decreased for the case of "bumpy" nitrogen rates.

The cryostat could generally be operated for 10 to 12 hours without refilling the liquid nitrogen storage vessel. The storage container is refilled every 10 hours to assure the continuous operation of the

cryostat. It is filled until liquid nitrogen comes out the top of the vent line which assures that the container is full.

Condensation of Solid in the Equilibrium Cell

The cell assembly is cooled to a temperature between the normal boiling point and triple point of the component to be condensed. Before the initial cool-down procedure, the cell is evacuated and flushed with helium, so that no impurities will be condensed in the cell cavity. Since the condensed component is a gas at room temperature, a one-liter transfer cylinder is evacuated and filled with enough vapor to produce a known amount of solid when condensed in the cell cavity.

Generally, about 9 to 12 cc of liquid are condensed into the cell cavity which corresponds to about 9 to 12 cc of solid after freezing. Approximately 90 to 100 psia of gas pressure in the one-liter cylinder is needed to yield this much solid. With all the other transfer lines to the cell valved off, valve 1 in the condensate fill line is "cracked" open and the gas slowly bleeds into the equilibrium cell where it is condensed. This condensation within the cell cavity causes an upset in the automatic temperature control (see below). Therefore, the nitrogen cooling rate to the cell must be greatly increased until all of the gaseous heavy component in the transfer cylinder is condensed into the cell cavity and automatic temperature control on the cell is restored.

After the heavy component is condensed into the equilibrium tray section, valve 1 in the condensate fill line is closed and valves 3 and 4 in the inlet and outlet vapor transfer lines are opened. The cell is pressured with helium and a flow rate through the cell is established. Then the cell assembly is cooled to that temperature below

the triple point of the heavy component at which an experimental run will be made. As the cell is cooled, the liquid on the trays and in the packing is frozen in place. The helium flow through the cell helps prevent the plugging of any transfer lines in which some liquid might have condensed. During the course of this work, a resistance heating wire was wrapped around the vapor inlet line to help eliminate the plugging problem.

Temperature Control

When the equilibrium cell has been cooled to the desired operating temperature as measured by the platinum resistance thermometer and the liquid nitrogen rates have been properly adjusted, temperature control must be established. Since the nitrogen cooling rates are a constant, the variable to be controlled is the heat input to the cell.

Two separate heaters are located on the cell, one at the top of the cell and one at the bottom. Variable high wattage resistors (0 to 100 ohms) are located in each heater circuit and are used in conjunction with another constant resistance load to each heater. Either heater can be used independently of the other. The Fincor A. C. power supply has two adjustable potentiometers for controlling the upper and lower limits of output voltage to the cell heaters. The potentiometers are adjusted so that the output voltage range of the power supply is approximately 25 to 100 volts.

The A. C. power supply is controlled by a current input which is the output of the current adjusting controller. The output current range of the controller is 0 to 5.75 milliamps. The controller has three modes of operation; proportional, reset, and rate. The current

output of the controller can be operated manually until the optimum arrangement of heater usage and variable resistance settings is established. During normal operation, only the top cell heater is used and depending upon the operating temperature, variable resistor settings of 40 to 70 ohms are used.

When the proper heater circuit resistance setting has been established, the proportional mode of the controller is adjusted. The set point unit is adjusted so that the temperature oscillates around the correct value as measured by the platinum resistance thermometer. The high sensitivity range of the set point unit is used to monitor the output of the temperature probe. The highest sensitivity is also used on the D. C. null detector.

The proportional mode of the controller is adjusted until the magnitude and period of the temperature oscillations have been reduced to the optimum level as indicated by the temperature control unit manual. Then the reset and rate are adjusted to "fine-tune" the temperature control. During normal operation the proportional mode setting is between 8 and 20%, the reset mode setting is between 0 and 100 and the rate mode setting is zero, i.e., it is not used. By using this temperature control unit, the temperature of the equilibrium cell can be controlled to $\pm$ 0.01° to $\pm$ 0.030° C. depending upon the operating temperature, the nature of the cryostant vacuum, and the nature of the nitrogen cooling flow.

Experimental Run

When the above procedures have been completed, experimental measurements can be made. First, the equilibrium cell is filled with

helium to the desired operating pressure. Refering to Figure 2, all the numbered valves are closed except valves 5, 10, and 15. Helium is supplied to the inlet of the "Mity-Mite" regulator at a pressure 25 to 50 psi greater than the desired operating pressure from the helium storage cylinder.

Then, by using the 3000 psig pressure gauge as a guide, the dome of the "Mity-Mite" is loaded so that it will deliver the desired pressure. Valve 15 is closed, and the pressure is released from all of the system including the "Mity-Mite" by opening valve 6 and then venting the gas through valve 13. Gas is vented to a pressure corresponding to the pressure in the equilibrium cell. Valve 13 is closed and valves 3, 4, and 7 are opened. Valve 15 is cracked open and the equilibrium cell is slowly pressured through both its inlet and outlet transfer lines.

For convenience, the cell is usually filled to the highest experimental pressure first. Measurements are then made at decreasing increments because the dome of the "Mity-Mite" can be more easily vented than loaded. Although the measurements are usually made in decreasing pressure steps, several runs were performed in increasing pressure steps with no detectable difference in the measurements.

Pressuring the equilibrium cell results in an upset in the automatic temperature control. When this temperature upset has been corrected and good control re-established, valve 15 is opened completely and valve 5 is closed. Vapor flow from the cell to the detector sampling system is initiated by cracking valve 12 open. Valve 12 is adjusted until the desired pressure in the sample loop as measured by a mercury manometer is reached.

Vapor is allowed to flow from the cell for a period of 15 to 30

minutes before samples are sent to the detector. The vapor is sampled until the response of the detector remains constant for a reasonable period of time. In this manner, a composition measurement is made. In order to assure that equilibrium has been attained inside the cell, the flow rate from the cell is increased by a significant amount (doubled, tripled, etc.) by cracking open valve 13. The increased flow bypasses the detector sampling system. Again the vapor effluent is sampled until a constant detector response is obtained. Increasing the vapor flow rate from the cell never influenced the concentration measurements, a good indication that equilibrium exists in the cell.

After a composition measurement has been made at one pressure, the pressure in the cell is lowered to a new value. Valves 3, 7, 12, and 13 are closed. Valve 5 is opened. Valve 13 is cracked open and pressure is bled off the dome of the "Mity-Mite" until its output pressure reaches the desired value as indicated by the pressure gauge. The regulator on the helium storage cylinder is re-adjusted so that the 25 to 50 psi differential across the "Mity-Mite" is re-established. Valves 5 and 13 are closed and valve 7 is cracked open and the pressure bled from the cell into the pressure gauge until pressure equilibrium is reached throughout the system. Finally, valve 13 is cracked open and pressure is slowly bled from the entire vapor system until the new operating pressure has been reached at which point valve 3 is re-opened, valve 12 is cracked open and adjusted, and valve 13 is closed.

At the new operating pressure, the entire composition measurement procedure is repeated. The above procedure is repeated until the measurements at the lowest operating pressure have been made. The cell is then repressured and the whole run is repeated to assure reproduci-

bility of the measurements.

In practice, during the first run for an isotherm, composition measurements are made at pressures of approximately 120, 100, 80, 60, 40, 20, and 10 atmospheres. During the second run, measurements are made at approximately 110, 90, 70, 50, 30, and 10 atmospheres. Good reproducibility of measurements is obtained throughout the work. For each experimental datum point, the following variables are recorded:

(1) G-2 Muellar Bridge readings (temperature measurement)

(2) barometer reading (usually made only at the start and end of each run)

(3) pressure measurement

(4) detector response.

Also, the sample pressure and detector carrier gas back pressure are monitored throughout a run to assure their constancy. When two runs are completed at the same temperature, the equilibrium cell is changed to a new temperature, temperature control is re-established, and the above experimental procedure is repeated.

Calibration of the Ultrasonic Detector

The ultrasonic detector was calibrated over the entire range of composition to be measured for each of the binary systems studied in this work. The detector was calibrated with mixtures of known composition that were prepared in this laboratory using a volumetric technique. A discussion of the equipment used to prepare the known mixtures and the results of the calibration for each system are presented in Appendix D. The results show that the detector response versus composition is relatively linear below trace component mole fractions of

0.002. However, above this value of the trace component mole fraction, curvature begins to appear in the response versus composition curves, and an S-shaped curve results if the range of composition is extended to trace component mole fractions as high as 0.04 to 0.07.

CHAPTER VI

PRESENTATION AND ANALYSIS OF THE EXPERIMENTAL DATA

The first part of this chapter consists of the presentation of experimental data, including preliminary measurements that were made to test the reliability of the equipment and solid-vapor equilibrium measurements on the helium-krypton and helium-xenon systems. The second part of the chapter consists of the analysis of the experimental data, including a discussion of the numerical techniques used and the results of the analysis.

Preliminary Measurements

Two separate experimental tests were used to verify the serviceability of the experimental equipment after it was constructed. In order to assure that the platinum resistance thermometer was functioning properly after it was installed in its cell port, vapor pressure measurements were made on pure argon. The details and results of these measurements are presented in Appendix E. The argon vapor pressure measurements made in the present study are in good agreement (nominal scatter of ± 0.25 psia) with the experimental data of Clark, et al (8) which indicates a nominal temperature agreement in the two sources of data to within ± 0.03° K. These measurements coupled with the measurement of the triple point of water served to establish the reliability of the platinum resistance thermometer.

The second test was designed to examine the overall reliability of the equipment; i.e., to assure that equilibrium was being established in the vapor effluent stream, that no temperature gradients or cold spots existed in the cell, etc. To accomplish this goal, liquid-vapor equilibrium measurements were made on the helium-argon system. Data were taken at several different pressures at each of two temperatures, 91.98° K and 108.02° K. Only the vapor phase was analyzed and the measurements were compared with those of Mullins and Ziegler (43) and Hiza (20). The measurements and the results of the comparison are presented in Appendix F. The data taken in the present study are in good agreement with the data of the other investigators (nominal scatter in the argon enhancement factors of ±1%), providing additional evidence that the equipment and procedure are reliable.

Presentation of the Experimental Data

After the preliminary measurements were completed, experimental solid-vapor equilibrium measurements were made on the helium-krypton and helium-xenon binaries. For the helium-krypton system, data were taken at six different isotherms, namely, 90, 95, 100, 105, 110, and 115° K. For the helium-xenon system data were taken at four different isotherms, namely, 120, 130, 140, and 155° K. Examples of typical experimental runs are presented in Appendix G.

The experimental equilibrium data are presented in Table II and III and in Figures 7 and 8. In Tables II and III, the experimental krypton and xenon compositions are tabulated as functions of temperature and pressure. The enhancement factors, $\phi_i = Py_i/P_i^o$, are also tabulated. Since the enhancement factor is a function of the vapor pressure of the

TABLE II

EXPERIMENTAL SOLID-VAPOR EQUILIBRIUM DATA FOR THE HELIUM-KRYPTON SYSTEM

Temperature °K	Pressure atm	Mole Fraction Krypton	Krypton Vapor Pressure* atm	Krypton Enhancement Factor*	Krypton Vapor Pressure** atm	Krypton Enhancement Factor**
90.00	119.15	0.000354	0.02653	1.590	0.02668	1.581
	117.99	0.000357		1.588		1.579
	109.35	0.000373		1.537		1.529
	98.53	0.000397		1.474		1.466
	98.53	0.000399		1.482		1.473
	90.43	0.000423		1.442		1.434
	89.82	0.000421		1.425		1.417
	77.03	0.000480		1.394		1.386
	77.03	0.000480		1.394		1.386
	70.16	0.000510		1.349		1.341
	56.49	0.000607		1.293		1.285
	50.33	0.000663		1.258		1.251
	39.63	0.000803		1.200		1.193
	39.58	0.000805		1.201		1.194
	34.12	0.000920		1.183		1.178
	30.16	0.001013		1.152		1.145
	20.52	0.001430		1.106		1.100
	20.27	0.001440		1.100		1.094
	10.08	0.002790		1.060		1.054
	9.76	0.002875		1.058		1.052
95.00	112.75	0.000769	0.05811	1.492	0.05844	1.484
	111.39	0.000769		1.474		1.466
	99.55	0.000843		1.444		1.436
	90.30	0.000898		1.395		1.388
	80.16	0.000985		1.359		1.351
	70.02	0.001078		1.299		1.292
	60.05	0.001225		1.266		1.259
	50.03	0.001412		1.216		1.209
	40.02	0.001712		1.179		1.172
	30.08	0.00224		1.160		1.153
	20.09	0.00318		1.099		1.093
	10.27	0.00598		1.057		1.051
	9.93	0.00621		1.061		1.055
100.00	117.79	0.001450	0.1175	1.454	0.1181	1.446
	115.07	0.001453		1.423		1.415
	109.21	0.001510		1.404		1.396
	100.30	0.001603		1.368		1.361
	99.62	0.001640		1.390		1.383
	89.89	0.00175		1.339		1.332
	80.23	0.00193		1.318		1.311
	80.09	0.00189		1.288		1.281
	70.50	0.00215		1.290		1.283
	60.29	0.00244		1.252		1.245

TABLE II (CONTINUED)

Temperature °K	Pressure atm	Mole Fraction Krypton	Krypton Vapor Pressure* atm	Krypton Enhancement Factor*	Krypton Vapor Pressure** atm	Krypton Enhancement Factor**
100.00	58.97	0.00248	0.1175	1.245	0.1181	1.238
	58.94	0.00248		1.244		1.237
	49.82	0.00287		1.217		1.210
	39.89	0.00343		1.164		1.158
	39.70	0.00343		1.159		1.153
	30.01	0.004415		1.128		1.122
	20.49	0.00619		1.079		1.074
	20.23	0.00632		1.088		1.082
	9.91	0.01235		1.042		1.036
	9.66	0.01270		1.044		1.039
	9.31	0.01310		1.039		1.033
105.00	116.56	0.00265	0.2217	1.393	0.2230	1.385
	110.10	0.00279		1.386		1.378
	99.96	0.00302		1.362		1.354
	90.16	0.00322		1.310		1.302
	80.36	0.00355		1.287		1.279
	70.02	0.00398		1.257		1.250
	60.17	0.00449		1.219		1.213
	50.32	0.00524		1.189		1.182
	40.11	0.00640		1.158		1.151
	30.01	0.00818		1.107		1.101
	20.17	0.01190		1.083		1.076
	10.00	0.02345		1.058		1.052
	9.86	0.02380		1.059		1.052
110.00	119.42	0.00453	0.3947	1.371	0.3970	1.363
	111.12	0.00483		1.360		1.352
	100.30	0.00533		1.354		1.347
	90.16	0.00566		1.293		1.285
	79.68	0.00632		1.276		1.269
	70.09	0.00690		1.225		1.218
	60.53	0.00783		1.201		1.194
	49.41	0.00932		1.167		1.160
	40.04	0.01135		1.151		1.145
	30.18	0.01455		1.113		1.105
	19.56	0.0219		1.085		1.079
	10.17	0.0410		1.056		1.050
	9.86	0.0422		1.054		1.048
115.00	119.22	0.00727	0.6682	1.297	0.6721	1.290
	110.17	0.00785		1.294		1.287
	100.03	0.00839		1.256		1.249
	90.64	0.00915		1.241		1.234
	90.57	0.00916		1.242		1.234
	80.50	0.01010		1.217		1.210

TABLE II (CONTINUED)

Temperature °K	Pressure atm	Mole Fraction Krypton	Krypton Vapor Pressure* atm	Krypton Enhancement Factor*	Krypton Vapor Pressure** atm	Krypton Enhancement Factor**
115.00	69.95	0.01150	0.6682	1.201	0.6721	1.197
	60.09	0.01310		1.178		1.171
	48.27	0.01590		1.149		1.142
	39.74	0.01910		1.136		1.129
	30.12	0.0246		1.109		1.103
	19.90	0.0364		1.084		1.078
	10.10	0.0695		1.051		1.044
	9.62	0.0732		1.054		1.048

*Vapor pressures of Ziegler, et al (61)

**Vapor pressures from the best fit of the experimental data to Equation (12)

TABLE III

EXPERIMENTAL SOLID-VAPOR EQUILIBRIUM DATA FOR THE HELIUM-XENON SYSTEM

Temperature °K	Pressure atm	Mole Fraction Xenon	Xenon Vapor Pressure* atm	Xenon Enhancement Factor*	Xenon Vapor Pressure** atm	Xenon Enhancement Factor**
120.00	118.49	0.000174	0.01485	1.388	0.01495	1.379
	118.49	0.000174		1.388		1.379
	114.63	0.000173		1.332		1.323
	105.17	0.000187		1.321		1.312
	95.08	0.000204		1.303		1.295
	95.08	0.000204		1.303		1.295
	90.20	0.000210		1.273		1.264
	80.06	0.000233		1.254		1.245
	70.03	0.000257		1.212		1.204
	65.06	0.000277		1.211		1.204
	65.04	0.000277		1.211		1.203
	60.11	0.000293		1.188		1.180
	49.67	0.000347		1.161		1.153
	49.57	0.000347		1.160		1.152
	45.07	0.000380		1.153		1.146
	39.99	0.000422		1.136		1.129
	29.87	0.000546		1.098		1.091
	24.96	0.000649		1.091		1.084
	24.96	0.000650		1.092		1.085
	19.91	0.000796		1.067		1.060
	9.98	0.001535		1.032		1.025
	9.95	0.001540		1.032		1.025
	9.85	0.001553		1.030		1.023
130.00	119.86	0.000516	0.04951	1.249	0.04964	1.246
	109.57	0.00554		1.226		1.223
	104.08	0.000575		1.209		1.206
	100.19	0.000606		1.226		1.223
	90.32	0.000649		1.184		1.181
	90.32	0.000648		1.182		1.179
	84.99	0.000688		1.181		1.178
	80.19	0.000723		1.171		1.168
	70.35	0.000805		1.144		1.141
	65.26	0.000864		1.139		1.136
	60.24	0.000937		1.140		1.137
	50.20	0.001093		1.108		1.105
	45.18	0.001197		1.092		1.090
	39.94	0.001360		1.097		1.094
	30.19	0.001757		1.071		1.069
	30.14	0.001760		1.071		1.069
	24.98	0.002095		1.057		1.054
	20.21	0.00258		1.053		1.051
	11.18	0.00457		1.032		1.029
	10.01	0.00510		1.031		1.029

TABLE III (CONTINUED)

Temperature °K	Pressure atm	Mole Fraction Xenon	Xenon Vapor Pressure* atm	Xenon Enhancement Factor*	Xenon Vapor Pressure** atm	Xenon Enhancement Factor**
130.00	9.93	0.00517	0.04951	1.037	0.04964	1.034
140.00	118.38	0.001345	0.1383	1.151	0.1382	1.152
	118.38	0.001345		1.151		1.152
	110.93	0.001412		1.133		1.133
	108.97	0.001435		1.131		1.131
	108.90	0.001432		1.128		1.128
	100.10	0.001555		1.126		1.126
	90.39	0.001695		1.108		1.108
	90.32	0.001697		1.108		1.108
	80.24	0.001905		1.105		1.106
	76.58	0.001970		1.091		1.091
	70.01	0.002152		1.089		1.090
	70.01	0.002158		1.092		1.093
	64.87	0.002335		1.095		1.096
	60.11	0.00251		1.091		1.092
	49.83	0.00300		1.081		1.082
	49.69	0.00299		1.074		1.075
	39.34	0.00372		1.058		1.059
	30.06	0.004825		1.049		1.049
	29.95	0.00487		1.055		1.055
	19.91	0.00720		1.037		1.037
	10.15	0.01400		1.028		1.028
	9.91	0.01417		1.015		1.016
155.00	121.01	0.00461	0.5015	1.112	0.4990	1.118
	120.94	0.004625		1.115		1.121
	120.62	0.004625		1.124		1.130
	120.41	0.00463		1.112		1.117
	114.41	0.00487		1.111		1.117
	110.05	0.00500		1.097		1.103
	109.65	0.00504		1.102		1.108
	100.18	0.00550		1.099		1.104
	100.18	0.00549		1.097		1.102
	100.07	0.00553		1.104		1.109
	95.42	0.00569		1.083		1.088
	90.19	0.00600		1.079		1.085
	90.18	0.00600		1.079		1.084
	90.05	0.00600		1.077		1.083
	90.04	0.00601		1.079		1.085
	80.13	0.00676		1.080		1.086
	80.11	0.00675		1.078		1.084
	80.11	0.00675		1.078		1.084
	75.45	0.00717		1.079		1.084
	70.15	0.00759		1.062		1.067
	65.99	0.00806		1.061		1.066
	60.14	0.008875		1.064		1.070

TABLE III (CONTINUED)

Temperature °K	Pressure atm	Mole Fraction Xenon	Xenon Vapor Pressure* atm	Xenon Enhancement Factor*	Xenon Vapor Pressure** atm	Xenon Enhancement Factor**
155.00	660.06	0.008875	0.5015	1.063	0.4990	1.068
	55.40	0.00962		1.063		1.068
	50.18	0.01050		1.051		1.056
	45.14	0.01165		1.049		1.054
	39.68	0.01320		1.044		1.050
	34.89	0.01513		1.053		1.058
	34.89	0.01510		1.051		1.056
	34.78	0.01510		1.047		1.053
	30.19	0.01722		1.037		1.042
	24.93	0.0209		1.039		1.044
	24.81	0.0210		1.039		1.044
	20.60	0.02515		1.033		1.038
	20.31	0.0254		1.029		1.034
	14.46	0.03525		1.016		1.022
	14.21	0.0357		1.012		1.017
	12.18	0.0414		1.006		1.011
	11.49	0.0440		1.088		1.013
	11.28	0.0449		1.010		1.015

*Vapor pressures of Ziegler, et al (62)

**Vapor pressures from the best fit of the experimental data to Equation (12)

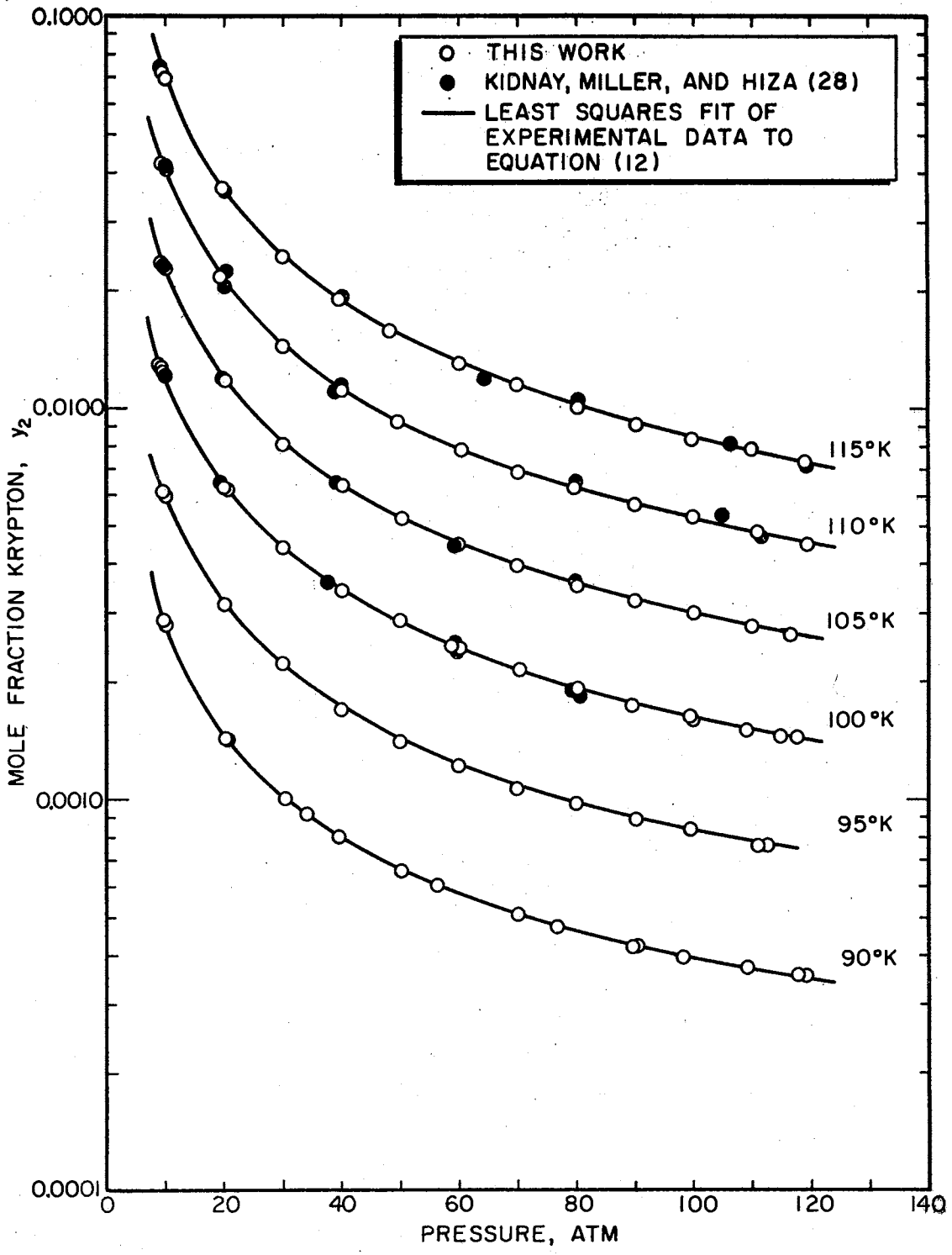

Figure 7. Solid-Vapor Equilibrium Data for the Helium-Krypton System

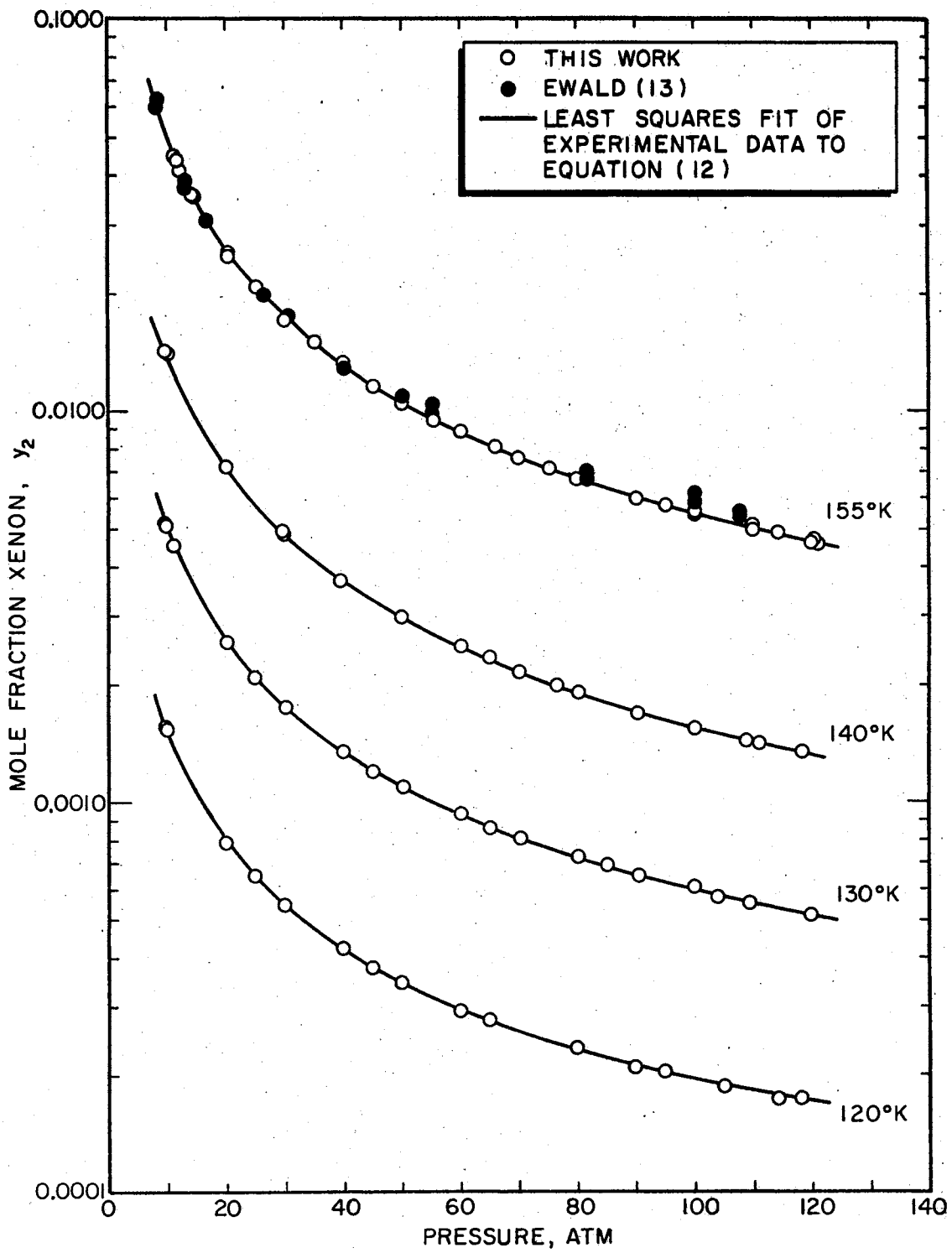

Figure 8. Solid-Vapor Equilibrium Data for the Helium-Xenon System

solid component (component "2"), accurate vapor pressures are required for accurate enhancement factors.

The effect of vapor pressure on the enhancement factor, and thus the interaction virial coefficients, is discussed in detail later. Here, two values of the solid component vapor pressure are used in Tables II and III to obtain enhancement factors. In one case, vapor pressures for both krypton and xenon were taken from the work of Ziegler, et al (61, 62). In Ziegler's work, the vapor pressures were calculated from heats of vaporization and other properties using a thermodynamically rigorous technique. In the other case, the experimental solid-vapor equilibrium data were used to determine the "best value" of the vapor pressure, i.e., the value of the vapor pressure that gave the best fit of the experimental data to Equation (12).

The experimental data for the helium-krypton system are presented in Table II and the helium-xenon data are presented in Table III. The results in these tables show that all the vapor pressures obtained from the best fit of the experimental data to Equation (12) agree with the values of Ziegler, et al, to within less than one per cent.

The experimental measurements are also presented in Figures 7 and 8 where the composition of the trace component (krypton or xenon) in the vapor phase is plotted as a function of pressure for lines of constant temperature. The results for the helium-krypton binary are shown in Figure 7 and are compared with similar measurements made co-currently with this work by Hiza, et al (28). Likewise, the results for the helium-xenon system are presented in Figure 8 and are compared to the older measurements of Ewald (13) at 155° K. Within experimental errors, the data of Hiza, et al, show excellent agreement with the data taken

in this work, although there appears to be more scatter in the Hiza data. The Ewald data agree relatively well with the data of this work at pressures below 40 atmospheres, whereas the xenon mole fractions measured by Ewald at pressures above 40 atmospheres are significantly higher than those measured in the present study. However, Ewald's composition data exhibit a larger scatter than the data of this work.

Krypton enhancement factors for the six isotherms of experimental measurements on the helium-krypton system are presented in Figures 9 and 10 and xenon enhancement factors for the four isotherms of experimental measurements on the helium-xenon system are presented in Figure 11. In each of these figures, vapor pressures determined from the least squares fit of the experimental data to Equation (12) were used to determine the enhancement factors. The smoothed enhancement factors obtained from the above-mentioned fit of the data to Equation (12) are also presented in these figures.

In Figure 10, krypton enhancement factors obtained at 105 and 115° K by the above method are compared with enhancement factors obtained by using the vapor pressures of Ziegler, et al (61). In neither case do the two sets of enhancement factor data differ by more than one per cent.

Krypton enhancement factors determined at 105 and 115° K from the experimental solid-vapor equilibrium measurements of Hiza, et al, (28) using Ziegler's vapor pressures are also presented in Figure 10. Xenon enhancement factors at 155 °K obtained from the solid-vapor equilibrium measurements of the present study and Ewald (13) using the vapor pressures from Ziegler, et al, (62) are presented in Figure 12. Although enhancement factors provide a more sensitive means of comparing solid-

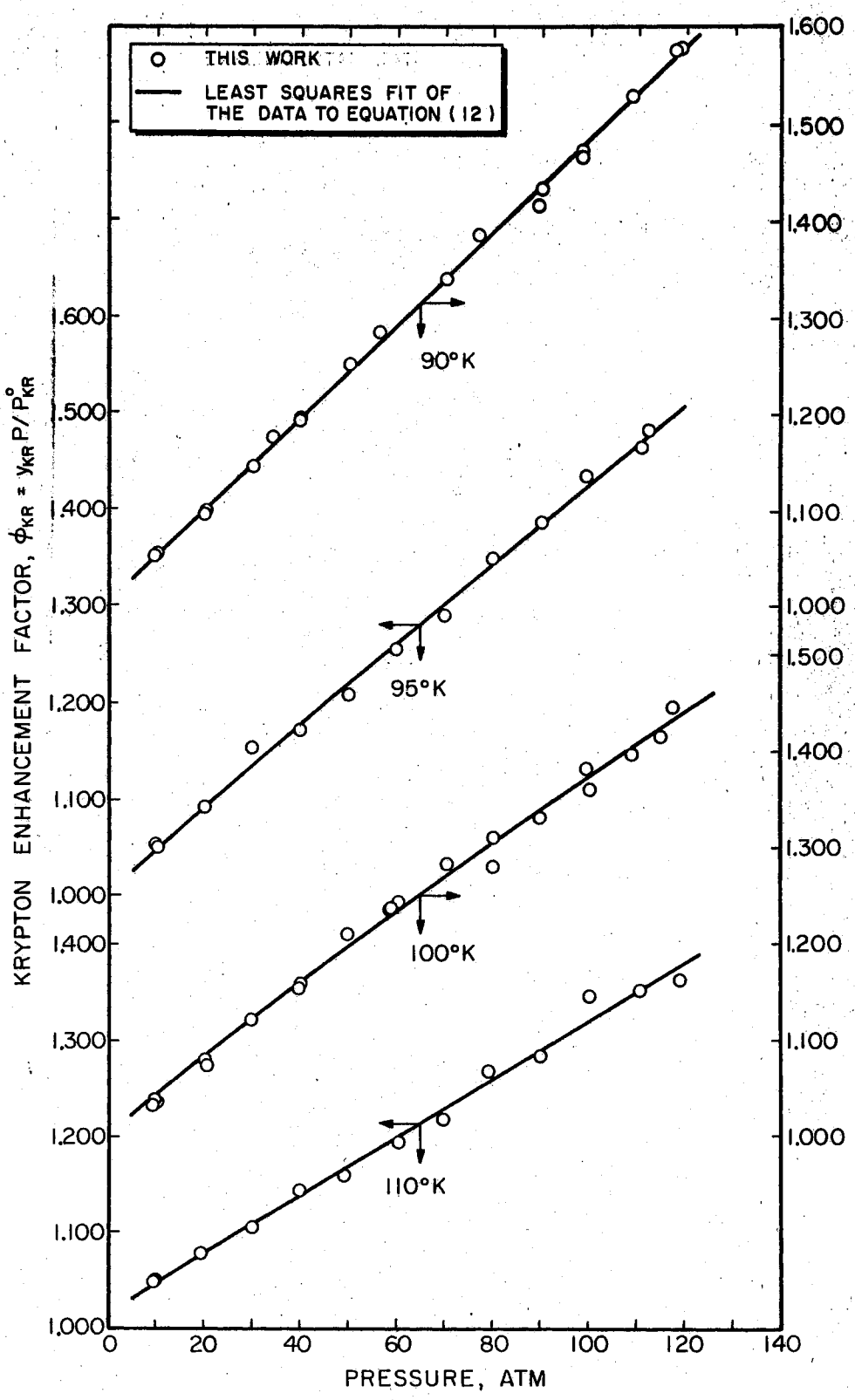

Figure 9. Krypton Enhancement Factors for the Helium-Krypton System

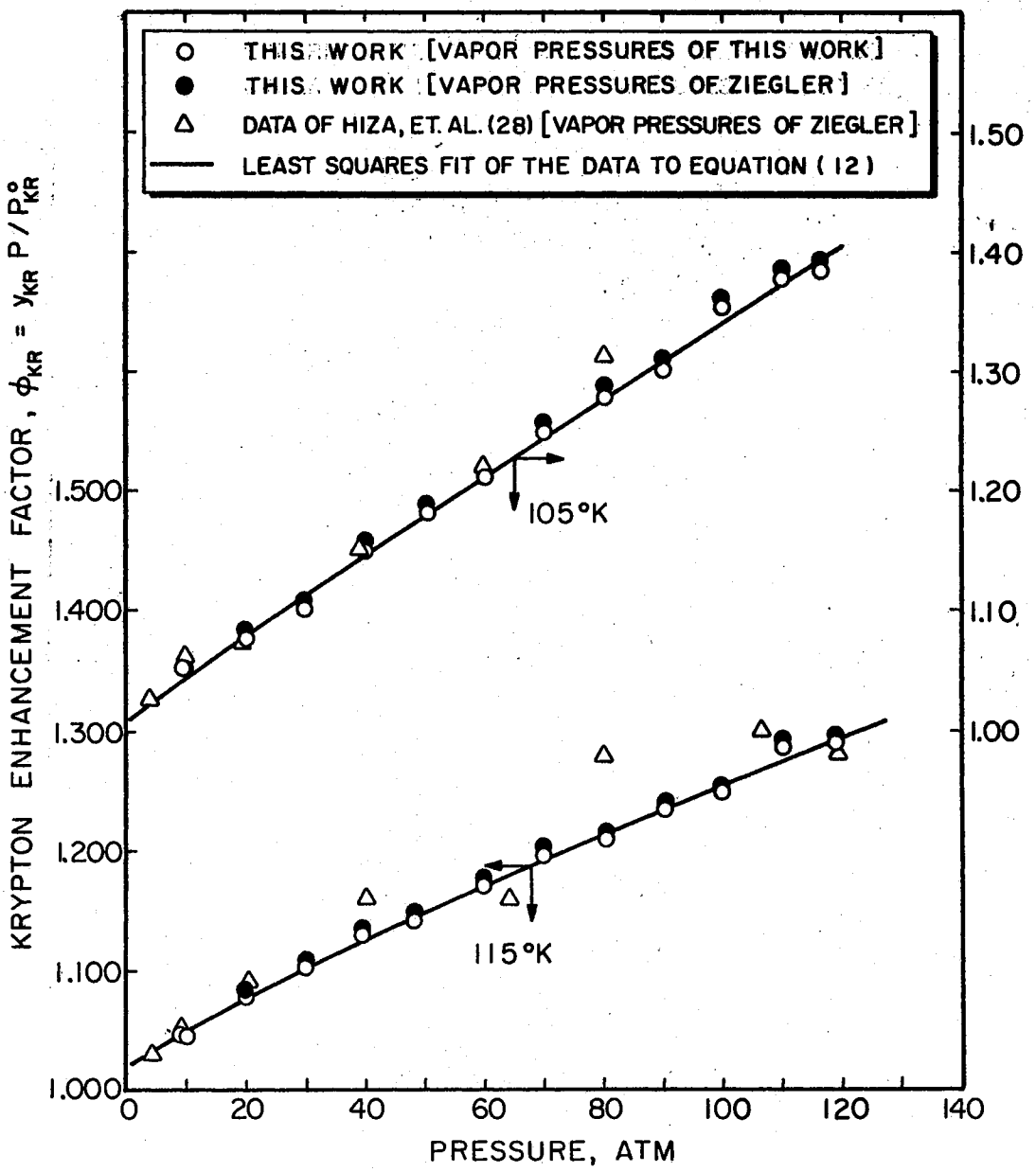

Figure 10. Krypton Enhancement Factors for the Helium-Krypton System

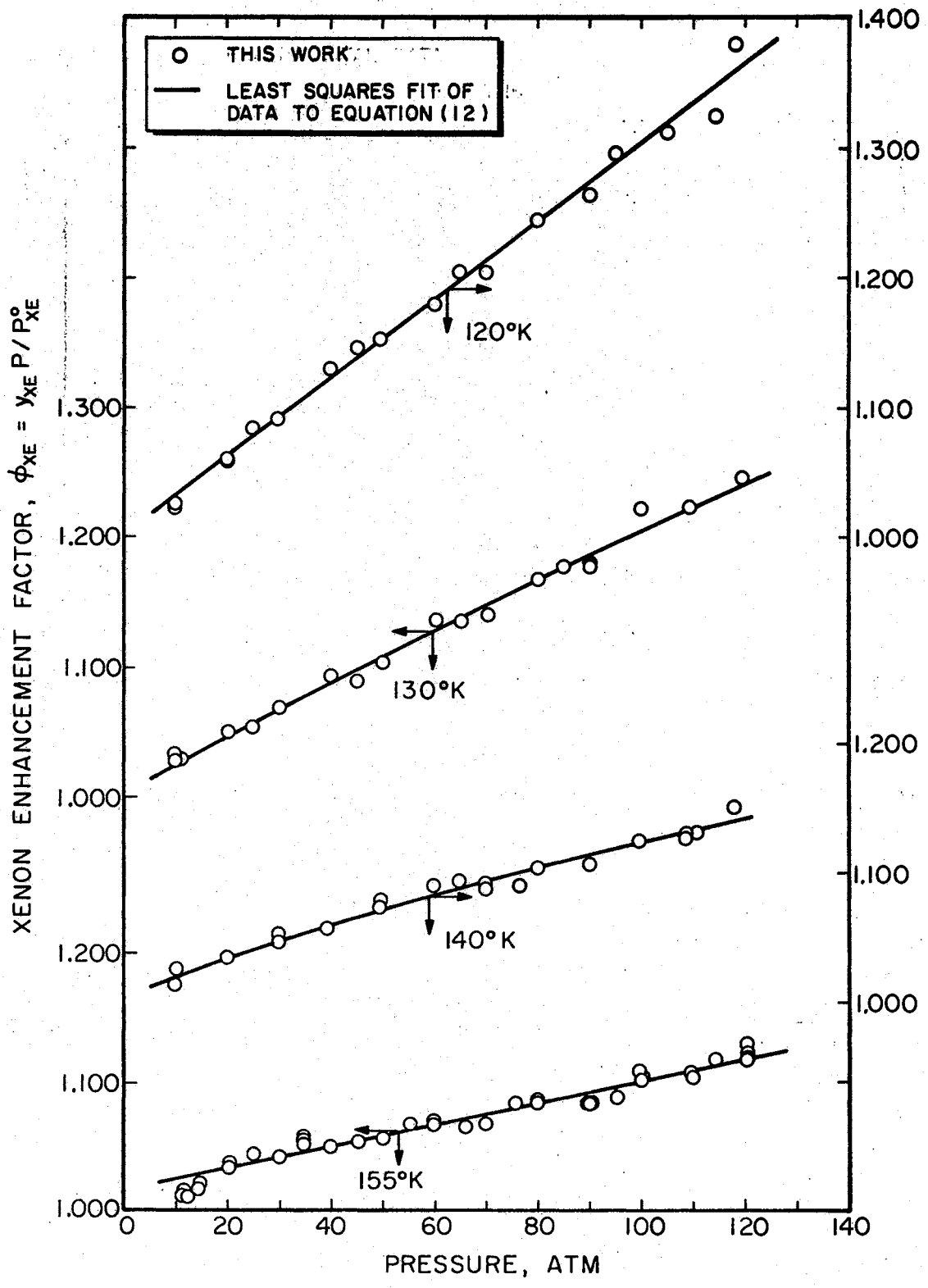

Figure 11. Xenon Enhancement Factors for the Helium-Xenon System

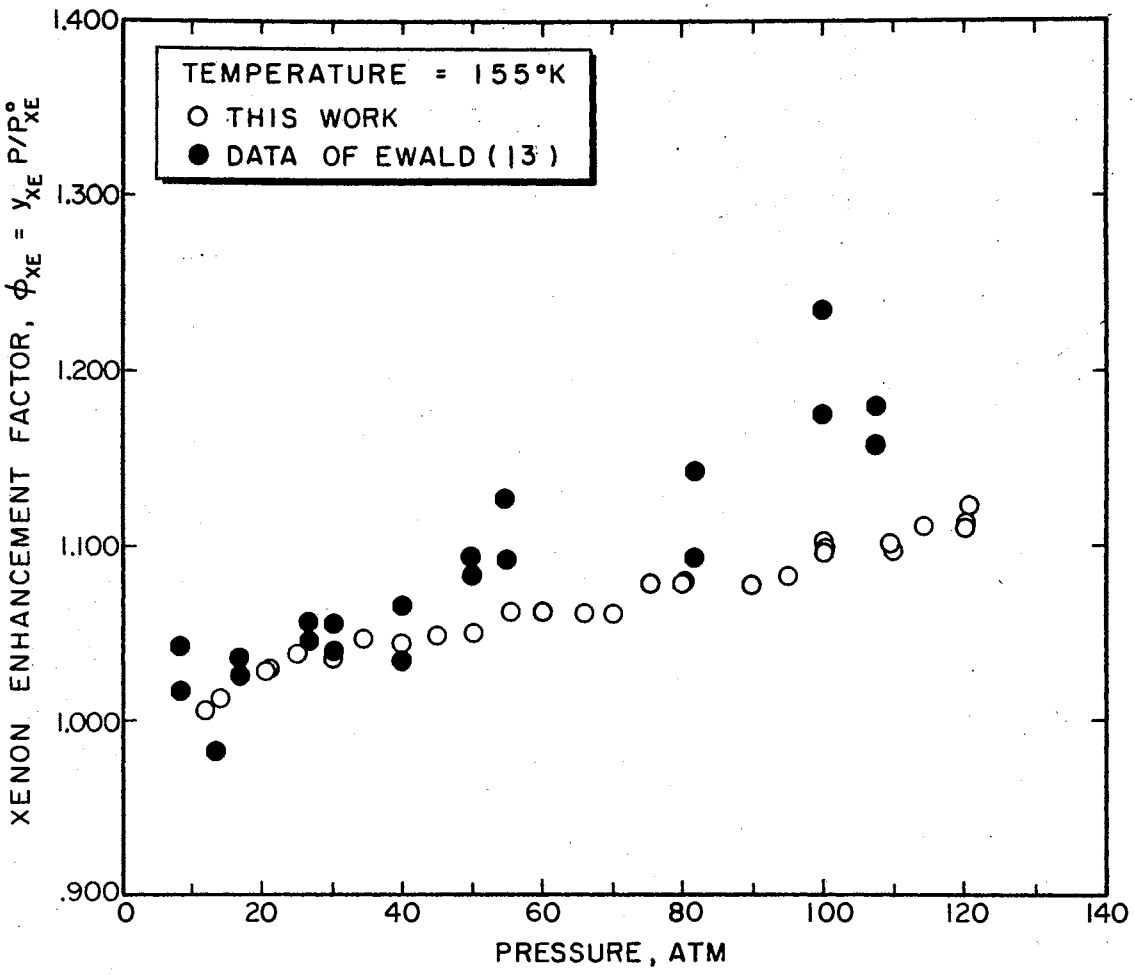

Figure 12. Xenon Enhancement Factors for the Helium-Xenon System

vapor equilibrium data, the results of the comparison of the data of this work with the data of other investigators have been reported previously in the discussion of Figures 7 and 8.

Data Reduction

Two different methods for reducing the experimental solid-vapor equilibrium data were employed. In the first method, the experimental data were fit to Equation (12) using both linear and non-linear regression techniques. In the second method, the experimental data were analyzed using the graphical procedure of Chiu and Canfield (7).

In order to determine the interaction virial coefficients B_{12} and C_{112} from the experimental solid-vapor equilibrium data using Equation (12), a knowledge of the following information is necessary:

(1) the pure component virial coefficients, B_{11}, B_{22}, C_{111}, and C_{222};

(2) the solid molar volume of component "2", $\bar{V}_{2S}$;

(3) the vapor pressure of solid component "2", P_2^o;

(4) a value of the interaction virial coefficient, C_{122}.

A complete survey of the data used in this work is presented in Appendix H.

Before the experimental solid-vapor equilibrium data were fit to Equation (12), the equation is rearranged to a more convenient form.

$$\ln \phi_2 - \bar{V}_{2S}(P - P_2^o)/RT - B_{22}P_2^o/RT - \ln Z_m + 2y_2B_{22}/\bar{V}_m \qquad (34)$$

$$+ (6y_1y_2C_{122} + 3y_2^2C_{222})/2\bar{V}_m^2 = - 2y_1B_{12}/\bar{V}_m - 3y_1^2C_{112}/2\bar{V}_m^2$$

Equation (34) may be written in the form

$$Y = -BX - CX^2 \tag{35}$$

where

$$Y = \ln \phi_2 - \bar{V}_{2S}(P - P_2^o)/RT - B_{22}P_2^o/RT - \ln Z_m + 2y_2B_{22}/\bar{V}_m + (6y_1y_2C_{122} + 3y_2^2C_{222})/2\bar{V}_m^2$$

$$X = y_1/\bar{V}_m$$

$$B = 2B_{12}$$

$$C = 3C_{112}/2$$

A least squares regression technique can now be applied to Equation (35) to obtain the constants B and C from the experimental data. When applying this technique, the criterion for the best fit is that the sum of the squares of the deviations between the experimental and calculated values of Y are a minimum, i.e.,

$$\sum(Y_{exp} - Y_{calc})^2/\varepsilon_Y^2 = \sum(Y_{exp} + BX + CX^2)^2/\varepsilon_Y^2 = \text{minimum} \tag{36}$$

where each experimental point is weighted by the error associated with Y, ε_Y. The complete error analysis needed to determine the appropriate values of ε_Y is presented in Appendix I.

If the sum of squares is to be a minimum, then the following relations must apply.

$$\frac{\partial}{\partial B}\left[\sum(Y_{exp} - Y_{calc})^2/\varepsilon_Y^2\right] = 0 \tag{37a}$$

$$\frac{\partial}{\partial C}\left[\sum(Y_{exp} - Y_{calc})^2/\varepsilon_Y^2\right] = 0 \tag{37b}$$

These two simultaneous relations may now be used to solve for B and C

which are given by

$$B = \frac{\Sigma(X^3/\varepsilon_Y^2)\Sigma(X^2Y/\varepsilon_Y^2) - \Sigma(X^4/\varepsilon_Y^2)\Sigma(XY/\varepsilon_Y^2)}{\Sigma(X^4/\varepsilon_Y^2)\Sigma(X^2/\varepsilon_Y^2) - \Sigma(X^3/\varepsilon_Y^2)\Sigma(X^3/\varepsilon_Y^2)} \tag{38}$$

$$C = \frac{\Sigma(X^3/\varepsilon_Y^2)\Sigma(XY/\varepsilon_Y^2) - \Sigma(X^4/\varepsilon_Y^2)\Sigma(X^2Y/\varepsilon_Y^2)}{\Sigma(X^4/\varepsilon_Y^2)\Sigma(X^2/\varepsilon_Y^2) - \Sigma(X^3/\varepsilon_Y^2)\Sigma(X^3/\varepsilon_Y^2)} \tag{39}$$

The subscripts have been left off the X's, Y's, ε_Y's and summation signs for brevity, but the summation sign implies summation over all data points used in the fit.

All the information necessary to calculate Y and X are directly available except Z_m and $\bar{V}_m$. These quantities must be evaluated from the virial equation to be consistent with the derivation of Equation (12). In order to determine mixture PVT properties from the virial equation, the mixture virial coefficients, B_m and C_m, must be known for a binary mixture.

$$B_m = y_1^2 B_{11} + 2y_1y_2B_{12} + y_2^2B_{22} \tag{40}$$

$$C_m = y_1^3 C_{111} + 3y_1^2y_2C_{112} + 3y_1y_2^2C_{122} + y_2^3C_{222} \tag{41}$$

However, B_{12} and C_{112} are the coefficients to be determined by the above regression procedure. Thus, the problem is, in reality, a non-linear one. Fortunately, because the value of $\bar{V}_m$ (or Z_m) is relatively insensitive to the values of B_{12} and C_{112}, the problem can be linearized.

A simple iterative procedure can be used to solve Equation (35). For the first iteration, values of B_{12} and C_{112} must be assumed in order to calculate B_m and C_m and thus, Z_m and $\bar{V}_m$. Using these assumed values

of B_{12} and C_{112}, new values of B_{12} and C_{112} are calculated from Equations (38) and (39) and compared with the assumed values. If the assumed and calculated values of B_{12} and C_{112} do not agree, then the calculated values are used as the new assumed values and the procedure is repeated. This iterative process is continued until the assumed and calculated values of B_{12} agree within ±0.0001 cc/g-mole and the assumed and calculated values of C_{112} agree within ±1.0 $(cc/g\text{-}mole)^2$. In all cases, only 3-5 iterations were required for convergence in determining the values of B_{12} and C_{112}, a good indication of the insensitivity of $\bar{V}_m$ (or Z_m) to the values of B_{12} and C_{112}.

The above analysis requires a source of accurate vapor pressure data, because, as will be shown later, the interaction virial coefficients, B_{12} and C_{112}, are more sensitive to vapor pressure than the other input data. In order to avoid determining which vapor pressure data are the best, a non-linear least squares regression procedure was employed to obtain both the vapor pressure and the interaction virials (B_{12} and C_{112}) from Equation (12) using the experimental solid-vapor equilibrium data.

In the non-linear regression procedure, a two parameter relation is assumed to approximate the vapor pressure curve over the temperature range of interest. A typical form of a vapor pressure curve is given by

$$\log P^o = A - B/T \tag{42}$$

Equation (42) can be modified to

$$\log P^o - \log P^o_{tp} = \beta\left(\frac{1}{T} - \frac{1}{T_{tp}}\right) \tag{43}$$

where

P^o_{tp} = vapor pressure at the triple point

T_{tp} = temperature of the triple point

Equation (42) or (43) can be further modified to an approximate form of the vapor pressure curve presented by Ziegler, et al (61,62) by adding a deviation function to Equation (43)

$$\log P^o = \log P^o_{tp} + \beta\left(\frac{1}{T} - \frac{1}{T_{tp}}\right) + \text{Deviation} \qquad (44)$$

The deviation function in Equation (44) is obtained from the following procedure:

(1) the vapor pressure data of Ziegler over the temperature range of interest are fit to Equation (42) by using the endpoints to determine the constants A and B

(2) the non-linearity associated with the fit, i.e., the difference between the experimental and calculated vapor pressures, is set equal to the deviation function (for the two endpoint temperatures, the deviation function is zero).

This procedure, in effect, allows for the non-linearity in the log (vapor pressure)-reciprocal temperature relationship, establishing this non-linearity from the vapor pressure work of Ziegler, et al.

Equation (44) is the two parameter relation which is used in this work to approximate the vapor pressure curve. The two unknowns are the endpoint pressure (triple point pressure in this work) and the constant β. The experimental solid-vapor equilibrium data are used to determine the best values of these two parameters in addition to the interaction virials (B_{12} and C_{112}). This technique was used to determine the vapor

pressures rather than regressing a value at each temperature in order to decrease the total number of parameters to be determined from the experimental data.

The major difference between the non-linear and linear regression methods is that, in the non-linear regression procedure, the parameters of the vapor pressure curve and the interaction virials are determined from the minimum overall sum of squares; i.e., the minimum total of the sums of squares of the individual linear regression problems at each temperature. When known vapor pressure data are used (linear problem), the minimum sum of squares at each temperature determines the fit independent of the results for the other isotherms.

The non-linear regression problem was solved by a pattern search technique. The parameters of the vapor pressure curve were assumed and the interaction virial coefficients (B_{12} and C_{112}) were regressed at each temperature using the previously mentioned linear method. Another set of vapor pressure parameters were assumed and the above procedure repeated. In this manner, a pattern search was conducted until the overall sum of squares was a minimum. An example of this kind of search is presented in Table IV for the helium-xenon system.

The krypton and xenon vapor pressures which were determined by the above non-linear regression technique have been presented in Appendix H (Table XXV) where they were compared with the experimental data of Ziegler, et al (61, 62) and Leming and Pollack (32). A graphical comparison is given in Figure 13 where the vapor pressures calculated from the non-linear regression of the solid-vapor equilibrium data are compared to the experimental vapor pressures.

The experimental krypton vapor pressures of Ziegler, et al (61)

TABLE IV

EXAMPLE OF THE PATTERN SEARCH TECHNIQUE USED TO SOLVE EQUATION (35)

Sum of Squares, Dimensionless

Vapor Pressure mmHg \ β	-809.50	-809.40	-809.30	-809.20	-809.10	-809.00	-808.90
379.75	2.0247×10^{-4}	2.0244×10^{-4}	2.0252×10^{-4}	2.0268×10^{-4}			
379.50			2.02345×10^{-4}	$2.02342^{*} \times 10^{-4}$	2.02420×10^{-4}		
379.25				2.0236×10^{-4}	2.0237×10^{-4}	2.0246×10^{-4}	
379.00						2.0250×10^{-4}	2.0251×10^{-4}

*This value represents the minimum overall sum of squares.

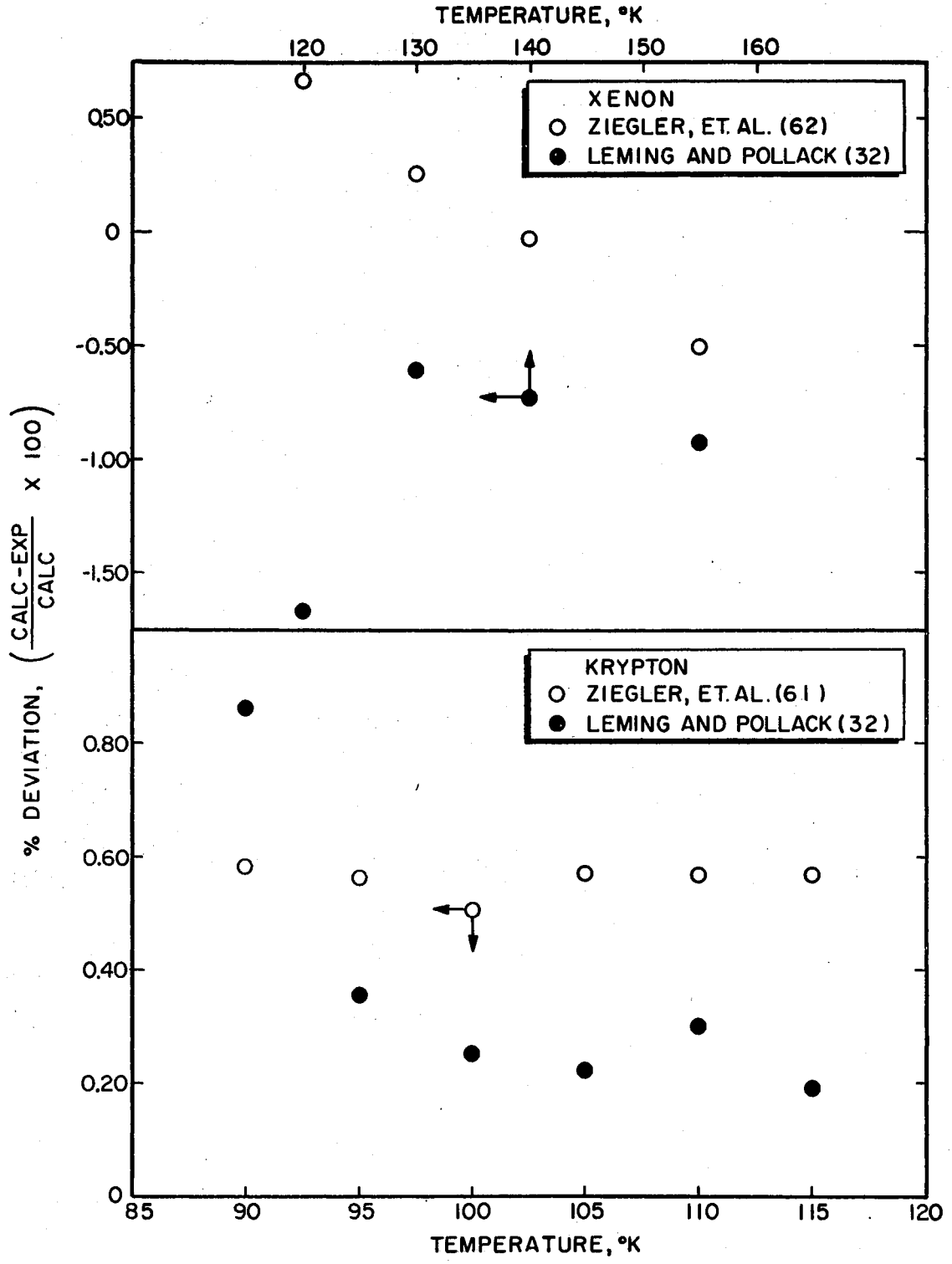

Figure 13. Comparison of Calculated and Experimental Vapor Pressures of Solid Krypton and Xenon

are all 0.5 to 0.6% lower than the values calculated in this work whereas the data of Leming and Pollack (32) are only 0.2 to 0.4% lower than the calculated values with the exception of the value at 90° K. The experimental xenon vapor pressures of Ziegler, et al (62) cut diagonally across the values calculated in this study, i.e., the values of Ziegler range from 0.6% below the calculated values at 120° K to 0.6% above the calculated values at 155° K. The experimental data of Leming and Pollack (32) are 0.6 to 0.9% above the calculated values except at 120° K where the data point is 1.7% above the calculated value.

The least squares regression program used in this work is presented in Appendix J. Typical examples of the least squares regression of the experimental solid-vapor equilibrium data to Equation (35) are presented in Figures 14 and 15. The error bands associated with each experimental point are included to demonstrate the ability of Equation (35) to fit the experimental data within its estimated experimental uncertainty. With few exceptions, the smoothed curves pass through the error bands on the data points.

The smoothed enhancement factor data for the helium-krypton and helium-xenon systems, determined from the least squares fit of the experimnetal data to Equation (12), are presented in Figures 16 and 17. Temperature cross-plots of the smoothed enhancement factor data of both the helium-krypton and helium-xenon systems appear in Figures 18 and 19. Smoothed curves were drawn through the cross-plotted data by inspection. Careful examination of these figures indicates that, although some systematic deviations are apparent among the isotherms, the deviations are within the experimental uncertainty of the data with the exception of the higher pressure data (above 80 atm).

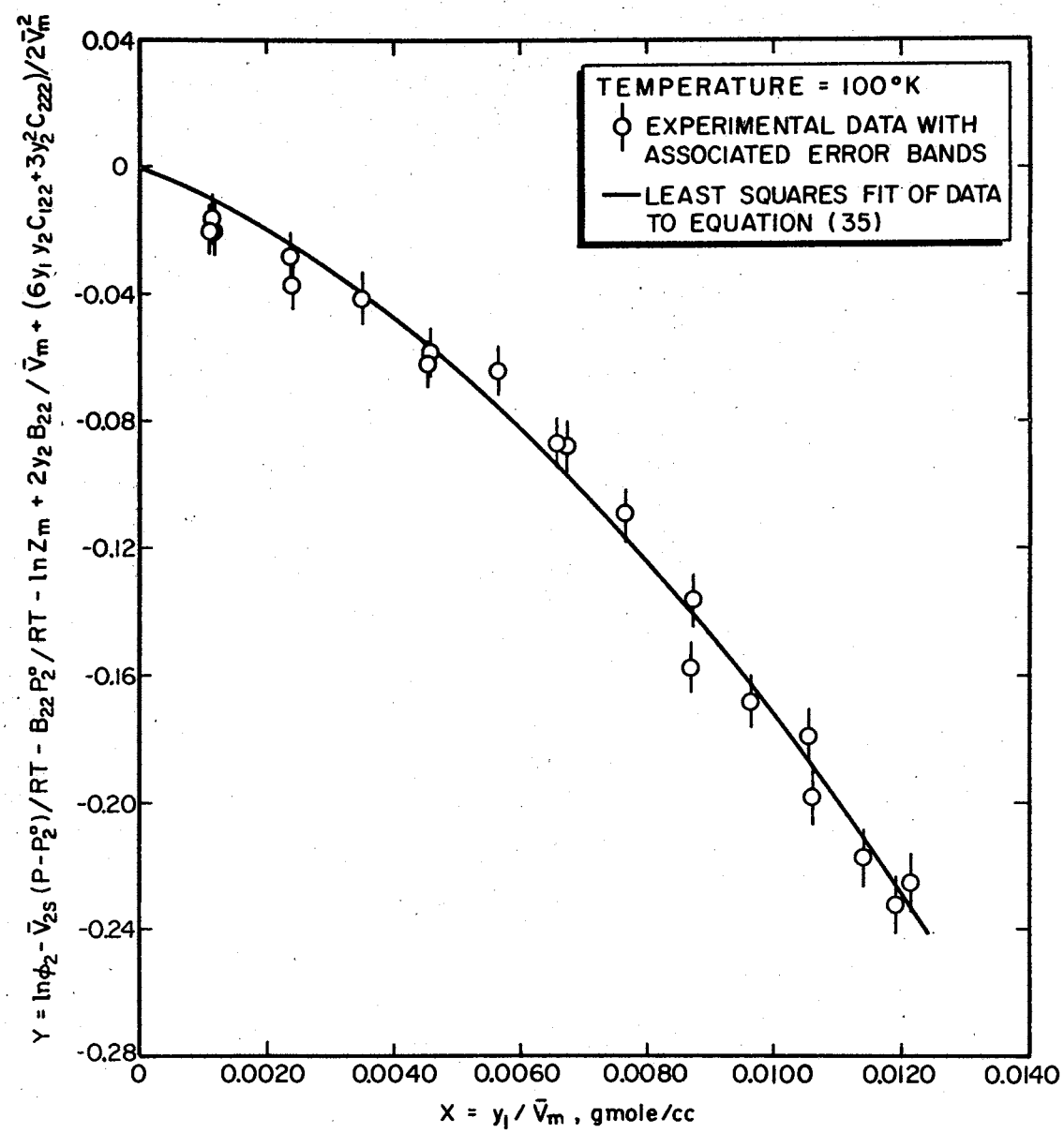

Figure 14. Example of the Least Squares Regression of the Experimental Data to Equation (35) for the Helium-Krypton System

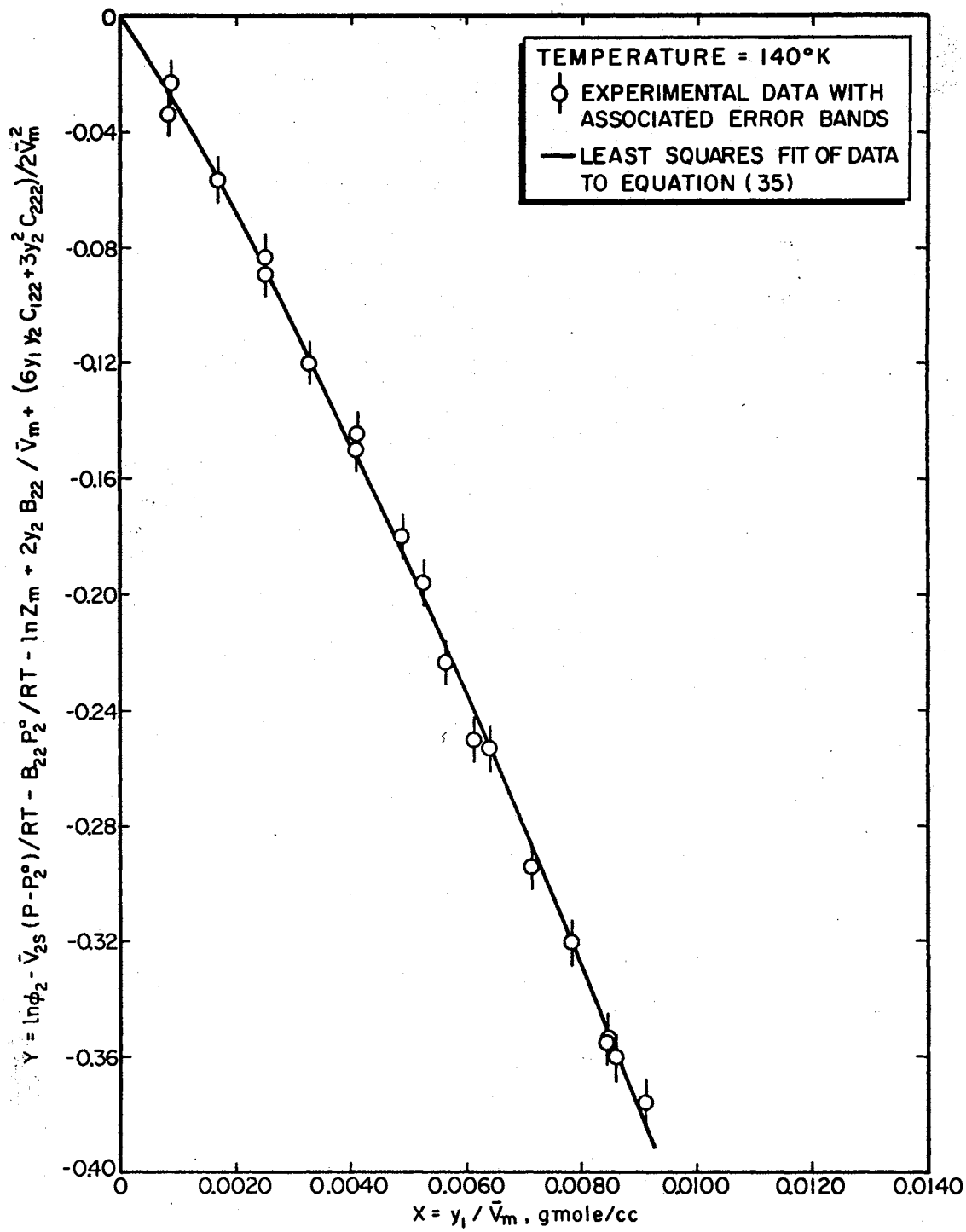

Figure 15. Example of the Least Squares Regression of the Experimental Data to Equation (35) for the Helium-Xenon System

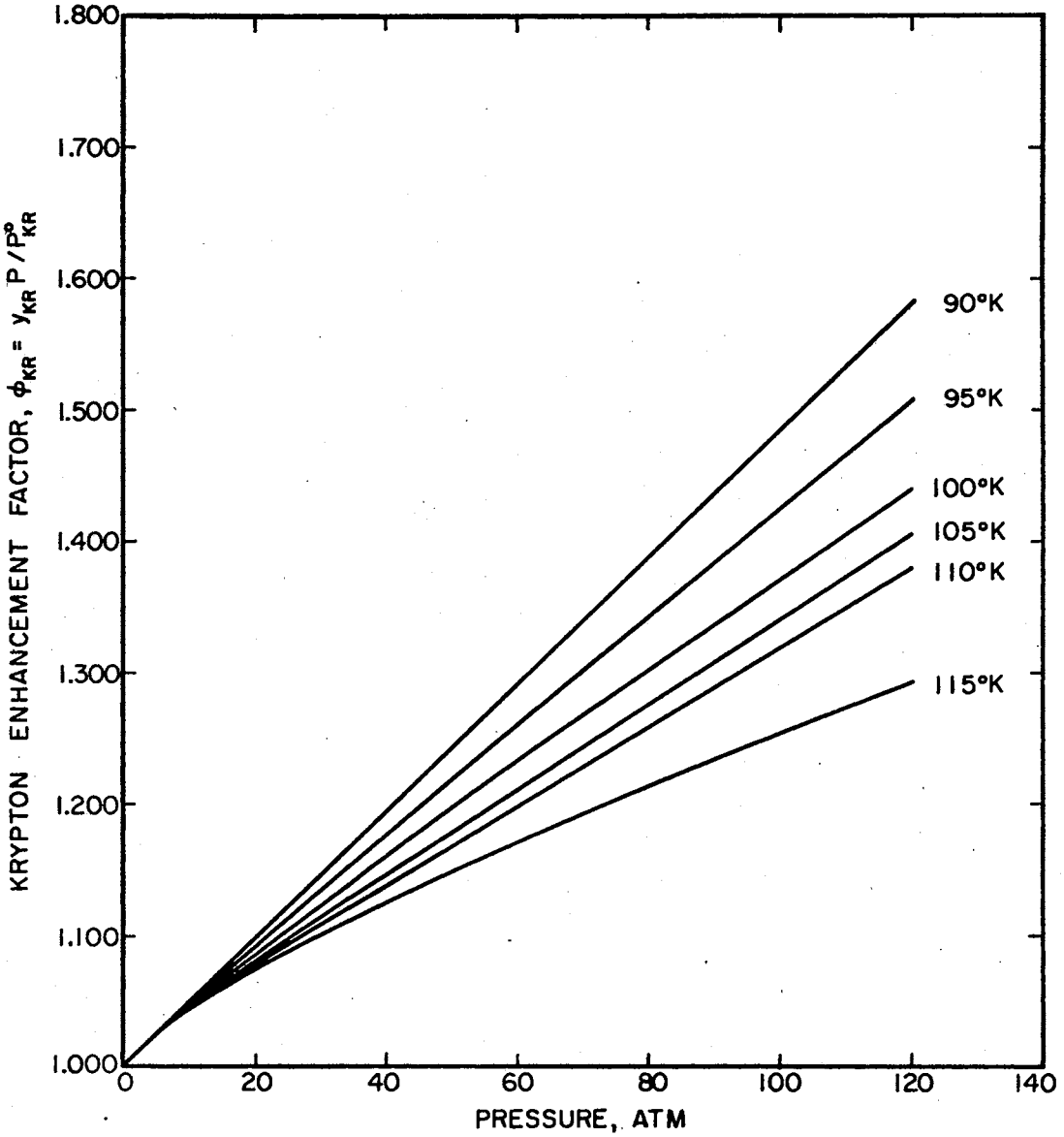

Figure 16. Smoothed Enhancement Factors for the Helium-Krypton System from the Least Squares Fit of the Experimental Data to Equation (12)

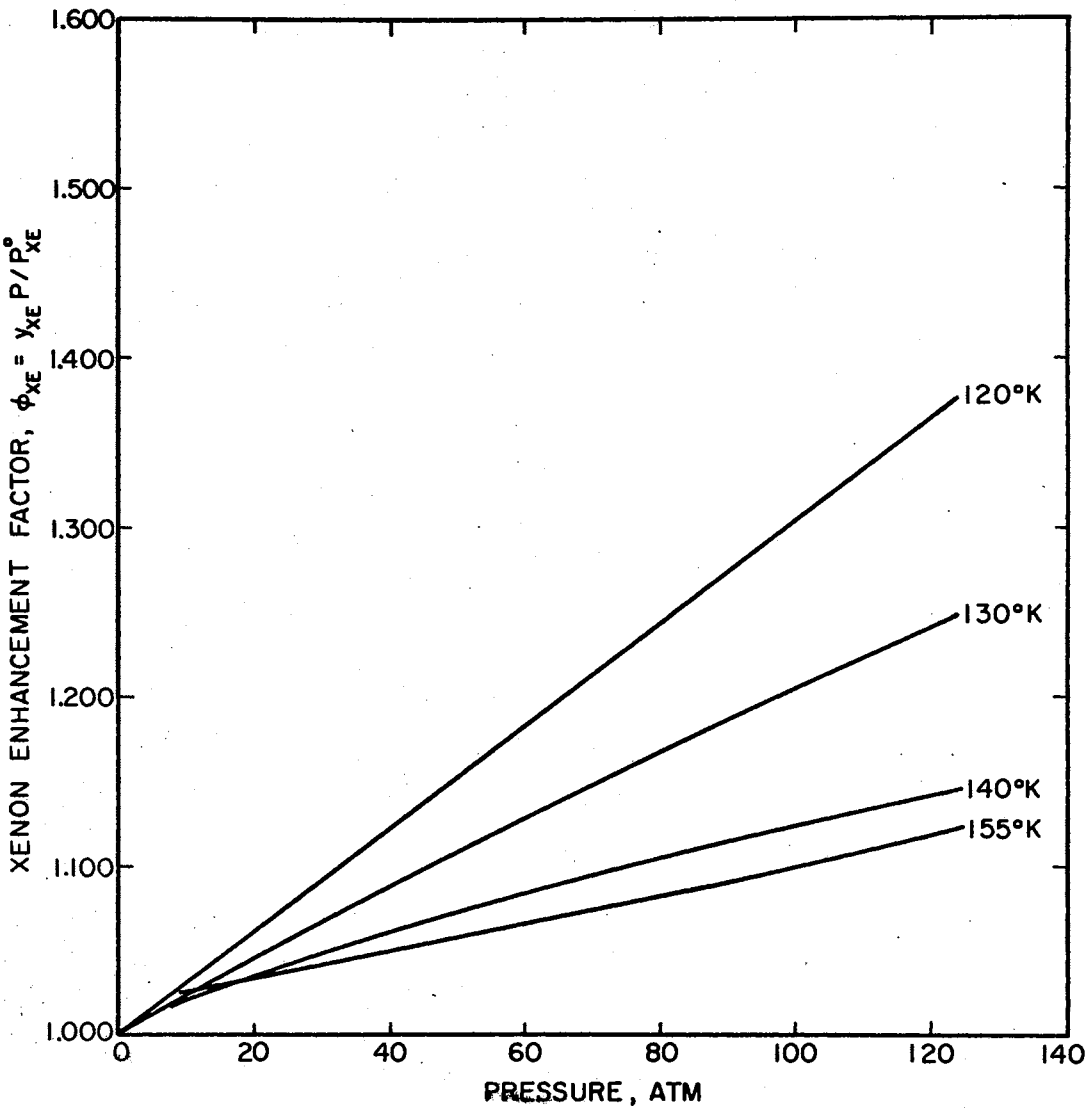

Figure 17. Smoothed Enhancement Factors for the Helium-Xenon System from the Least Squares Fit of the Experimental Data to Equation (12)

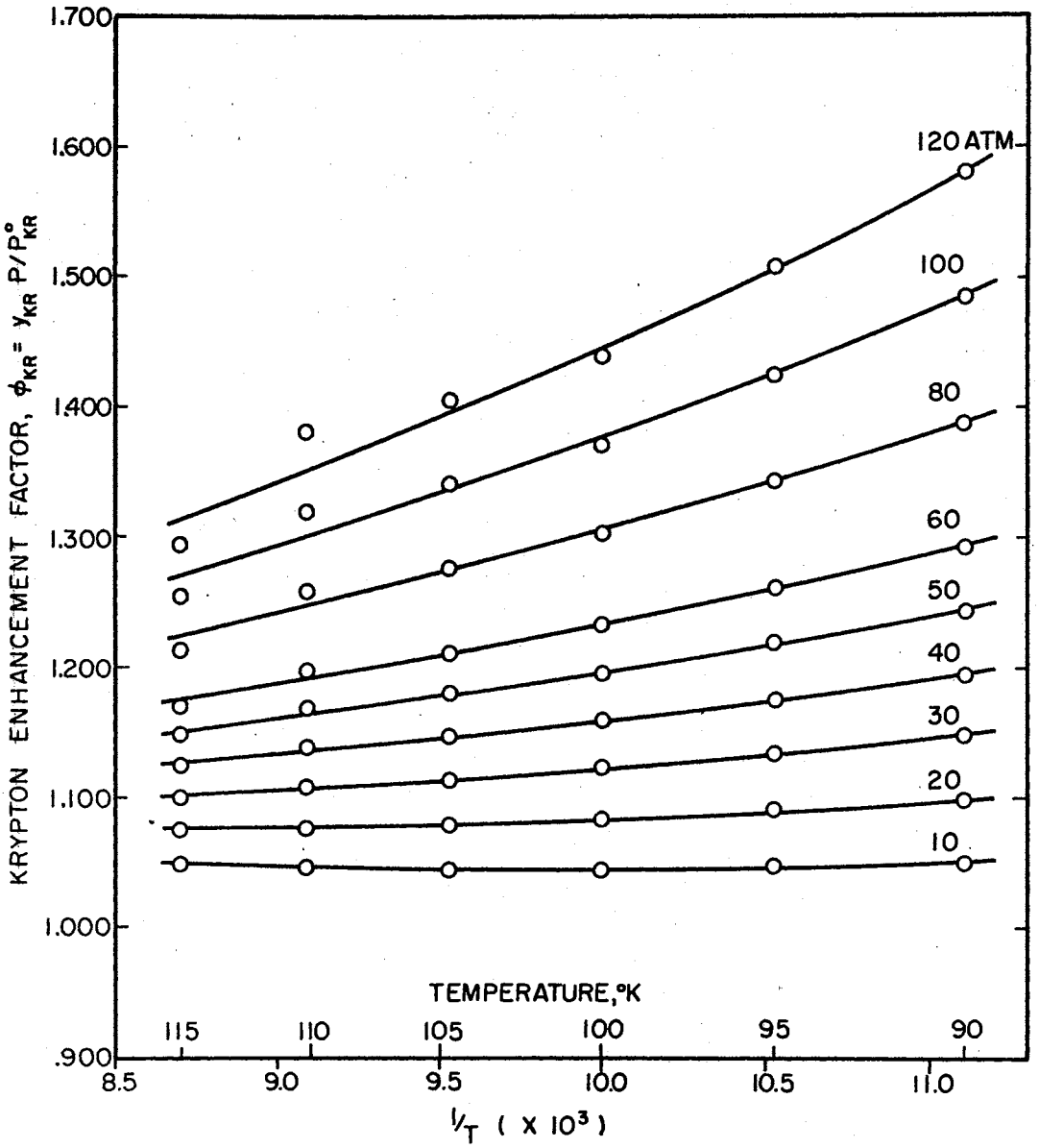

Figure 18. Temperature Cross-Plot of the Smoothed Enhancement Factor Data for the Helium-Krypton System

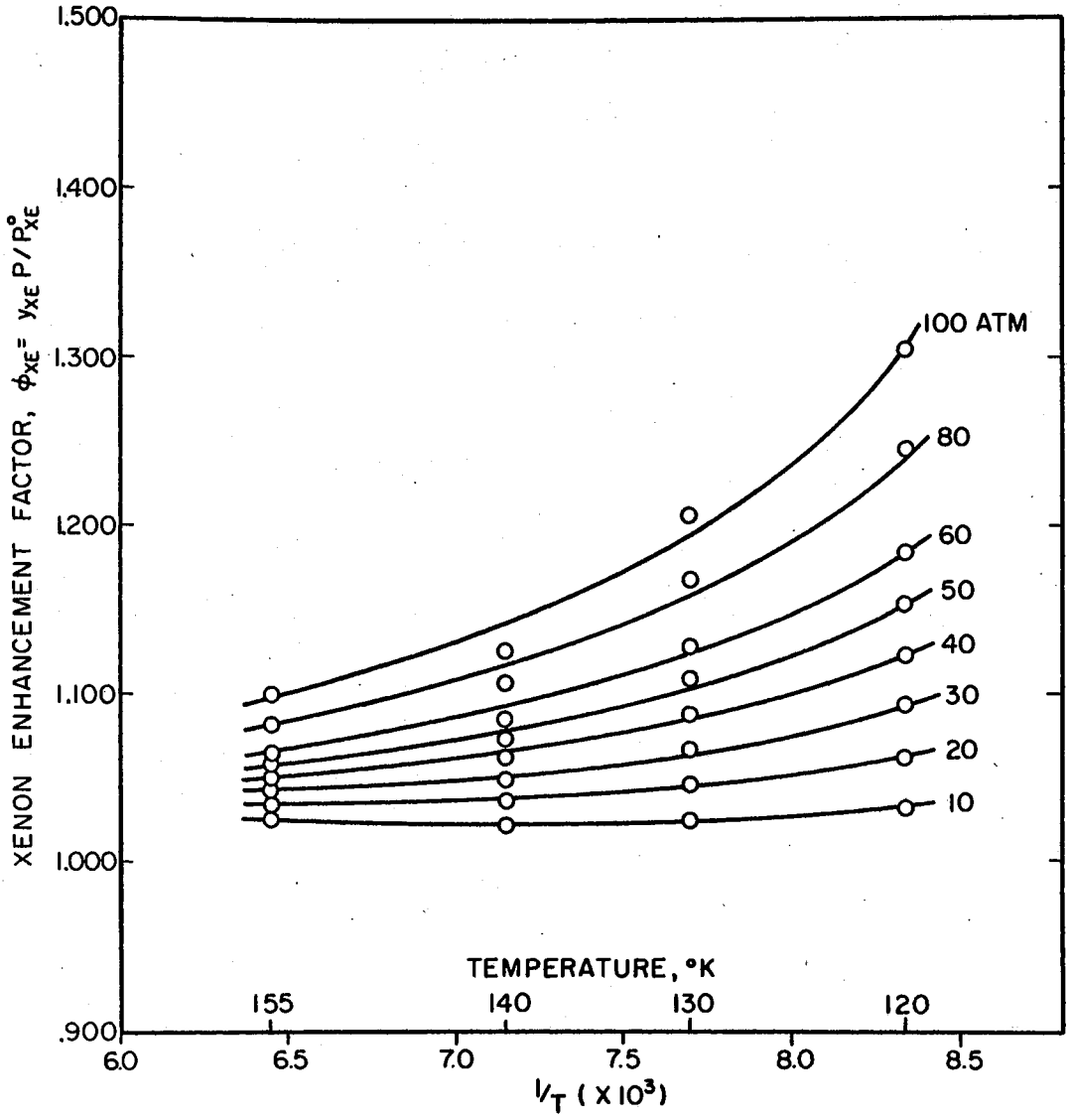

Figure 19. Temperature Cross-Plot of the Smoothed Enhancement Factor Data for the Helium-Xenon System

Another method of analyzing solid-vapor equilibrium data is the graphical procedure of Chiu and Canfield (7). Equation (15) was used to calculate values of the ERT function from the experimental data. These ERT values were plotted as a function of pressure [see Equation (16)] and extrapolated to the vapor pressure to obtain the value of $(B_{11} - 2B_{12})$. Chiu and Canfield suggested using an optimum extrapolation pressure, P_{oe}, where the value of $\left| \frac{FP}{ERT} \right|$ is a minimum. However, the value of P_{oe} and the vapor pressure are both quite small for solid-vapor equilibrium data and thus, in this work, the vapor pressure was used as the extrapolation pressure. The error associated with each value of ERT was also calculated using an error analysis similar to the one presented in Appendix I.

Two typical examples of the application of Chiu and Canfield's graphical technique to the solid-vapor equilibrium data of the helium-krypton system are presented in Figures 20 and 21. The smooth curves are placed through the data by inspection. The main difficulty in using this method is immediately obvious, i.e., the large errors associated with the data at lower pressures. The errors associated with the values of ERT also increase with increasing temperature. Thus, extrapolating the ERT versus pressure curve by inspection to obtain the second interaction coefficient can lead to an undesirable degree of uncertainty. Because of the high uncertainty associated with the values of ERT at low pressures, values of B_{12} determined from the Chiu and Canfield method for any system could possibly be in error by as much as 2 to 5 cc/g-mole.

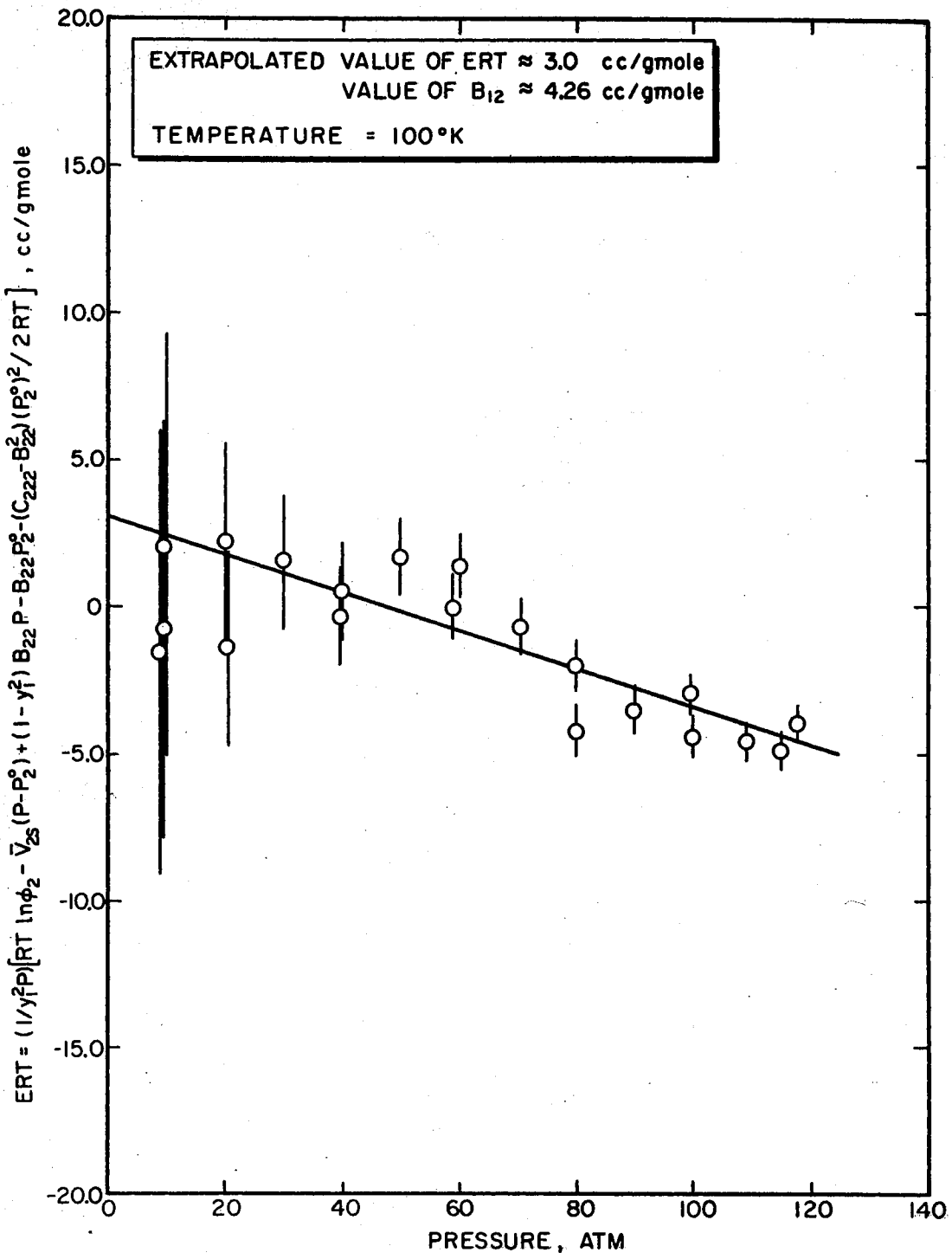

Figure 20. Example of the Application of the Chiu and Canfield Technique to Solid-Vapor Equilibrium Data for the Helium-Krypton System

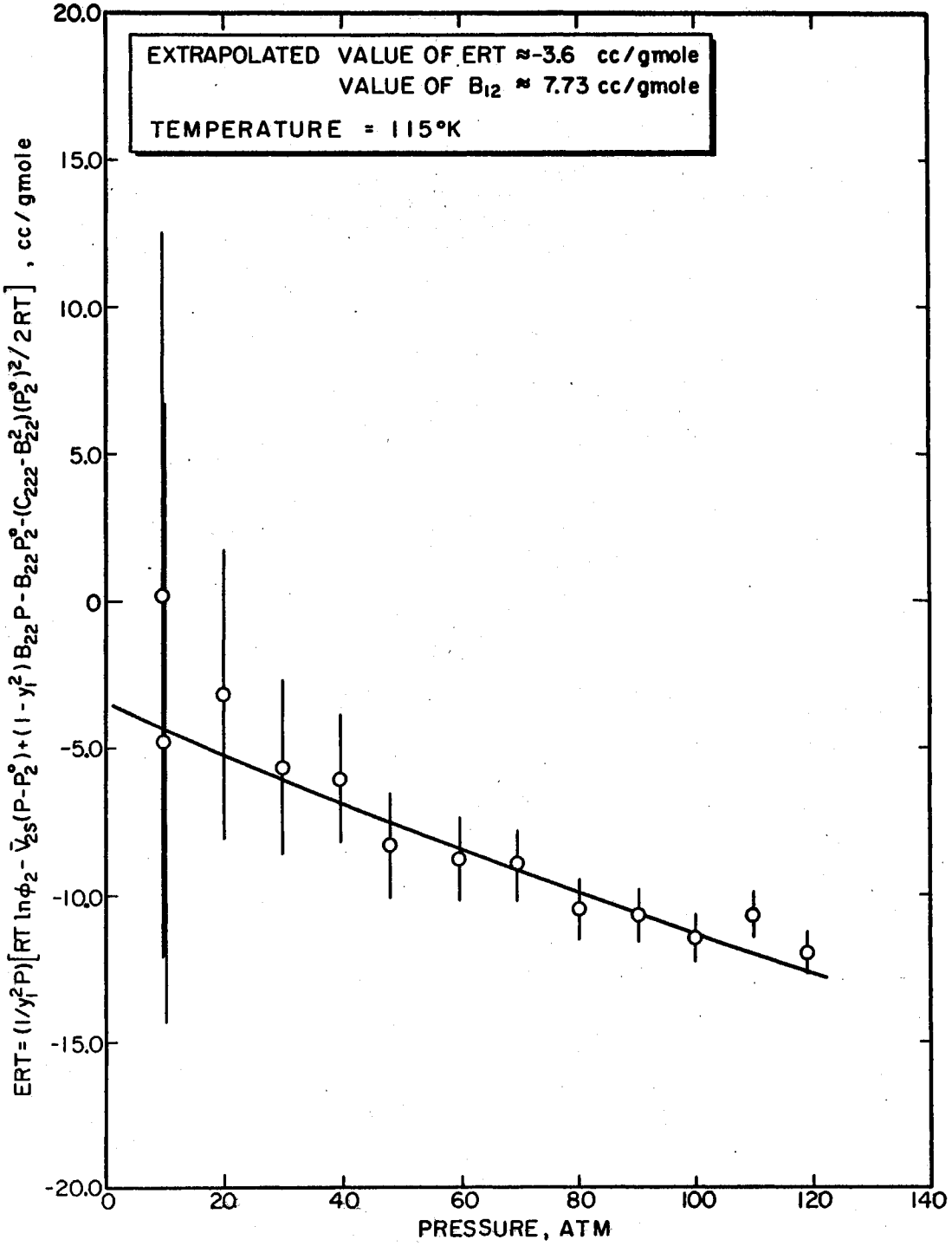

Figure 21. Example of the Application of the Chiu and Canfield Technique to Solid-Vapor Equilibrium Data for the Helium-Krypton System

CHAPTER VII

DISCUSSION OF RESULTS

A discussion of the results of the analysis of the experimental measurements made in this study is presented in this chapter. The interaction virial coefficients determined from the procedures discussed in the previous chapter are presented and discussed. The B_{12} values obtained in the present study are compared with the data of other investigators and the results are analyzed. Finally, a discussion is presented on the testing of various combining rules for determining interaction potential parameters using all available B_{12} data on the systems studied in this work.

Interaction Virial Coefficients

The second interaction virial coefficients (B_{12}'s) determined by the procedures discussed in the previous chapter are presented in Table V. Interaction virials for both the helium-krypton and helium-xenon systems are tabulated. For every case in which a least squares regression technique was used to determine the interaction virial coefficient, B_{12}, the standard deviation is also presented.

For the helium-krypton system, the second interaction virial coefficients determined by each of the various methods of data reduction agreed with one another within 1.0 cc/g-mole, including the B_{12} values obtained by the graphical procedure of Chiu and Canfield (although

TABLE V

EXPERIMENTAL SECOND INTERACTION VIRIAL COEFFICIENTS (B_{12}'s)

Helium-Krypton System				
Temperature °K	$B_{12}(1)$ cc/g-mole	$B_{12}(2)$ cc/g-mole	$B_{12}(3)$ cc/g-mole	$B_{12}(4)$ cc/g-mole
90	1.73(±0.61)	0.85(±0.62)	0.39(±0.65)	1.57
95	2.97(±1.13)	2.04(±1.28)	2.37(±1.22)	2.92
100	4.06(±1.03)	3.19(±0.94)	3.60(±0.97)	4.26
105	5.66(±0.99)	4.67(±1.10)	5.28(±1.02)	5.33
110	6.99(±1.34)	6.00(±1.41)	6.56(±1.36)	6.38
115	8.52(±0.66)	7.50(±0.72)	8.18(±0.66)	7.73

Helium-Xenon System			
Temperature °K	$B_{12}(1)$ cc/g-mole	$B_{12}(2)$ cc/g-mole	$B_{12}(3)$ cc/g-mole
120	9.38(±0.96)	8.11(±0.91)	12.64(±1.40)
130	13.05(±0.85)	12.49(±0.91)	14.40(±0.77)
140	16.42(±0.85)	16.52(±0.85)	17.81(±0.83)
155	20.47(±0.82)	21.63(±0.89)	22.58(±0.96)

(1) Determined simultaneously with the vapor pressure by a nonlinear regression technique from Equation (35)

(2) Determined by a linear regression technique from Equation (35) using the vapor pressure data of Ziegler, et al (61, 62)

(3) Determined by a linear regression technique from Equation (35) using the vapor pressure data of Leming and Pollack (32)

(4) Determined by the graphical procedure of Chiu and Canfield (7) using the vapor pressure data of Ziegler, et al (61)

these values required some artistry). However, for the helium-xenon system, the B_{12}'s calculated using Leming and Pollack's vapor pressure data disagreed with the B_{12}'s obtained from the other regression methods by significantly more than 1.0 cc/g-mole, especially at the lower temperatures.

Although the principle objective of analyzing the solid-vapor equilibrium measurements was to determine accurate second interaction virial coefficient data, third interaction virial coefficients (C_{112}) were also determined from the experimental data using Equation (35). The values of C_{112} determined by the various regression techniques of data reduction are presented in Table VI. As can be seen in this table, the C_{112}'s exhibit a significant amount of scatter and have a large uncertainty associated with them. Although the values of C_{112} should decrease slightly with increasing temperature in the reduced temperature ranges studied in this work, the excessive scatter and large standard deviations of the C_{112} data precluded any conclusions as to the trend of the C_{112} data of the present study.

At this point, the effect of the various quantities in Equation (12) on the regressed values of the second interaction virial coefficient should be discussed. Calculations of these effects are detailed in Appendix K. The results show that the only variable having a large effect on the B_{12} values is the vapor pressure of the condensed component. Upon careful examination of Table XXV (or Figure 13) and Table V, a 0.5 to 0.6% change in vapor pressure produces a change in the value of B_{12} of approximately 1.0 cc/g-mole for either the helium-krypton or helium-xenon systems.

Because of the sensitivity of the value of B_{12} to the vapor pres-

TABLE VI

EXPERIMENTAL THIRD INTERACTION VIRIAL COEFFICIENTS (C_{112}'s)

Helium-Krypton System			
Temperature °K	$C_{112}^{(1)}$ $(cc/g\text{-}mole)^2$	$C_{112}^{(2)}$ $(cc/g\text{-}mole)^2$	$C_{112}^{(3)}$ $(cc/g\text{-}mole)^2$
90	573(±57)	646(±58)	684(±61)
95	572(±113)	654(±129)	625(±123)
100	611(±106)	689(±97)	652(±101)
105	517(±106)	610(±118)	553(±110)
110	439(±147)	534(±155)	480(±150)
115	606(±75)	709(±82)	640(±76)
Helium-Xenon System			
Temperature °K	$C_{112}^{(1)}$ $(cc/g\text{-}mole)^2$	$C_{112}^{(2)}$ $(cc/g\text{-}mole)^2$	$C_{112}^{(3)}$ $(cc/g\text{-}mole)^2$
120	516(±115)	649(±109)	173(±167)
130	564(±114)	629(±122)	405(±103)
140	683(±114)	672(±114)	524(±112)
155	296(±118)	148(±128)	25(±139)

(1) Determined simultaneously with the vapor pressure by a non-linear regression technique from Equation (35)

(2) Determined by a linear regression technique from Equation (35) using the vapor pressure data of Ziegler, et al (61, 62)

(3) Determined by a linear regression technique from Equation (35) using the vapor pressure data of Leming and Pollack (32)

sure of the condensed component, the previously mentioned non-linear regression technique was used to simultaneously determine the condensed component vapor pressure as well as the interaction virial coefficients, B_{12} and C_{112}. This technique eliminated the necessity of choosing between the various sets of experimental vapor pressure data. The values of B_{12} obtained by the non-linear technique are the values that are used in all further discussion; i.e., comparison of the experimental B_{12}'s with those of other investigators, testing combination rules, etc.

In Figures 22, 23 and 24, the B_{12}'s obtained for the helium-krypton system in this work are compared with the data of Brewer (2) and Dillard (11). In Figure 25, the B_{12}'s obtained for the helium-xenon system in this study are compared with the data of Brewer (2). Also appearing in these figures are the smoothed B_{12} curves obtained from the fit of the B_{12} data to the Dymond-Alder potential.

The recently-proposed potential of Dymond and Alder (12) is a tabular presentation of the reduced potential, $U^*(R) = U(r)/\varepsilon$, as a function of the reduced distance, $R = r/\sigma$. The form of the potential was established to yield a simultaneous fit to the available gas phase equilibrium and transport properties of argon. Thus, this potential form does not suffer as do other simple potentials from inadequacies due to restrictions imposed by an analytical form. Although the potential was developed for argon, Lin and Robinson (35) have recently applied the potential to other rare gases within the framework of two-parameter corresponding states theory.

A more meaningful comparison of the B_{12} values obtained in this work to the B_{12} data of the other investigators is presented in Figures 26 and 27. In these figures, the deviations between the experimental values

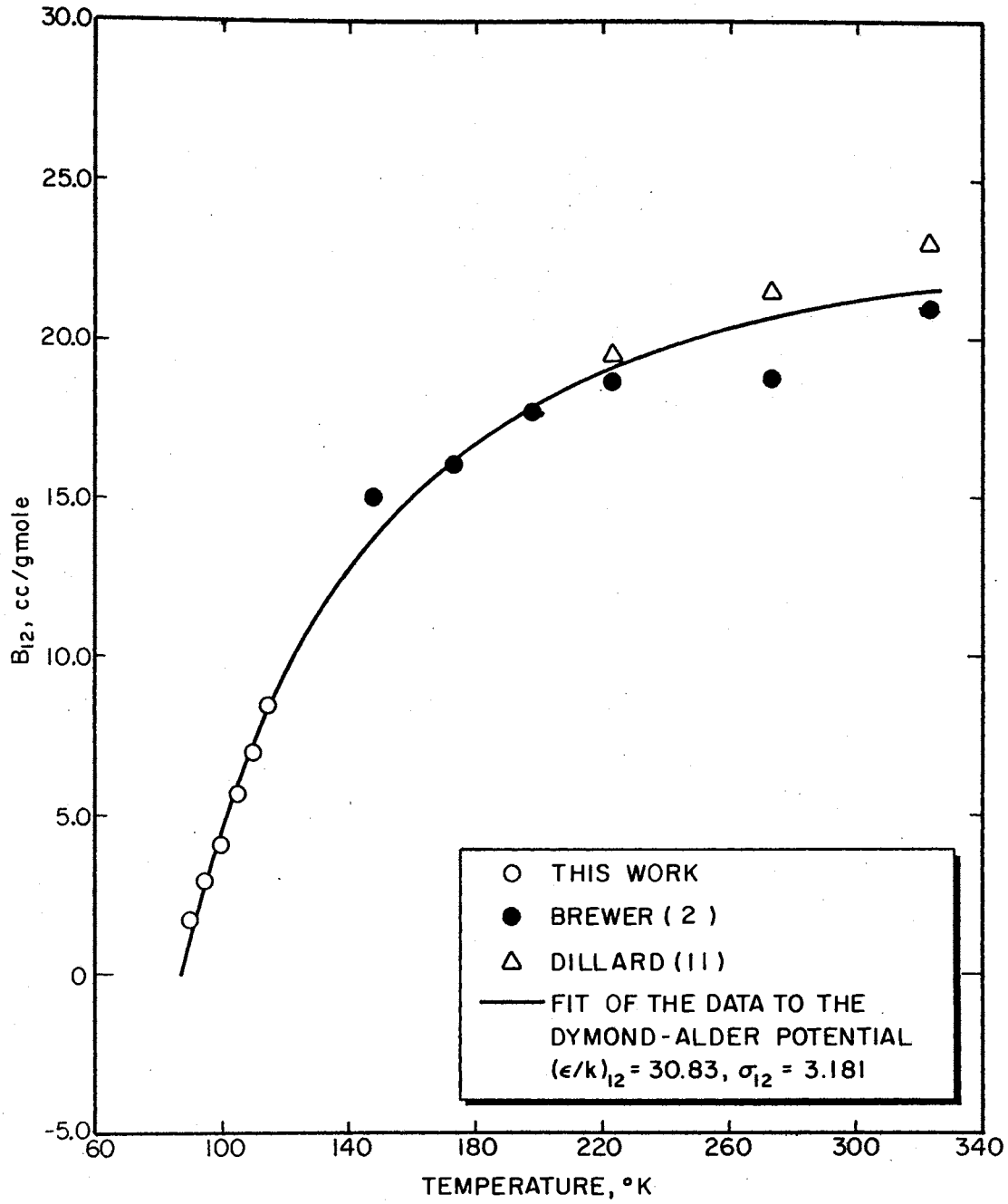

Figure 22. Comparison of the Interaction Second Virial Coefficients B_{12}, Obtained in This Work with the Values of Other Investigators for the Helium-Krypton System

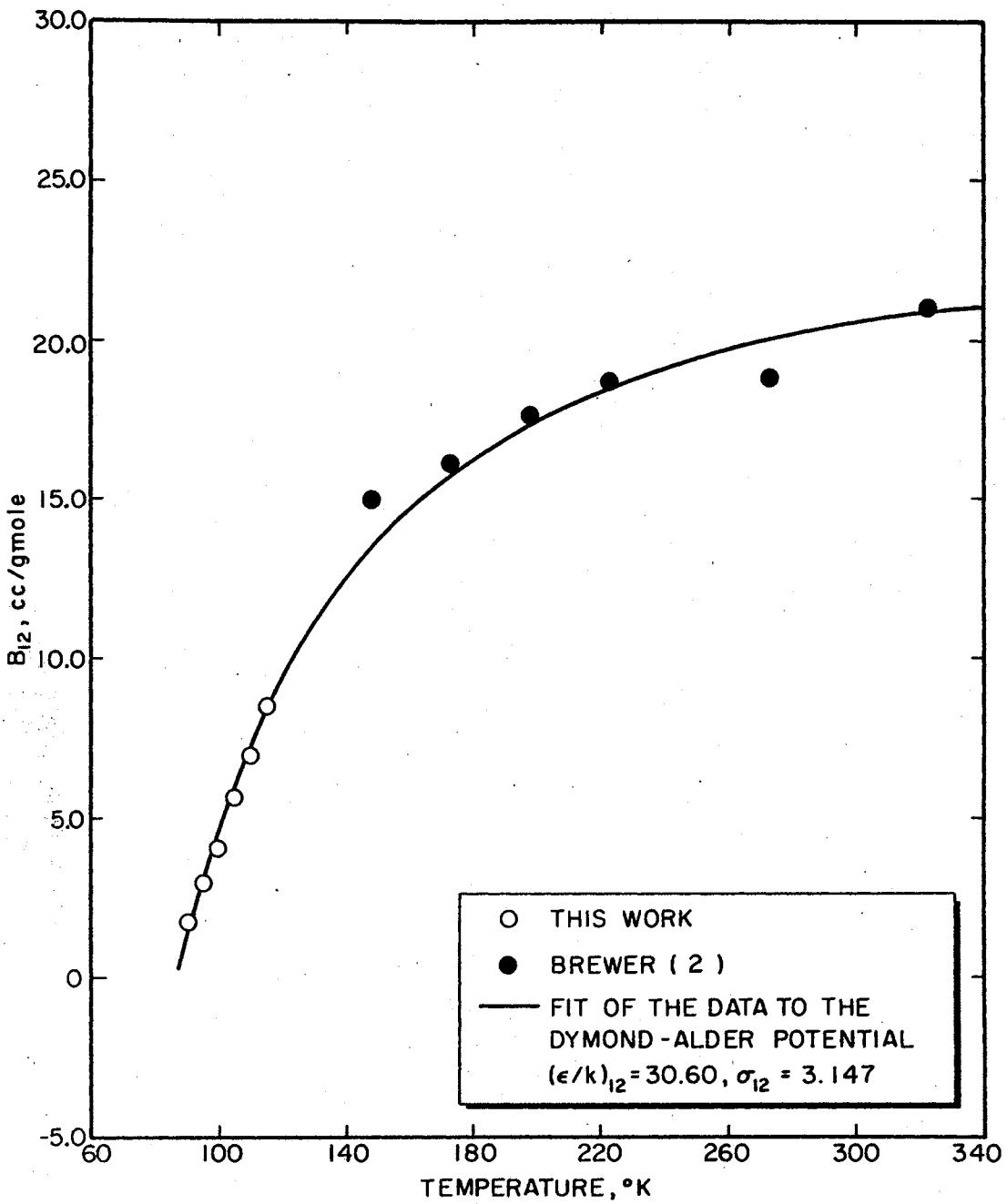

Figure 23. Comparison of the Interaction Second Virial Coefficients, B_{12}, Obtained in This Work with the Values of Brewer for the Helium-Krypton System

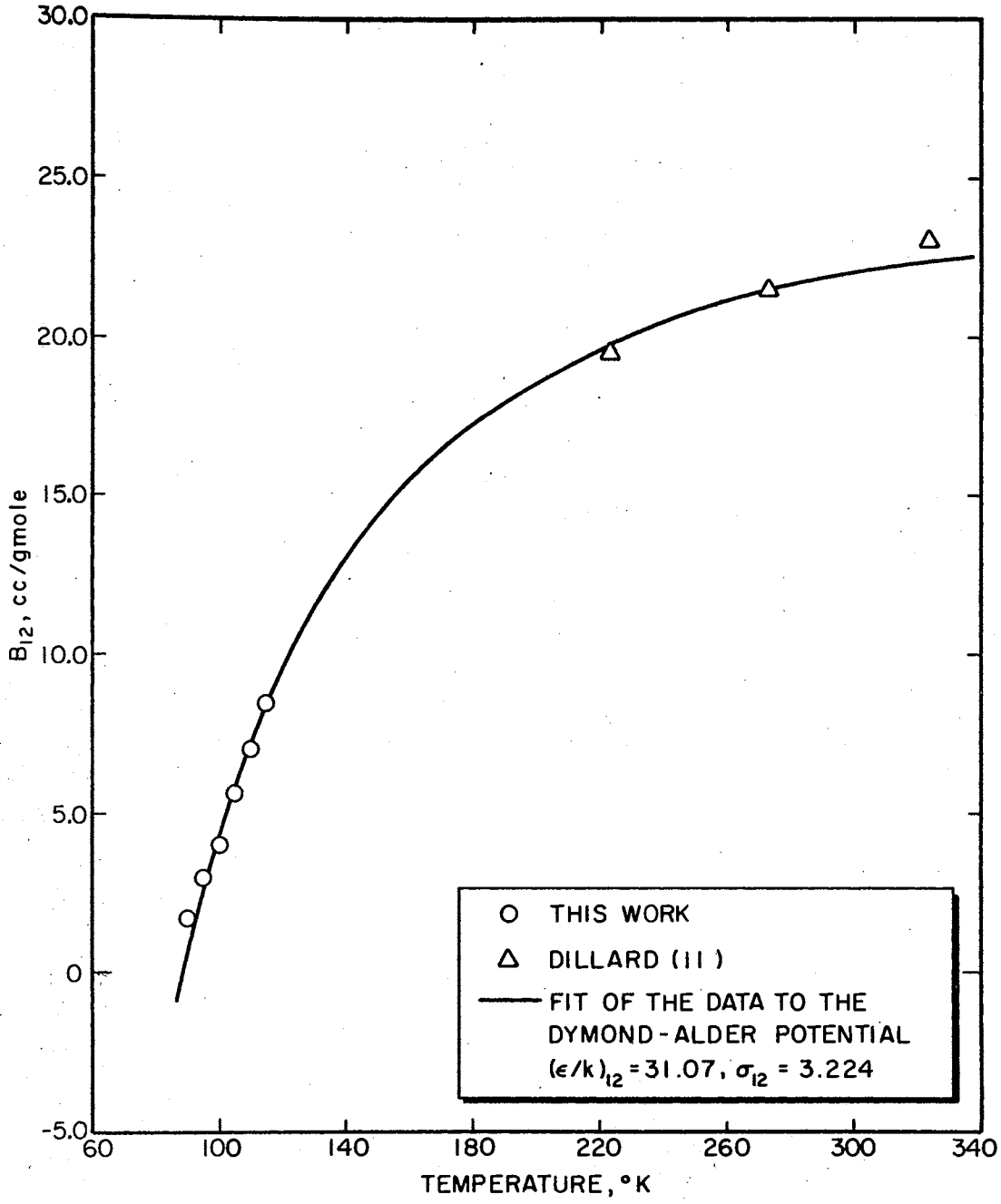

Figure 24. Comparison of the Interaction Second Virial Coefficients, B_{12}, Obtained in This Work with the Values of Dillard for the Helium-Krypton System

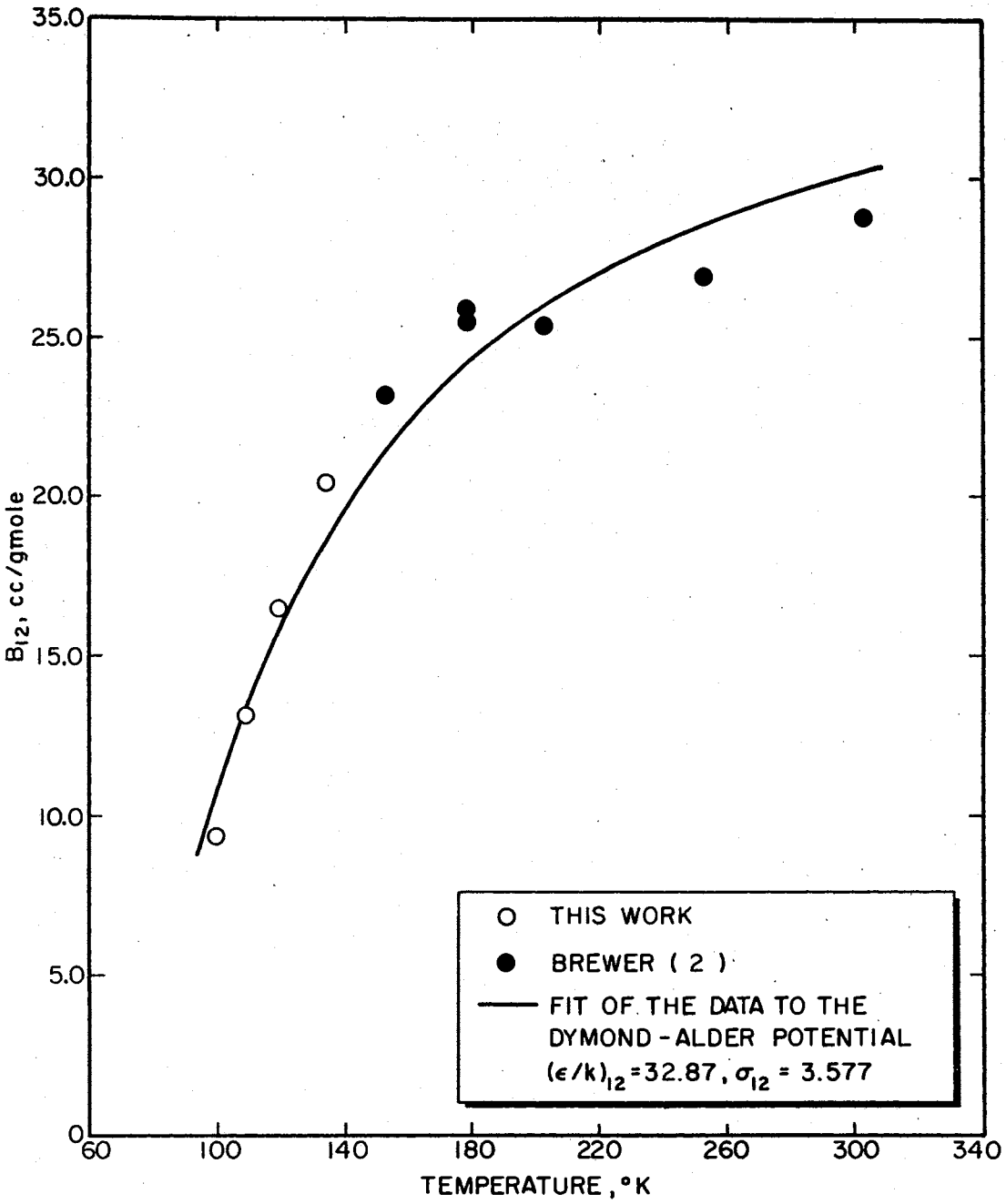

Figure 25. Comparison of the Interaction Second Virial Coefficients, B_{12}, Obtained in This Work with the Values of Brewer for the Helium-Xenon System

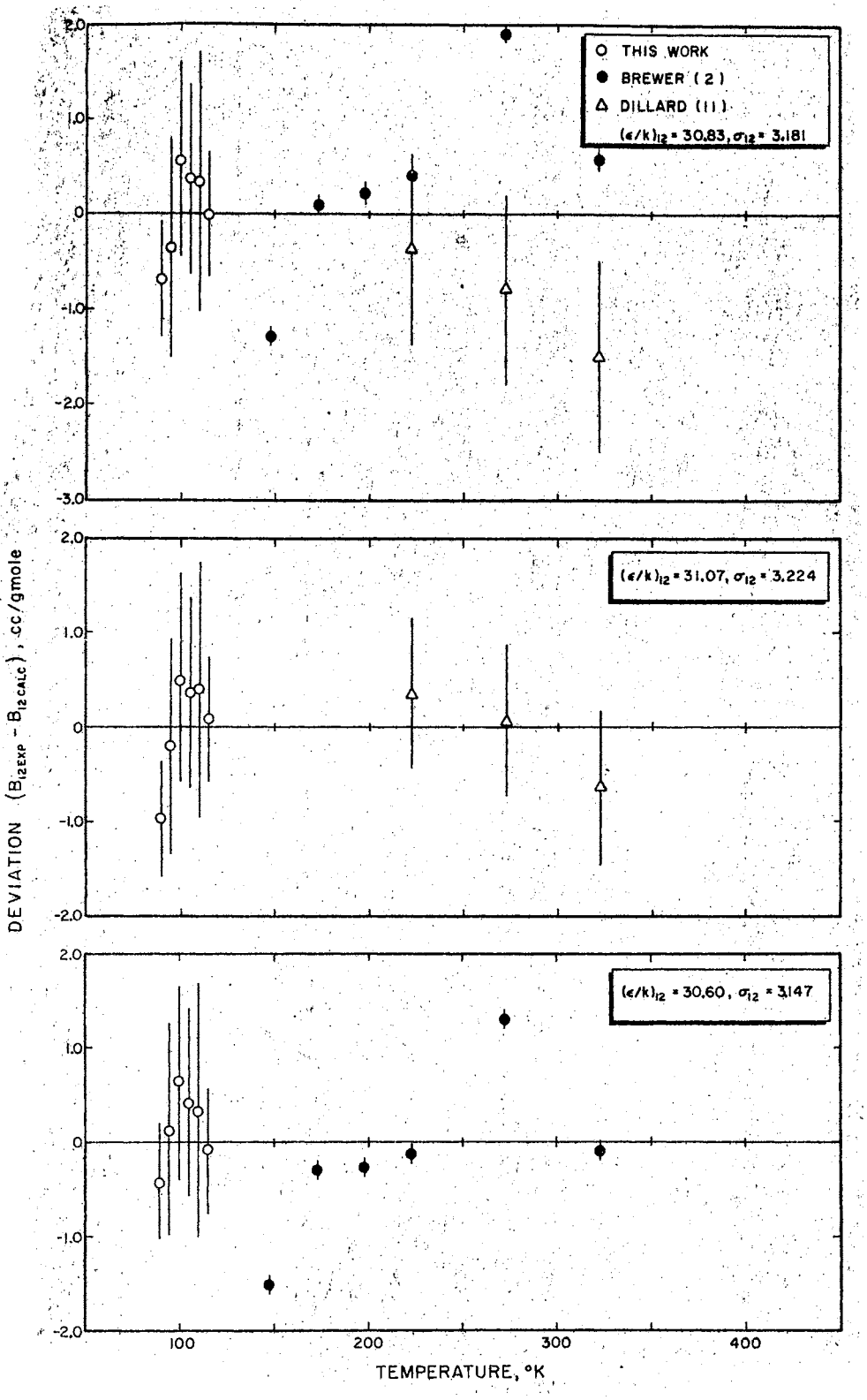

Figure 26. Comparison of Experimental Interaction Second Virial Coefficients for the Helium-Krypton System with Values Calculated from the Dymond-Alder Potential

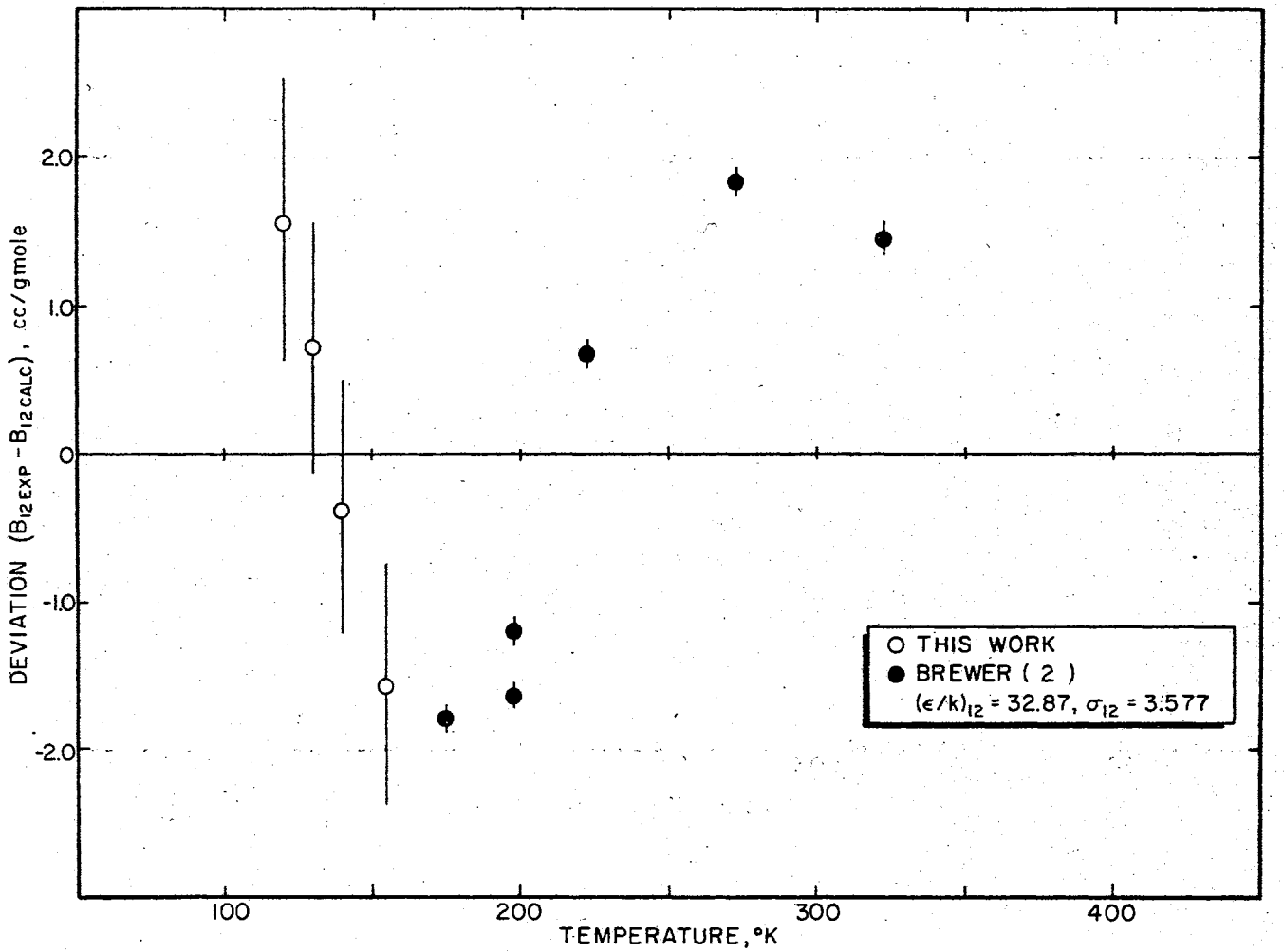

Figure 27. Comparison of Experimental Interaction Second Virial Coefficients for the Helium-Xenon System with Values Calculated from the Dymond-Alder Potential

of B_{12} and the values predicted by the Dymond-Alder potential are plotted as a function of temperature (error bands are also included).

In Figure 26, using the above technique, the B_{12} values of this study for the helium-krypton system are compared simultaneously with the data of Brewer (2) and Dillard (11). In the same figure, the data of this work are also compared individually to the Brewer data and to the Dillard data. When the data of Brewer and the data of Dillard were individually fit with the data of this work to the Dymond-Alder potential, Figure 26 indicates that the agreement for both cases was good (nominal scatter of ±1 cc/g-mole). However, the results of the simultaneous fit of all the data to the Dymond-Alder potential revealed that the data of Brewer and Dillard failed to agree with each other as well as they individually agreed with the data of this work.

Examination of Figure 27 reveals that the B_{12} values for the helium-xenon system of this study and of Brewer are not in as good of agreement as the B_{12} values of the helium-krypton data. The agreement for the helium-xenon system is ±2 cc/g-mole. The apparent systematic deviation from the Dymond-Alder potential exhibited by this system could result from the failure of the potential to adequately fit the data, but this is unlikely because of its ability to fit the data of other rare gas systems. Brewer claims a precision in his measurements of the excess virial coefficient [Equation (1)] of ±0.1 cc/g-mole, but examination of Figures 23 or 26 for the helium-krypton system and Figure 25 or 27 for the helium-xenon system indicates that the nominal scatter in his data for either system is significantly larger than ±0.1 cc/g-mole. This does not imply that Brewer's data are not of excellent quality, but merely that some of his data points have a higher uncertainty than

±0.1 cc/g-mole.

An attempt was made to resolve the question of this possible (marginal) inconsistency of the present data and that of Brewer on the helium-xenon system. A method was devised to test the consistency of the virial coefficient data on the present systems through the use of recent data on gas phase diffusivities in the same systems. The test would rest only on the assumption of the applicability of two-parameter corresponding states theory.

The method of superposition of logrithmic plots (39) was used, independent of any empirical potential model, to determine potential parameter ratios from the diffusion coefficient data for the helium-krypton and helium-xenon systems. The potential parameter ratios from the gas diffusion data were then used to superimpose the virial coefficient data for the helium-xenon system on the data for the helium-krypton system with the hope that such superposition would reveal whether the values of this work or those of Brewer superimposed more readily. In this manner, any inconsistency in the virial coefficient data of this work or that of Brewer for the two systems of interest would be revealed.

The virial coefficient is classically related to the reduced virial coefficient (19) by

$$B(T) = \frac{2}{3}\pi\tilde{N}\sigma^3 B^*(T^*) \qquad (45)$$

where

$\tilde{N}$ = Avogadro's number

B^* = reduced virial coefficient

T^* = reduced temperature, $T/(\varepsilon/k)$

Taking the logrithem of Equation (45) yields

$$\log B(T) = \log \left(\frac{2}{3}\pi\tilde{N}\right) + \log \sigma^3 + \log B^*(T^*) \qquad (46)$$

In order to compare the interaction virial coefficient data of two different systems, the following equations are examined.

$$\log B_{12}(T) = \log \left(\frac{2}{3}\pi\tilde{N}\right) + \log \sigma_{12}^3 + \log B^*(T^*_{12})$$

$$\log B_{13}(T) = \log \left(\frac{2}{3}\pi\tilde{N}\right) + \log \sigma_{13}^3 + \log B^*(T^*_{13})$$

where

"12" indicates helium-krypton binary

"13" indicates helium-xenon binary.

If the B versus temperature plots are to be superimposed on one another, the reduced temperatures for both systems must be equal. The corresponding shift in the temperature axis is given by $\log T_{13} - \log T_{12}$. But because $T^*_{13} = T^*_{12}$, then

$$\log (T_{13}/T_{12}) = \log T_{13} - \log T_{12}$$

$$= \log T_{13} - \log T^*_{13} - \log T_{12} + \log T^*_{12}$$

$$= \log (T_{13}/T^*_{13}) - \log (T_{12}/T^*_{12})$$

$$= \log (\varepsilon/k)_{13} - \log (\varepsilon/k)_{12} = \log[(\varepsilon/k)_{13}/(\varepsilon/k)_{12}]$$

Thus, when the temperature axes are shifted so that the B versus T curves are superimposed on a log-log plot, the ratio of the temperatures, T_{13}/T_{12}, corresponds to the ratio of the potential parameters, $(\varepsilon/k)_{13}/(\varepsilon/k)_{12}$. Similarly, when the B axes are shifted so that B versus T curves are superimposed on a log-log plot,

$$\log (B_{13}/B_{12}) = \log B_{13} - \log B_{12}$$

$$= \log \sigma_{13}^3 - \log \sigma_{12}^3 = \log (\sigma_{13}^3/\sigma_{12}^3)$$

and the ratio, B_{13}/B_{12}, gives the ratio of the potential parameters, $\sigma_{13}^3/\sigma_{12}^3$.

According to the Chapman-Enskog theory (6, 19), the gaseous state binary diffusion coefficient is given to the first approximation by

$$\rho D_{12} = \left(\frac{3}{8\sqrt{\pi}}\right) \frac{(kT/2\mu_{12})^{1/2}}{\sigma_{12}^2 \Omega_{12}^{(1,1)*}(T_{12}^*)} \tag{47}$$

where

D_{12} = binary diffusion coefficient (cm^2/sec)

ρ = molar density ($g\text{-}mole/cm^3$)

k = Boltzmann's constant ($erg/^oK$)

μ = reduced mass ($gm/g\text{-}mole$)

T = temperature (^oK)

σ_{12} = distance parameter (Å)

$\Omega_{12}^{(1,1)*}(T_{12}^*)$ = reduced collision integral

T^* = reduced temperature, $T/(\varepsilon/k)$

If we assume that the ideal gas law applies, then $\rho = P/RT$. Substituting the ideal gas law into Equation (47) and rearranging yields

$$\sigma_{12}^2 \Omega_{12}^{(1,1)*}(T_{12}^*) = 0.0018583(T^3/\mu_{12})^{1/2}/D_{12}P \tag{48}$$

If the curves of $0.0018583(T^3/\mu_{12})^{1/2}/D_{12}P$ versus temperature for the two systems are superimposed on one another on a log-log plot, an analysis similar to the one for the virial coefficient data shows that the ratio of the shift in the temperature axes, T_{13}/T_{12}, yields the parameter ratio, $(\varepsilon/k)_{13}/(\varepsilon/k)_{12}$, and the ratio of the shift in the diffusion

function axes yields the parameter ratio, $\sigma_{13}^2/\sigma_{12}^2$.

When using the superposition of logrithmic plots technique to determine parameter ratios independent of a potential function from virial coefficient or binary diffusion coefficient data, theory (19) tells us that the classical values of the virial and diffusion coefficients should be used. To obtain these classical values from experimental data, quantum corrections must be subtracted from the experimental data. For example, for virial coefficient data,

$$B_{CL}(T) = [B_{exp}(T) - (h^2/m)B_I(T) - (h^2/m)^2 B_{II}(T) - . \ . \ .] \pm (h^2/m)^{\frac{3}{2}} B_0 \quad (49)$$

where

$B_{exp}(T)$ = experimental virial coefficient

$B_{CL}(T)$ = classicial virial coefficient

$B_I(T)$, $B_{II}(T)$, B_o = quantum corrections,

or in terms of the reduced virial coefficient,

$$B^*_{CL}(T^*) = \tfrac{2}{3}\pi\tilde{N}\sigma^3[B^*_{exp}(T^*) - (\Lambda^*)^2 B^*_I(T^*) - (\Lambda^*)^4 B^*_{II}(T^*) - ...] \pm (\Lambda^*)^3 B^*_o \quad (50)$$

where

$$\Lambda^* = h/[\sigma(\mu\varepsilon)^{\frac{1}{2}}]$$

Quantum corrections for the virial coefficient data were approximated by corrections to the Dymond-Alder potential as evaluated by Lin and Robinson (35).

Iman-Rahajoe, et al (27) have demonstrated that the quantum corrections to the collision integral, $\Omega^{(1,1)*}(T^*)$, are significantly less than one percent for reduced temperatures greater than 5.0 and a value of $\Lambda^* = 1$. Since the values of Λ^* for the helium-krypton and helium-xenon systems are 1.07 and 0.94, respectively, and because the binary

diffusion coefficient measurements cover an approximate reduced temperature range of 5 to 36, quantum corrections to the diffusion data were negligible and were ignored.

Binary diffusion coefficients for the systems of interest over a wide temperature range have been measured by Hogervorst (24) and Van Heijningen, et al (59). The estimated uncertainty in these measurements is ±0.5 to ±1%. The virial coefficient data are assumed to have an uncertainty of ±1 cc/g-mole.

The binary diffusion coefficient and virial coefficient data for both the helium-krypton and helium-xenon systems were plotted on log-log coordinates. The error bands associated with each data point were also plotted for both the diffusion and the virial coefficient data. Because the gas diffusion coefficient data were rather insensitive to the values of the parameter ratios, no unique set of potential parameter ratios were obtained from the diffusion data. Thus, several sets of potential parameter ratios were obtained from the diffusion data by shifting the two curves to several different values of $(\varepsilon/k)_{13}/(\varepsilon/k)_{12}$ and determining the upper and lower limits of $(\sigma_{13}/\sigma_{12})^3$. The uncertainty in $(\sigma_{13}/\sigma_{12})^3$ at each value of $(\varepsilon/k)_{13}/(\varepsilon/k)_{12}$ arises from the uncertainty in the experimental data. Using a similar procedure, values of potential parameter ratios are obtained from the virial coefficient data. The potential parameter ratios from both diffusion data and virial data are plotted with their associated error in Figure 28.

Figure 28 indicates only a small region of overlap for the potential parameter ratios obtained from the diffusion and virial data. This region can be approximated by potential parameter ratios of $(\varepsilon/k)_{13}/(\varepsilon/k)_{12} \simeq 1.01$ and $(\sigma_{13}/\sigma_{12})^3 \simeq 1.32$. The values of the

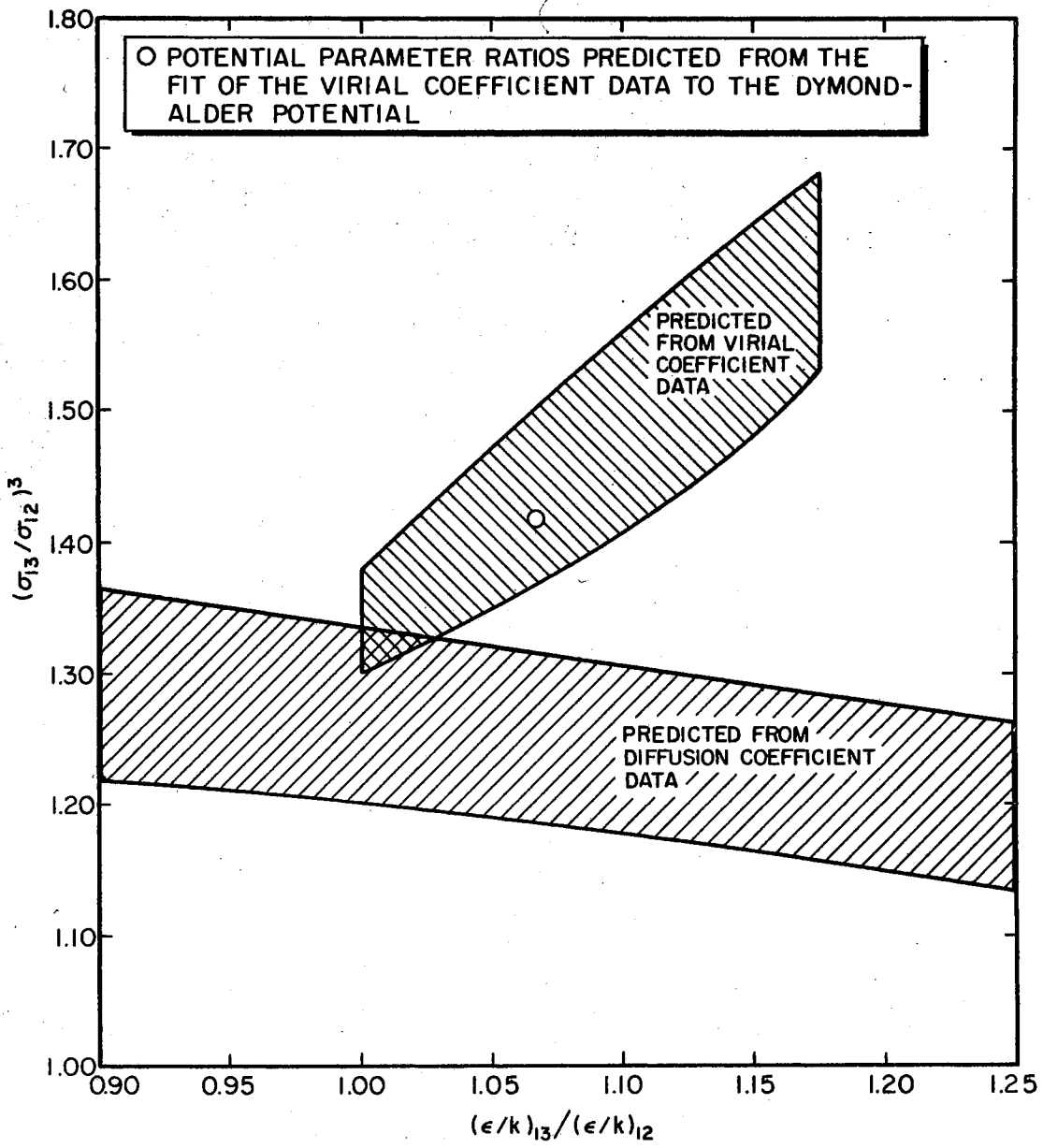

Figure 28. Comparison of Potential Parameter Ratios Obtained from Binary Diffusion Coefficient and Virial Coefficient Data

potential parameter ratios predicted from the fit of the virial coefficient data to the Dymond-Alder potential are $(\varepsilon/k)_{13}/(\varepsilon/k)_{12} = 1.067$ and $(\sigma_{13}/\sigma_{12})^3 = 1.418$.

The results of the superposition of the helium-xenon virial coefficient data onto the helium-xenon virial coefficient data for both of the above-mentioned sets of potential parameter ratios are shown in Figures 29 and 30. The virial coefficients are plotted with their associated error bands. Figure 30 demonstrates that the superposition of virial coefficient data was not greatly altered by the use of the potential parameter ratios consistent with the binary diffusion coefficient data. Thus, within the combined accuracy of the data, the diffusion data revealed no significant inconsistency in the B_{12} data for the helium-xenon system.

The original purpose of the above test was to use a set of potential parameter ratios obtained from binary diffusion coefficient data for the systems of this study to determine whether the virial coefficient data of this work or that of Brewer could be superimposed more readily on one another. In this respect, the test provided no information due to the insensitivity of the diffusion data to the choice of potential parameter ratios. No attempt was made to determine potential parameter ratios independent of empirical potential forms from other types of transport properties (thermal conductivity, viscosity, or thermal diffusivity) because the superposition of logrithmic plots can not be conveniently applied to these data.

Recently, Buck (4) has developed a technique for directly inverting molecular crossed beam scattering data without assuming any analytical form of the intermolecular potential. If this technique were applied

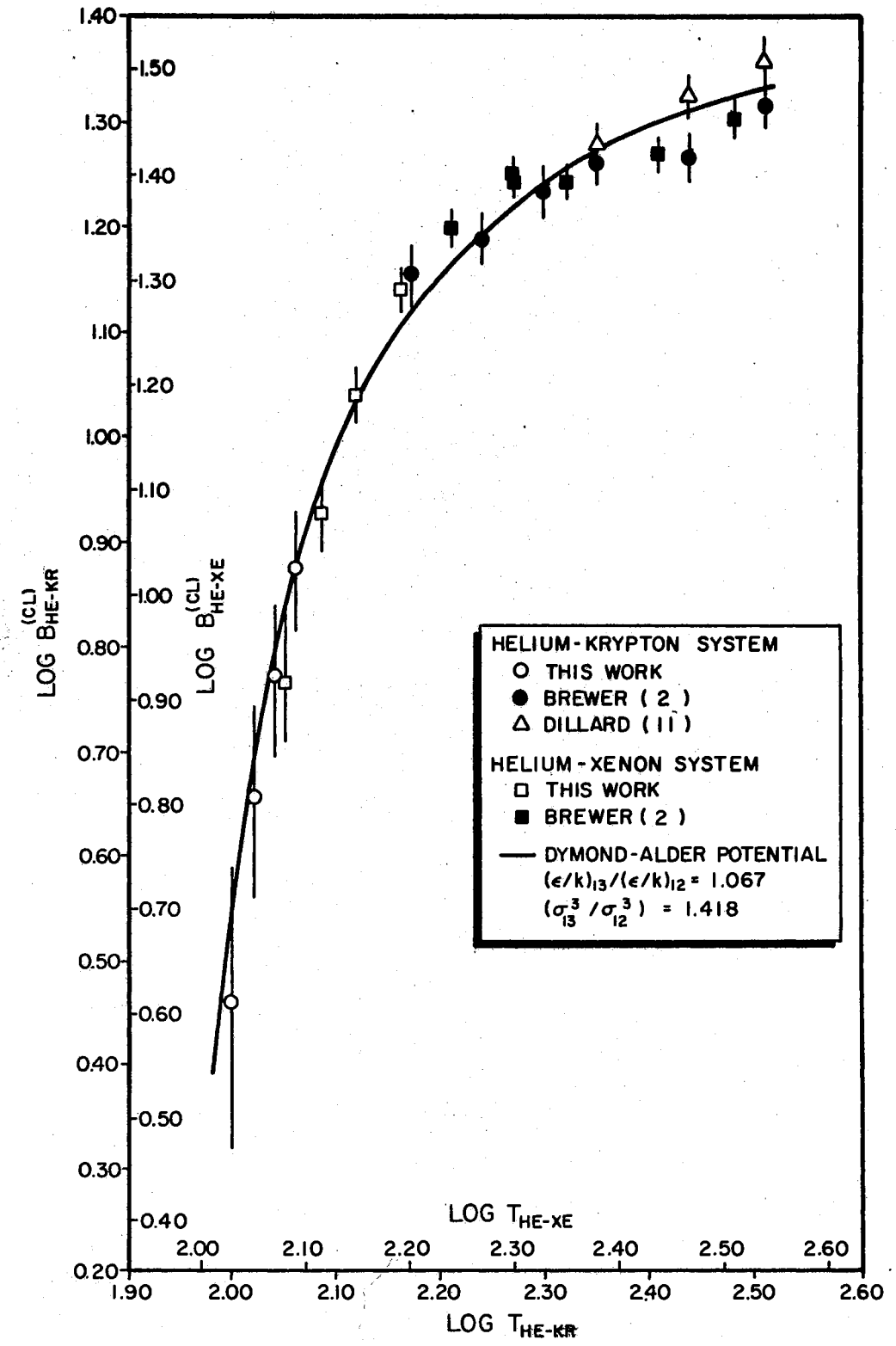

Figure 29. Superposition of the Virial Coefficient Data Using Potential Parameter Ratios Determined from the Dymond-Alder Potential

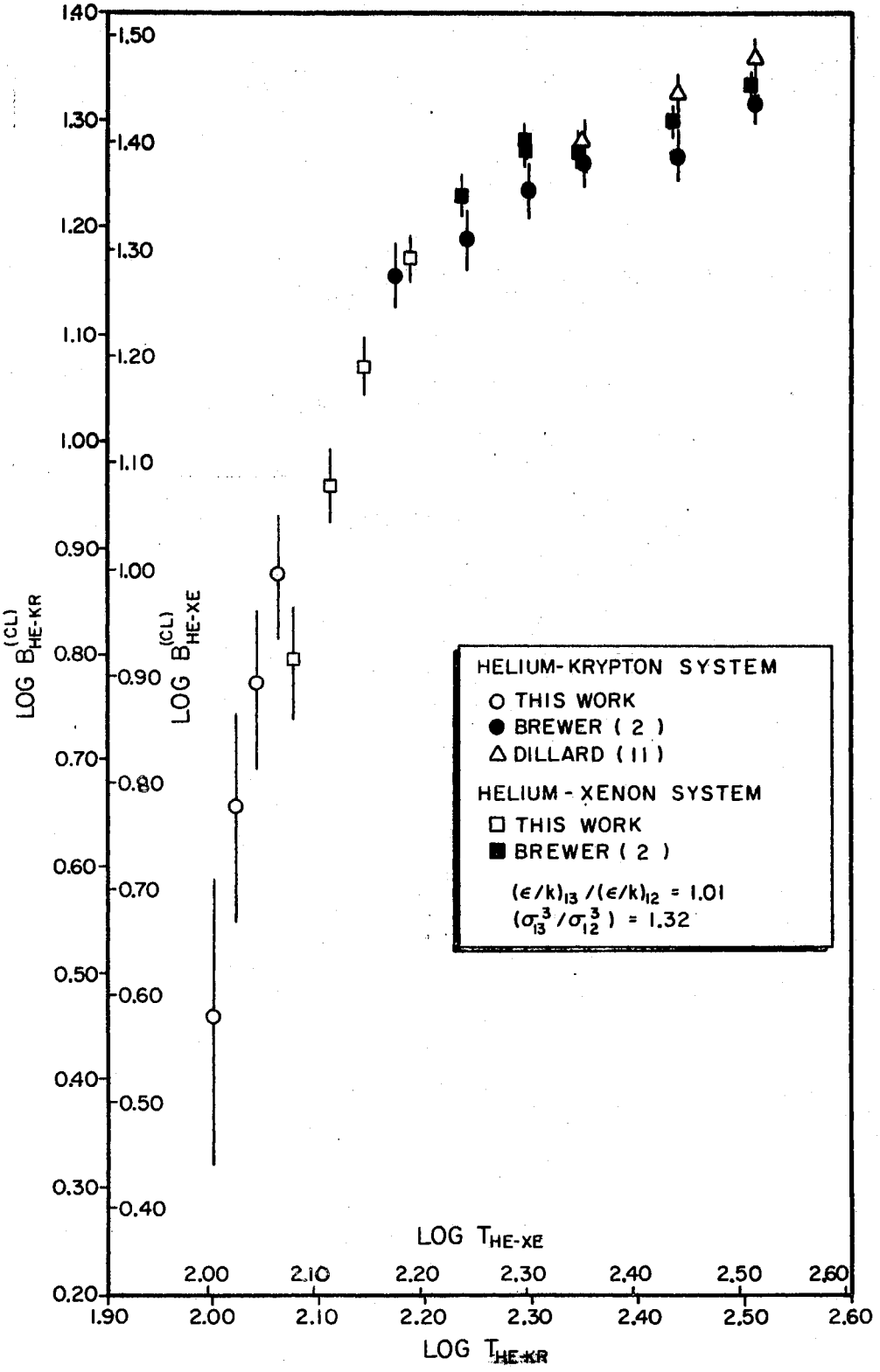

Figure 30. Superposition of the Virial Coefficient Data Using Potential Parameter Ratios Determined Simultaneously from Virial and Diffusion Coefficient Data

to high quality crossed beam data such as that of Lee, et al (47) on rare gas pairs, a valuable source of interaction intermolecular potential parameters could result. If successful, the above technique could provide a more valuable source of interaction potential parameters than do macroscopic properties.

Test of Combination Rules

In this section, the various combining rules presented in Table I for predicting the interaction energy parameter, $(\varepsilon/k)_{12}$, from the pure component parameters were tested using all the available experimental second interaction virial coefficient on the helium-krypton and helium-xenon systems. The two rules for predicting σ_{12} from the pure component parameters by Equations (32) and (33) were also tested. The pure component potential parameters were taken from the work of Lin and Robinson (35) and the values of I, α, and χ were taken from Pitzer (49).

The results of these tests are given in Tables VII and VIII for the helium-krypton and helium-xenon system, respectively. In each table, the values of $(\varepsilon/k)_{12}$ regressed from the experimental B_{12} data are compared to the values calculated from the various combining rules. Also presented are the average deviation, maximum deviation, and root mean square deviation between the experimental value of B_{12} and the value of B_{12} calculated from the Dymond-Alder potential using each of the combination rules.

For the helium-krypton systems, Rules III, VII, and VIII all appeared to give excellent results. Since these three rules were each developed from different theoretical considerations and since each gave similar results, no differentiation between theoretical developments

TABLE VII

TEST OF COMBINING RULES USING VIRIAL COEFFICIENT DATA (B_{12}) FOR THE HELIUM-KRYPTON SYSTEM*

Source of $(\varepsilon/k)_{12}$	$(\varepsilon/k)_{12}$ °K	Deviation** in Predicated $(\varepsilon/k)_{12}$ %	Deviations in B_{12} cc/g-mole		
			Average	Maximum	RMSD***
Direct Regression (k_{12}=0.342)	30.83	---	-0.01	1.90	0.80
Rule I	46.82	51.86	-7.49	-22.50	12.29
Rule II	21.12	-31.49	5.17	10.14	6.23
Rule III	30.57	-0.84	0.15	1.97	0.82
Rule IV	37.83	22.71	-4.32	-9.42	5.13
Rule V	29.40	-4.63	0.82	2.20	1.26
Rule VI	29.26	-5.08	0.90	2.23	1.34
Rule VII	30.43	-1.31	0.23	2.01	0.85
Rule VIII	30.70	-0.42	0.07	1.94	0.81

Source of σ_{12}	σ_{12} Å	Deviation** in Predicated σ_{12} %
Direct Regression	3.181	---
$(\sigma_1+\sigma_2)/2$	2.999	-5.72
$(\sigma_1\sigma_2)^{\frac{1}{2}}$	2.963	-6.85

*Using the value of σ_{12} regressed from the experimental data.

**Deviation = $\frac{\text{calc} - \text{exp}}{\text{exp}} \times 100$

***Root mean square deviation

TABLE VIII

TEST OF COMBINING RULES USING VIRIAL COEFFICIENT DATA (B_{12}) FOR THE HELIUM-XENON SYSTEM*

Source of (ε/k)	(ε/k) ^{o}K	Deviation** in Predicated (ε/k) %	Deviations in B_{12} cc/g-mole		
			Average	Maximum	RMSD***
Direct Regression (k =0.392)	32.87	---	-0.03	1.83	1.37
Rule I	54.07	64.50	-16.29	-25.71	17.67
Rule II	21.41	-34.87	6.87	13.68	7.63
Rule III	24.27	-26.16	5.30	11.00	5.93
Rule IV	36.23	10.21	-2.83	-4.29	2.97
Rule V	22.84	-30.53	6.10	12.31	6.79
Rule VI	23.52	-28.45	5.72	11.71	6.39
Rule VII	24.14	-26.55	5.37	11.15	6.01
Rule VIII	25.91	-21.18	4.36	9.27	4.93

Source of σ_{12}	σ_{12} $\mathring{A}$	Deviation** in Predicated σ_{12} %
Direct Regression	3.577	---
$(\sigma_1 + \sigma_2)/2$	3.196	-10.63
$(\sigma_1\sigma_2)^{\frac{1}{2}}$	3.131	-12.45

*Using the value of σ_{12} regressed from the experimental data

**Deviation $= \frac{\text{calc} - \text{exp}}{\text{exp}} \times 100$

***Root Mean Square Deviation

could be made for this particular system. For the helium-xenon system, no rule predicated the B_{12} data within its experimental accuracy, but Rules IV and VIII gave the best results.

Lin and Robinson (35) have tested various combining rules (Rules I-VI) on the available second interaction virial coefficient data of all ten binaries of the rare gases helium through xenon (excluding data of the present study). They found that Rules II and VI (similar theoretical development) gave the best results for the helium-krypton system and that Rule IV gave the best results for the helium-xenon system although (as in this work) the results for the helium-xenon system were not as satisfactory as those for the helium-krypton system.

In conclusion, the testing of the various combining rules for determining values of $(\varepsilon/k)_{12}$ failed to indicate any rule which gave uniformly good results in predicting second interaction virial coefficients for both the systems studied. These results are in agreement with the conclusions of Lin and Robinson (35) on the rare gas binaries of helium. Likewise, neither the hard-sphere model [Equation (32)] nor the geometric mean rule [Equation (33)] gave satisfactory results in the prediction of the interaction distance parameter, σ_{12}. However, the recent suggestion of Good and Hope (15) appears worse than the hard sphere model.

The interaction constant of the attractive potential term has been well studied within the limits of the London theory, the Kirkwood-Muller theory, etc.; i.e., for symmetrical systems of spherical molecules containing a small number of electrons (49). However, the combining rules derived from these considerations often fail to apply even to systems which approximately obey the above assumptions. This indicates that

consideration of the attractive potential term only does not provide a completely adequate means of developing mixing rules. A more extensive study of the repulsive potential term would seem desirable.

Finally, the values of k_{12} determined in this work from Equation (30) were compared with the correlation of Hiza and Duncan (22), Equation (31), and values of k_{12} obtained by other experimental methods as tabulated in a recent paper by Hiza (21). For the helium-krypton system, a value of k_{12} of 0.342 was obtained in this work as compared to values of k_{12} of 0.359, 0.350, and 0.312, which were obtained, respectively, from beam scattering data, diffusion data, and Equation (31). For the helium-xenon system a value of k_{12} of 0.392 was obtained in this study as compared to values of 0.406 and 0.422 which were obtained, respectively, from beam scattering data and Equation (31).

CHAPTER VIII

CONCLUSIONS AND RECOMMENDATIONS

In this study, an apparatus was constructed which can be used to make both solid-vapor and liquid-vapor equilibrium measurements over a temperature range of 90 to 300° K and a pressure range of 0 to 150 atm. The following conclusions were drawn about the apparatus:

(1) the apparatus and procedures employed successfully combined precision with a relative ease of operation;

(2) the use of an ultrasonic detector to analyze for the trace component in the vapor effluent stream from the equilibrium cell is a composition measuring technique that is at least as good and probably better than any other technique used in studies of this type.

Concerning the experimental apparatus constructed in this work, the following recommendations are offered:

(1) the vacuum transfer line from the cryostat to the high vacuum system should be shortened considerably in an attempt to improve the vacuum inside the cryostat by an order of magnitude (from 10^{-4} torr to 10^{-5} torr);

(2) the ionization vacuum gauge should be mounted closer to the top of the cryostat in order to obtain a more reasonable measurement of the actual vacuum inside the cryostat;

(3) a servicable level indicator for the liquid nitrogen storage vessel should be developed;

(4) the number of differential thermocouples on the cell should be increased so that both temperature gradients on the cell and the temperature difference between the top of the cell and the vapor effluent line could be monitored during experimental operation;

(5) the problem of plugging of the bottom of the cell and the cell inlet vapor line with solid condensate should be carefully studied and a dependable method of heating the inlet vapor line should be developed;

(6) an attempt should be made to apply the ultrasonic detector to composition measurements of binary gas mixtures in which the trace component mole fraction is less than 50 PPM; if the ultrasonic detector can be used in this composition range, lower temperature solid-vapor equilibrium measurements can be made (within the temperature control limitations of the apparatus);

(7) a vapor recirculation pump should be added to the apparatus to decrease condensed phase losses and to provide better liquid mixing when making liquid-vapor equilibrium measurements;

(8) a more elaborate system for metering the amount of the heavier component being condensed into the equilibrium cell should be developed.

As another part of this study, solid-vapor equilibrium measurements were made on the helium-krypton and helium-xenon systems. The following conclusions were reached about the experimental data:

(1) the measurement of the vapor phase composition is the most critical factor influencing the precision of solid-vapor equilibrium measurements;

(2) the composition of the vapor phase was measured with an estimated uncertainty of ±1% in the mole fraction of the trace component; similarly, the enhancement factors (y_2P/P_2^o) of the solid component exhibited a nominal scatter of ±1%.

Concerning the experimental measurements of this type, recommendations for further studies are as follows:

(1) the applicability of this apparatus to liquid-vapor equilibrium measurements should be tested;

(2) solid-vapor and/or liquid-vapor equilibrium measurements should be made on other rare gas pairs which have not been studied previously, namely neon-xenon and argon-xenon;

(3) since solid-vapor equilibrium measurements are limited to systems in which the critical temperature of one component is below the triple point temperature of the other component, further studies of this type could be considered for systems containing such low critical temperature gases as helium, hydrogen, neon, or nitrogen as the lighter component (component "1").

The solid-vapor equilibrium measurements were analyzed using conventional techniques to determine interaction virial coefficients (B_{12} and C_{112}). The values of B_{12} obtained in this manner were compared to the experimental data of other investigators. The following conclusions were reached regarding this part of the study:

(1) the B_{12} data obtained in this study are considered to have a nominal imprecision of ±1 cc/g-mole;

(2) the B_{12} data for the helium-krypton system showed excellent agreement with the data of Dillard and Brewer (nominal scatter of less than ±1 cc/g-mole); the B_{12} data for the helium-xenon system is in reasonable agreement with the data of Brewer (nominal scatter of ±2 cc/g-mole);

(3) binary diffusion coefficient data were used to test (independent of any specific intermolecular potential model) their mutual consistency with the B_{12} data; within the combined accuracies of the virial and diffusion coefficient data, the data appear to be consistent.

Finally the various combining rules presented in Table I for predicting interaction potential parameters from the pure component parameters were tested using the available second interaction virial coefficient data on the two systems studied in this work. No single rule proved uniformly successful in predicting B_{12} data for both systems although several rules gave reasonable results for the helium-krypton system.

Although the interaction constant of the attractive potential term has been extensively studied, no such claim can be made for the interaction constant of the repulsive potential term. Before combining rules for interaction potential parameters can be developed which are uniformly applicable to all simple systems, a closer study of unlike-molecule repulsive forces would seem desirable.

In summary, the apparatus and procedures developed in this study provide an excellent means of making solid-vapor equilibrium measure-

ments. Solid-vapor equilibrium measurements yield a source of sufficiently accurate low temperature data to provide valuable input to the low temperature behavior of second interaction virial coefficients. These data are useful if virial coefficient data are to be used to test combining rules for interaction intermolecular potential parameters.

BIBLIOGRAPHY

1. Abrahamson, A. A., Phys. Rev. 130, 693 (1963).

2. Brewer, J., "Determination of Mixed Virial Coefficients", Report No. MRL-2915-C, Air Force Office of Scientific Research, No. 67-2795 (1967).

3. _____, and G. W. Vaughn, J. Chem. Phys. 50, 2960 (1969).

4. Buck, U., J. Chem. Phys. 54, 1923 (1971).

5. Canfield, F. B., T. W. Leland, Jr., and R. Kobayashi, Advances in Cryogenic Engineering, Vol. 8, Plenum Press, New York (1963), p. 146.

6. Chapman, S., and T. G. Cowling, "The Mathematical Theory of Non-Uniform Gases", Cambridge University Press, New York (1952).

7. Chiu, C.-h., and F. B. Canfield, Advances in Cryogenic Engineering, Vol. 12, Plenum Press, New York (1967), p. 741.

8. Clark, A. M., F. Din, J. Robb, A. Michels, T. Wassenaar, and Th. Zwietering, Physica 17, 876 (1951).

9. Cook, G. A., "Argon, Helium, and the Rare Gases, Vol. I", Interscience Publishers, New York (1961)

10. Dalgarno, A., Advances in Chemical Physics, Vol. XII, Interscience Publishers, New York (1967), p. 143.

11. Dillard, D. D., Ph. D. Thesis, Oklahoma State University, Stillwater, Oklahoma (in preparation).

12. Dymond, J. H., and B. J. Alder, J. Chem. Phys. 51, 309 (1969).

13. Ewald, A. H., Trans. Faraday Soc. 51, 347 (1955).

14. Fender, B. E. F., and G. C. Halsey, Jr., J. Chem. Phys. 36, 1881 (1962).

15. Good, R. J., and C. J. Hope, J. Chem. Phys. 53, 540 (1970).

16. Grice, H. W., and D. J. David, J. Chromatog. Sci. 7, 239 (1967).

17. Guggenheim, E. A., and M. L. McGlashan, Proc. Roy. Soc. (London), A206, 448 (1951).

18. Hall, K. R., and F. B. Canfield, Physica 47, 219 (1970).

19. Hirschfelder, J. O., C. F. Curtiss, and R. B. Bird, "Molecular Theory of the Gases and Liquids", John Wiley and Sons, Inc., New York (1954).

20. Hiza, M. J., Nat. Bur. Std., Boulder, Colo., personal communication, 1970.

21. _____, Cryogenics 10, 106 (1970).

22. _____, and A. G. Duncan, A.I.Ch.E. J. 16, 773 (1970).

23. _____, and R. N. Herring, Advances in Cryogenic Engineering, Vol. 8, Plenum Press, New York (1963), p. 158.

24. Hogervorst, W., Physica 51, 59 (1971).

25. Hoover, A. F., F. B. Canfield, R. Kobayashi, and T. W. Leland, Jr., J. Chem. Eng. Data 9, 568 (1964).

26. Hudson, G. H., and J. C. McCoubrey, Trans. Faraday Soc. 56, 761 (1960).

27. Iman-Rahajoe, S., C. F. Curtiss, and R. B. Bernstein, J. Chem. Phys. 42, 530 (1965).

28. Kidnay, A. J., R. C. Miller, and M. J. Hiza, Ind. Eng. Chem. Funda. 10, 459 (1971).

29. Kirk, B. S., and W. T. Ziegler, Advances in Cryogenic Engineering, Vol. 10, Plenum Press, New York (1965), p. 160.

30. Kirkwood, J. G. Physik Z. 33, 57 (1932); Muller, A., Proc. Roy. Soc. (London) A154, 624 (1936).

31. Kramer, H. L., and D. R. Herschbach, J. Chem. Phys. 53, 2792 (1970).

32. Leming, C. W., and G. L. Pollack, Phys. Rev. B 2, 3323 (1970).

33. Lennard-Jones, J. E., Proc. Roy. Soc. (London) A106, 463 (1924).

34. Levelt-Sengers, J. M. H., M. Klein, and J. S. Gallagher, "Pressure-Volume-Temperature Relationships of Gases. Virial Coefficients", unpublished manuscript, Nat. Bur. Std., Washington, D. C., 1969.

35. Lin, H.-M., and R. L. Robinson, Jr., J. Chem. Phys. 54, 52 (1971).

36. London, F., Z. Physik 63, 245 (1930).

37. Maimoni, A., Rev. Sci. Instr. 27, 1024 (1956).

38. Mason, E. A., M. Islam, and S. Weissman, Phys. Fluids 7, 1011 (1964).

39. Mason, E. A., and W. E. Rice, J. Chem. Phys. 22, 522 (1954).

40. McKinley, C., J. Brewer, and E. S. J. Wang, Advances in Cryogenic Engineering, Vol. 7, Plenum Press, New York (1962), p. 114.

41. Miller, R. C., A. J. Kidnay and M. J. Hiza, "The Solid-Vapor and Liquid-Vapor Phase Equilibrium Properties of the Neon-Krypton System", unpublished manuscript, Nat. Bur. Std., Boulder, Colo., 1970.

42. Moelwyn-Hughes, E. A., Physical Chemistry, Pergamon Press, New York (1957).

43. Mullins, J. C., and W. T. Ziegler, Advances in Cryogenic Engineering, Vol. 10, Plenum Press, New York (1965), p. 171.

44. Noble, F. W., ISA J. 8, 54 (1961).

45. _____, K. Abel, and P. W. Cook, Anal. Chem. 36, 1421 (1964).

46. Packard, J. R., and C. A. Swenson, J. Phys. Chem. Solids 24, 1405 (1963).

47. Parson, J. M., T. P. Schafer, P. E. Siska, F. P. Tully, Y. C. Wong, and Y. T. Lee, J. Chem. Phys. 53, 3755 (1970).

48. Phillipson, Phys. Rev. 125, 1981 (1962).

49. Pitzer, K. S., Advances in Chemical Physics, Vol. II, Interscience Publishers, New York (1959), p. 59.

50. Prigogine, I., "The Molecular Theory of Solutions", North-Holland Publishing Co., Amsterdam (1957).

51. Reid, R. C., and T. W. Leland, Jr., A.I.Ch.E. J. 11, 228 (1965).

52. Rowlinson, J. S., and M. J. Richardson, Advances in Chemical Physics, Vol. II, Interscience Publishers, New York (1959), p. 85.

53. Scott, R. B., "Cryogenic Engineering", D. van Nostrand Co., Inc., Princeton, N. J. (1959).

54. Sherwood, A. E., and J. M. Prausnitz, J. Chem. Phys. 41, 413 (1964).

55. Ibid., p. 429.

56. Sikora, P. T., J. Phys. B: Atom. Molec. Physics 3, 1475 (1970).

57. Sonntag, R. E., and G. J. Van Wylen, Advances in Cryogenic Engineering, Vol. 7, Plenum Press, New York (1962), p. 99.

58. Trefny, J. U., and B. Serin, J. Low Temp. Phys. 1, 231 (1969).

59. Van Heijningen, R. J. J., J. P. Harpe, and J. J. M. Beenakker, Physica 38, 1 (1968).

60. White, D., T. Rubin, P. Camky, and H. L. Johnson, J. Phys. Chem. 64, 1607 (1960).

61. Ziegler, W. T., D. W. Yarbrough, and J. C. Mullins, Tech. Rept. No. 1 (Krypton), Project No. A-764, Georgia Inst. of Tech., Contract No. CST-1154, Natl. Std. Ref. Data Program, NBS, Wash., D. C. (1964).

62. _____, J. C. Mullins, and A. R. Berquist, Tech. Rept. No. 3 (Xenon), Project Nos. A-764 and E-115, Georgia Inst. of Tech., Contract No. CST-1154, Natl. Std. Ref. Data Program, NBS, Wash., D. C. (1966).

APPENDIX A

CHECK OF PLATINUM RESISTANCE THERMOMETER AT THE TRIPLE POINT OF WATER

The triple point of a substance is that point at which all three phases, solid, liquid, and vapor coexist in equilibrium. The triple point of water is defined as 0.01° C. In this work, a triple point cell manufactured by Trans-Sonic, Inc. was used to check the platinum resistance thermometer. Two separate tests were made and these tests were performed eight months apart. The results are shown in Tables IX and X. The measurements are in excellent agreement with the National Bureau of Standards calibration.

TABLE IX

MEASUREMENT OF THE TRIPLE POINT OF WATER (10/69)

Resistance Readings

Reading No.	N	R	Average Reading
1	25.5310	25.5360	25.5335
2	25.5295	25.5355	25.5325
3	25.5293	25.5353	25.5323
	(Apparent Equilibrium Occurs)		
4	25.5293	25.5352	25.5322
5	25.5292	25.5352	25.5322
6	25.5292	25.5352	25.5322
7	25.5293	25.5352	25.5322
8	25.5293	25.5351	25.5322
9	25.5292	25.5352	25.5322
10	25.5292	25.5352	25.5322
11	25.5293	25.5351	25.5322
	(Ice Melted)		
	Overall Average = 25.5322		
	NBS Calibration = 25.5321		

TABLE X

MEASUREMENT OF THE TRIPLE POINT OF WATER (6/70)

Resistance Readings

Reading No.	N	R	Average Reading
	(20 minute wait)		
1	25.5365	25.5258	25.5321
2	25.5366	25.5258	25.5322
3	25.5366	25.5258	25.5322
4	25.5365	25.5258	25.5321
5	25.5365	25.5257	25.5321
6	25.5365	25.5258	25.5321
	(Ice Melted)		
	Overall Average = 25.5321		
	NBS Calibration = 25.5321		

APPENDIX B

PRESSURE GAUGE CALIBRATIONS

All three Heise bourdon tube pressure gauges used in this work were calibrated against a Ruska dead weight gauge which has a precision of ±0.01 psia. Each of the gauges were compared with the dead weight gauge at evenly spaced pressure increments over the entire pressure range of the gauge. Measurements were taken for both increasing and decreasing pressure increments as a check for hystersis.

The 3000 psig gauge was calibrated in increments of 100 psi from 0 to 2000 psig, the 1000 psig gauge in increments of 50 psi over the entire range of the gauge, and the 300 psig gauge in increments of 20 psi over the entire range of the gauge. The results of these calibrations are presented in Figures 31 to 33. In these figures, the Ruska pressure reading is considered to be the actual pressure reading. The Heise gauge readings are corrected by adding the appropriate pressure deviation (Ruska gauge-Heise gauge) to the Heise gauge reading.

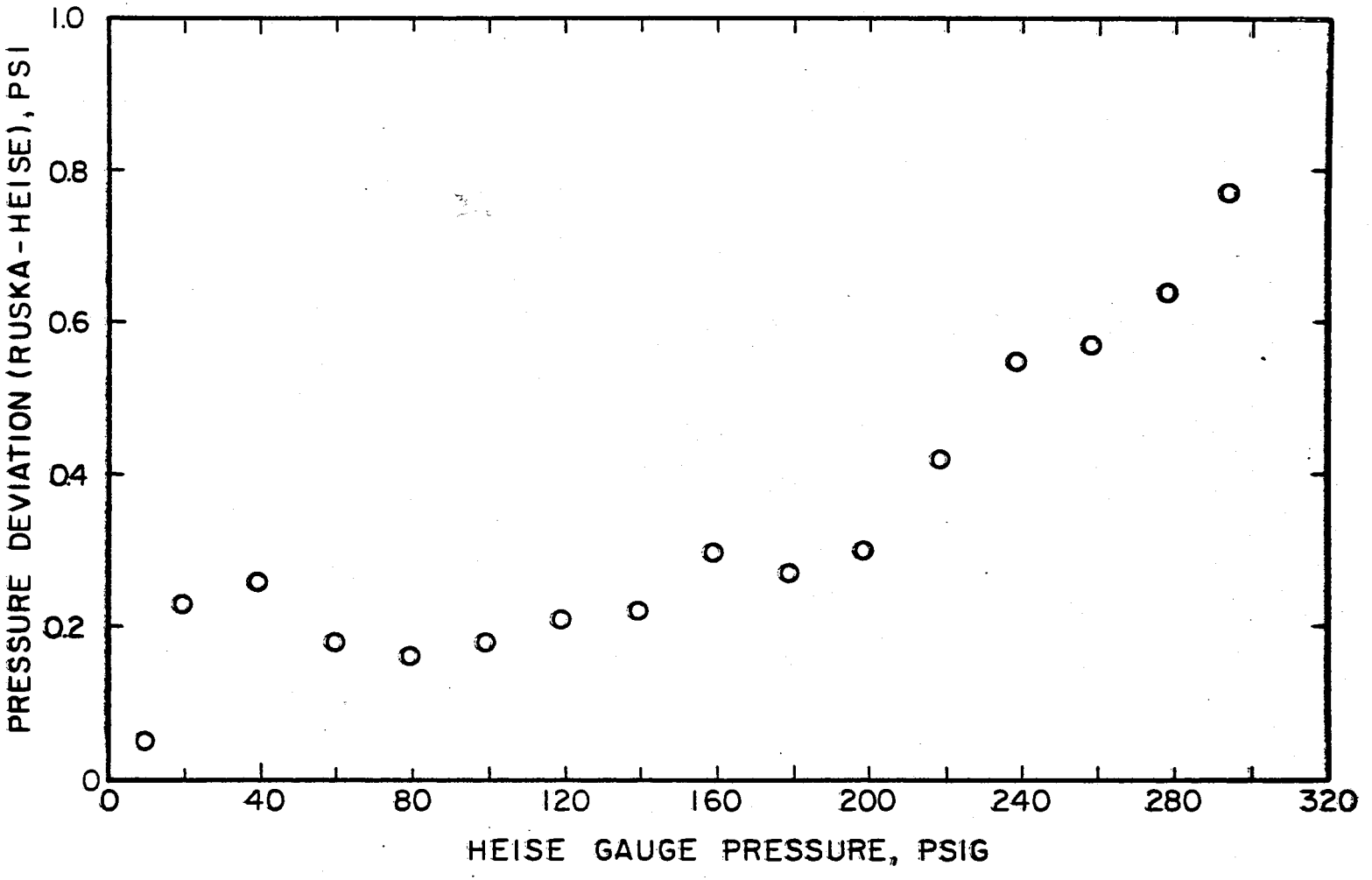

Figure 31. Calibration of the 300 psig Pressure Gauge

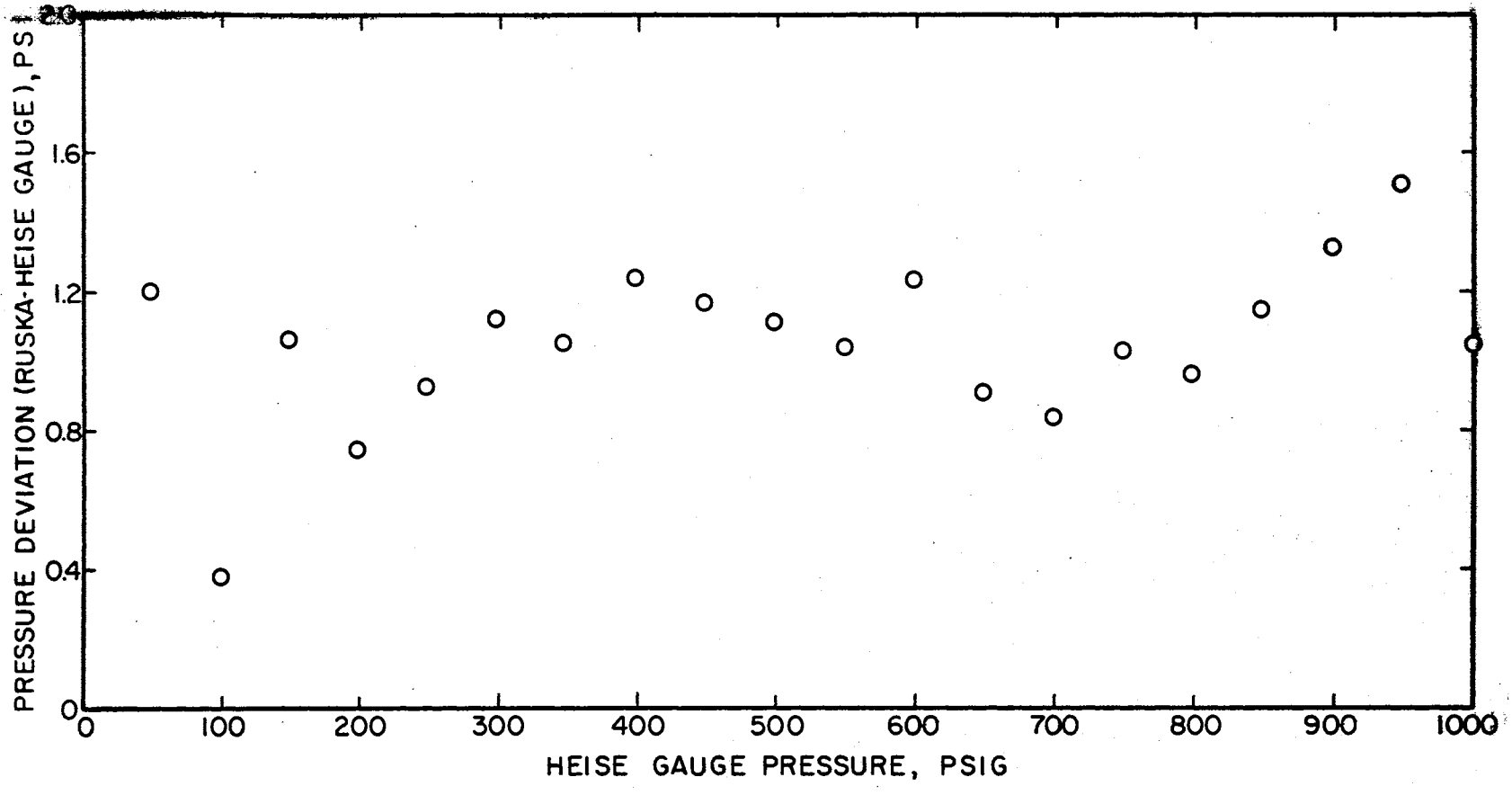

Figure 32. Calibration of the 1000 psig Pressure Gauge

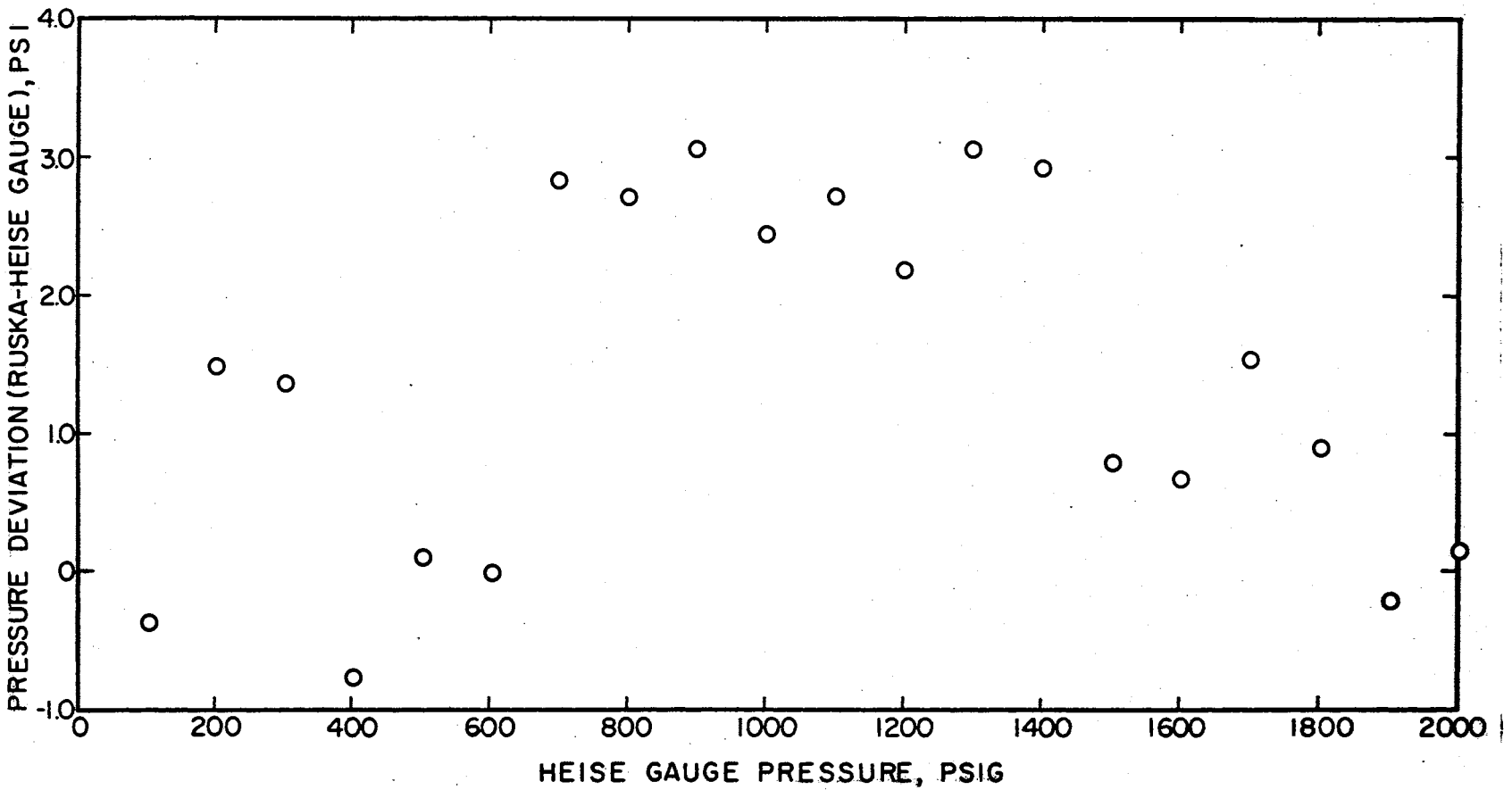

Figure 33. Calibration of the 3000 psig Pressure Gauge

APPENDIX C

ELEMENTARY THEORY OF THE ULTRASONIC DETECTOR

Directly or indirectly measuring the velocity of sound in gas mixtures is a technique that has been utilized for more than 70 years in gas analysis problems. However, Noble (44) was one of the first to apply this technique to gas chromatography. In 1964, Noble, Abel, and Cook (45) presented the theory and instrumentation for an ultrasonic detector as applied to gas chromatography, and discussed the influence of factors affecting the sensitivity of the detector.

The time required for a sound wave of velocity, c, to travel a distance, s, is given by

$$t = s/c$$

The phase delay, Θ, of a sound wave in electrical degrees corresponding to t is

$$\Theta = \frac{360fs}{c} \qquad \text{(C-1)}$$

where f is the frequency of the sound wave.

For pure ideal gases at low frequency

$$c = \left[\frac{\gamma RT}{M} \right]^{\frac{1}{2}} \qquad \text{(C-2)}$$

where

M = molecular weight

γ = ratio of the specific heat at constant pressure to the specific heat at constant volume

R = universal gas constant (8314 m^2/g-mole - ^oK)

T = absolute temperature.

Combining Equations (C-1) and (C-2) yields

$$\Theta = \frac{360sf}{(RT)^{\frac{1}{2}}} (M/\gamma)^{\frac{1}{2}} \qquad \text{(C-3)}$$

For a binary gas mixture in which a sample gas of mole fraction y_2, molecular weight, M_2, and specific heat ratio, γ_2, the equation for the phase delay of a sound wave is

$$\Theta = \frac{360sf}{(RT)^{\frac{1}{2}}} \left(\frac{M_1}{\gamma_1}\right)^{\frac{1}{2}} \left\{1 + \frac{y_2}{2}\left[\left(\frac{M_2}{M_1} - 1\right) + \frac{C_{P2}}{C_{P1}}\left(\frac{\gamma_1}{\gamma_2} - 1\right)\right]\right\} \qquad \text{(C-4)}$$

where C_{P2} and C_{P1} are the specific heats at constant pressure of components "1" and "2", respectively. In Equation (C-4) both gases are assumed to be ideal and the gas mixture is assumed to be homogeneous.

The phase delay change, $\Delta\Theta$, caused by the addition of gas "2" to gas "1" is

$$\Delta\Theta = 180sf\left(M_1/RT\gamma_1\right)^{\frac{1}{2}} y_2\left[\left(\frac{M_2}{M_1} - 1\right) + \frac{C_{P2}}{C_{P1}}\left(\frac{\gamma_1}{\gamma_2} - 1\right)\right] \qquad \text{(C-5)}$$

Equation (C-5) is valid when the specific heats at the frequency of a sound wave are the same as the tabulated values determined by calorimetry. At high frequencies, the tabulated values are generally valid only for monatomic gases. Equation (C-5) indicates that a sample gas ("2")

whose molecular weight is greater than the reference gas ("1") will yield a positive phase delay change.

Several factors influencing the sensitivity of an ultrasonic detector are the temperature, pressure, and carrier gas flow rate. Over a temperature range of 50 to 250° C., Equation (C-5) predicts that the average phase change per degree centigrade temperature change at a sound frequency of 4 megacycles per millimeter of path length is approximately 1.6 electrical degrees for helium. Therefore, when helium is used as a carrier gas, a phase stability of 0.001 electrical degrees requires a temperature stability of roughly 0.0006° C. which is obtainable with suitable lagging and insulation.

The RT/M term in Equation (C-2) is equivalent to P/ρ for an ideal gas where P is the pressure and ρ is the density of the gas. This ratio is a constant for an ideal gas at constant temperature. Thus, the velocity of sound appears to be independent of pressure for the ideal gas case. This is true for monatomic gases except at very high frequencies. For all other gases, the value of γ is a function of pressure or, more exactly, a function of the ratio of frequency to pressure when working near a region of frequency dispersion because the relaxion frequency is proportional to pressure. At a frequency of 4 Mc., a 2.0% decrease in pressure will result in an approximate increase of 0.04% in the velocity of sound in hydrogen at 0° C. This results in a phase change of about 0.5 electrical degree per millimeter of path length.

For a tube of length s with gas flowing through it at some specified velocity v_g parallel to the direction of sound propagation, the time required for a sound wave to travel through the tube will be increased or decreased by s/v_g. The change in phase associated with a

change in v_g will be

$$|\Delta\theta| \simeq \frac{360sf}{c_1^2} |\Delta v_g| \qquad \text{(C-6)}$$

where v_g is the change in the gas flow rate and c_1 is the velocity of sound in the unmoving gas. However, if the length of the tube is short compared with the diameter so that the gas flow can be directed at right angles to the propagation of the sound wave with essentially no holdup of sample in the ends of the tube, then there will be no change in phase associated with a change in carrier flow rate.

Examination of Equation (C-5) shows that the phase change (i.e., detector response) is linear with respect to the trace component mole fraction (y_2) when the assumptions inherent in Equation (C-5) are obeyed. However, Noble, Abel, and Cook (45) have stated that the accuracy of Equation (C-5) and thus, the linearity of phase change with respect to y_2, decreases as the trace component mole fraction increases. They have derived an expression for the maximum allowable mole fraction, y_2, for which Equation (C-5) is applicable.

$$y_2^{max} = \frac{0.3}{(M_2/M_1) - 1} \qquad \text{(C-7)}$$

The results of the calibrations performed in this study on the ultrasonic detector (Appendix D) are in agreement with the above observations. The calibration curves for all the systems considered in the present study are linear below mole fractions (y_2) of 0.002. A slight curvature in the curves appears above this mole fraction and an s-shape occurs in the curves at mole fractions near the values of y_2^{max} as determined by Equation (C-7).

APPENDIX D

CALIBRATION OF THE ULTRASONIC DETECTOR

The ultrasonic detector was calibrated using mixtures of known composition prepared in this laboratory using a volumetric technique. The equipment used to prepare these mixtures is presented in Figure 34. The equipment consists of a constant temperature bath which houses the mixture sample bomb, two pressure gauges, a vacuum pump, and the component gas storage cylinders.

Solute pressures are measured with either a fused quartz precision pressure gauge (Texas Instruments, Inc., Model 141 A) or a 100 psig Heise bourdon tube pressure. The fused quartz gauge contains a fused quartz tube capsule with a pressure range of 0-1000 mm Hg. The precision of the Heise gauge is ±0.1 psi and the precision of the fused quartz gauge is ±0.15 mm Hg. Gas mixture pressures are measured with a 3000 psig Heise bourdon tube gauge whose precision is ±3 psi. The vacuum pump is a Welch Model No. 1402B. The mixture sample bomb is a one-liter aluminum transfer cylinder with a pressure rating of 3000 psia. The constant temperature bath is capable of controlling the temperature of the gas mixture sample bomb to ±0.05° C.

All mixtures are made up at a temperature of 25 ±0.05° C. The mixture bomb is evacuated to 1.0 millitorr and solute gas is injected into the mixture bomb and its pressure measured. After the bomb has reached thermal equilibrium, the transfer lines are evacuated and solute

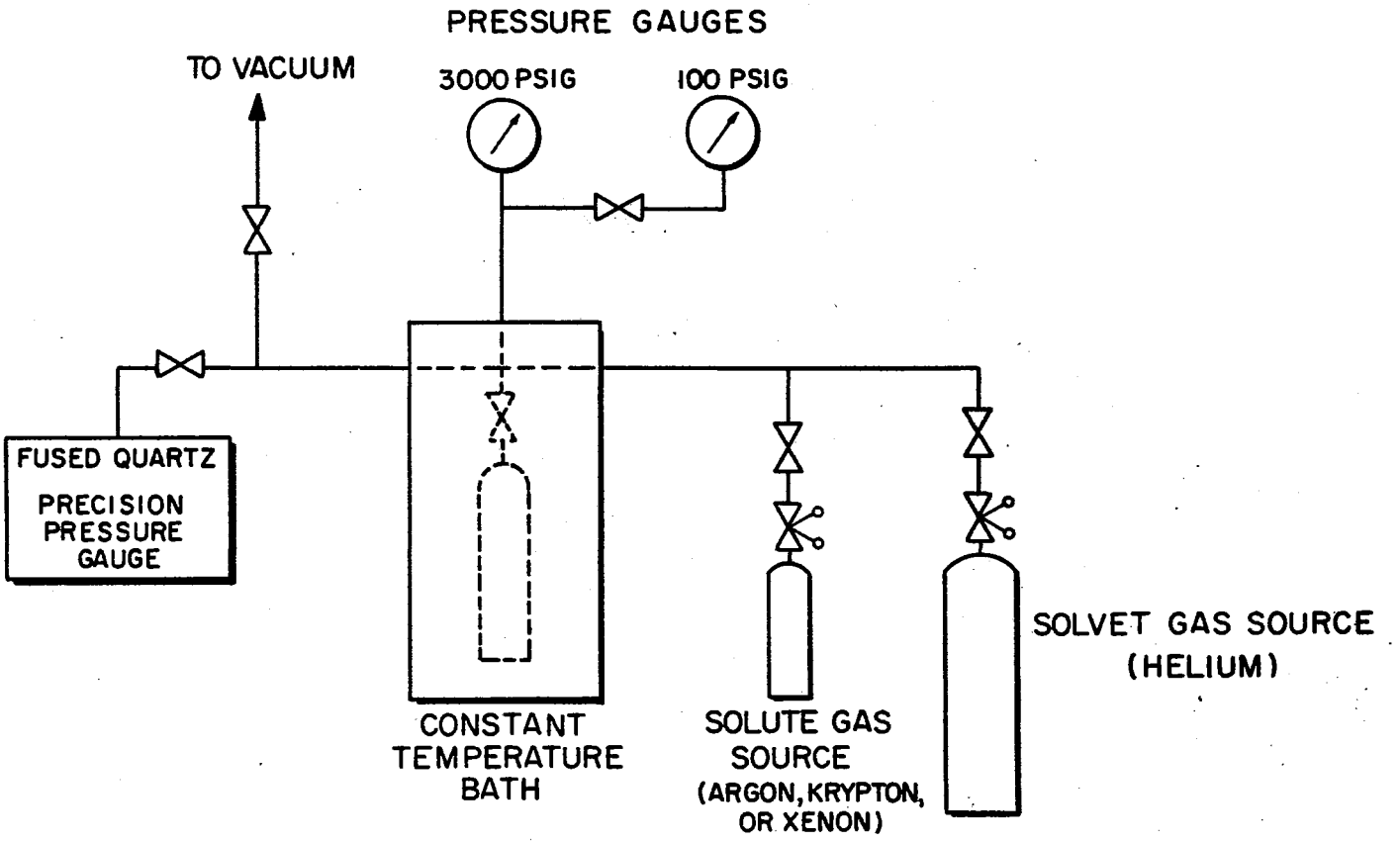

Figure 34. Schematic Diagram of Equipment Used to Prepare Sample Gas Mixtures

gas is injected into the mixture bomb and its pressure measured. After the bomb has reached thermal equilibrium, the transfer lines are evacuated and solvent gas is injected into the cylinder and the mixture pressure is measured.

The number of moles of the solute gas in the gas mixture sample bomb is given by

$$n_1 = P_1 V_{BOMB} / Z_1 RT_{BOMB} \qquad \text{(D-1)}$$

Likewise, the number of moles of the gas mixture in the mixture sample bomb is given by

$$n_m = P_m V_{BOMB} / Z_m RT_{BOMB} \qquad \text{(D-2)}$$

Combining equations (D-1) and (D-2) gives

$$y_1 = n_1 / n_m = (P_1/Z_1)/(P_m/Z_m) \qquad \text{(D-3)}$$

Equation (D-3) can be used to determine the mole fraction of the gas mixture directly from pressure measurements if a knowledge of the PVT behavior of the solute and the gas mixture is available. In a similar manner, one can show that the mole fraction of a gas mixture obtained by diluting a previously prepared gas mixture is given by

$$y_1' = [(P_1'/Z_1')/(P_m/Z_m)]y_1 \qquad \text{(D-4)}$$

where

y_1' = mole fraction of component "1" in the new mixture

P_1' = pressure measurement of solute (i.e., mixture to be diluted)

Z_1' = compressibility factor of solute (i.e., mixture to be diluted).

A typical example of a mixture prepared by each method is shown in Table XI.

Calibration mixtures were prepared for three different systems, namely, helium-argon, helium-krypton, and helium-xenon. A summary of the compositions and average detector responses for the calibration mixtures of these three systems is presented in Tables XII, XIII, and XIV. The gases used in preparing the gas mixtures are the same as those used in the actual solid-vapor equilibrium measurements. Their minimum purities are summarized elsewhere. The calibration mixtures can be made with an imprecision in the trace component mole fraction of ±0.35 to ±0.65%.

In calibrating the detector, the response of each sample mixture was measured at several different attenuations. The results of the calibrations for all three helium-trace component systems are presented in Tables XII to XIV and in Figures 35 to 43 which show the response of the detector plotted as a function of trace component mole fraction for lines of constant attenuation of the phase meter of the ultrasonic detector.

Originally, three commercial helium-krypton mixtures of known composition (516, 2400, and 9600 PPM mole fraction krypton) were purchased to calibrate the ultrasonic detector. Unfortunately, the uncertainty in the trace component mole fraction was ±5% for these commercial mixtures which is approximately ten times greater than the uncertainty in the mixtures prepared in this work. However, the commercial mixtures could still be used as a partial check on the reliability of the calibration mixture technique used in this study.

Average detector responses to the mixtures of composition 2400 and

TABLE XI

TYPICAL EXAMPLES OF SAMPLE MIXTURE CALCULATIONS

Example 1: Helium-Krypton System

Solute Pressure Reading (T. I. Gauge) = 184.54

Mixture Pressure Reading (3000 psig Heise Gauge) = 800 psia

Corrected Solute Pressure = 182.65 mm Hg (4.7880 psia)

Z of Pure Krypton = 0.999313 (34)

Z of Helium-Krypton Mixture = 1.0242 (11)

$$y_{Kr} = (P_1/Z_1)/(P_m/Z_m) = \frac{(4.7880/0.999313)}{(800/1.0242)}(10^6) = 4532 \text{ PPM}$$

Example 2: Helium-Xenon System

(Mixture Dilution Technique)

Original Mixture Composition = 1218 PPM Xenon

Barometer = 14.15 psia

Solute Pressure Reading (100 psig Heise Gauge) = 80.50 psig

Mixture Pressure Reading (3000 psia Heise Gauge) = 783 psia

Corrected Solute Pressure = 94.65 psia

Z of Mixture Being Diluted = 1.0031 (2, 34)

Z of New Mixture = 1.0256 (2, 34)

$$y'_{Xe} = (P'_1/Z'_1)/(P_m/Z_m) = \frac{(94.65/1.0031)}{(783/1.0256)}(1218) = 150.5 \text{ PPM}$$

TABLE XII

HELIUM-ARGON CALIBRATION MIXTURES

PVT Behavior Reference: Argon (34); Helium-Argon (3)

Mixture Composition (Trace Component Mole Fraction) PPM	Average Detector Response		
	X256*	X512*	X1024*
19,850	40.1	19.9	9.7
34,873	66.6	33.1	16.2
49,950	93.0	46.3	22.8
49,990	93.2	46.5	23.0
63,110		60.0	29.8
80,350		82.2	41.0
99,460			52.0
118,960			61.3
120,320			61.6
138,240			70.5
139,000			70.7

*Detector Attenuation

TABLE XIII

HELIUM-KRYPTON CALIBRATION MIXTURES

PVT Behavior Reference: Krypton (34); Helium-Krypton (11)

Mixture Composition (Trace Component Mole Fraction) PPM	X16*	X32*	X64*	X128*	X256*	X512*	X1024*
489	38.1	18.4					
1,195	93.2	46.3	22.8	11.0			
2,400**		95.3	47.5	23.3			
2,516		94.2	46.6	23.1			
4,517			82.7	41.2	20.0		
4,532			83.1	41.4	20.2		
6,640				59.7	29.6	14.2	
9,600**				88.1	43.7	21.9	
9,978				87.2	43.3	21.3	
10,000				87.2	43.2	21.2	
19,770					80.1	39.8	19.4
22,260					86.9	43.1	21.3
31,350						65.2	32.2
39,790						89.5	44.5
69,460							77.0

*Detector Attenuation

**Sample Mixtures from Air Products and Chemicals

TABLE XIV

HELIUM-XENON CALIBRATION MIXTURES

PVT Behavior Reference: Xenon (34); Helium-Xenon (2,34)

Mixture Composition (Trace Component Mole Fraction) PPM	X2*	X4*	X8*	X16*	X32*	X64*	X128*	X256*	X512*	X1024*
74.2	68.8	34.5	16.8							
150.5		70.0	34.7	17.1						
297.3			69.1	34.7	16.9					
301			69.5	34.9	17.0					
603				70.1	35.0	17.0				
1218					71.3	35.4	17.4			
2526						71.8	35.9	17.7		
2535						71.9	36.0	18.0		
5034							69.2	34.6	17.1	
5035							69.1	34.6	17.2	
7611								51.1	25.4	12.4
10,110								66.4	33.2	16.3
14,920								98.0	49.1	24.3
20,240									71.5	35.7
30,340										55.8
49,560										91.2

*Detector Attenuation

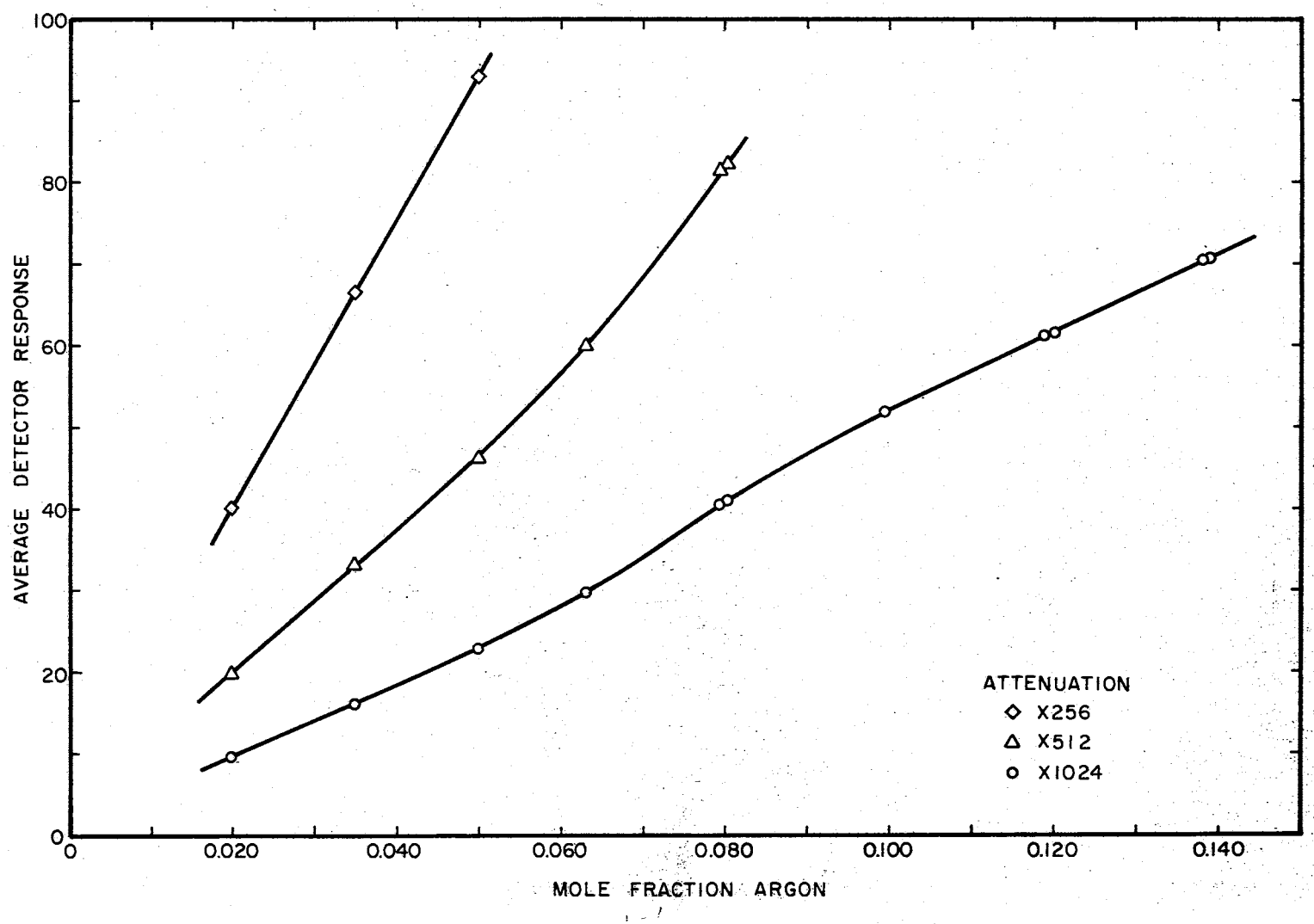

Figure 35. Detector Calibration Curves for the Helium-Argon System

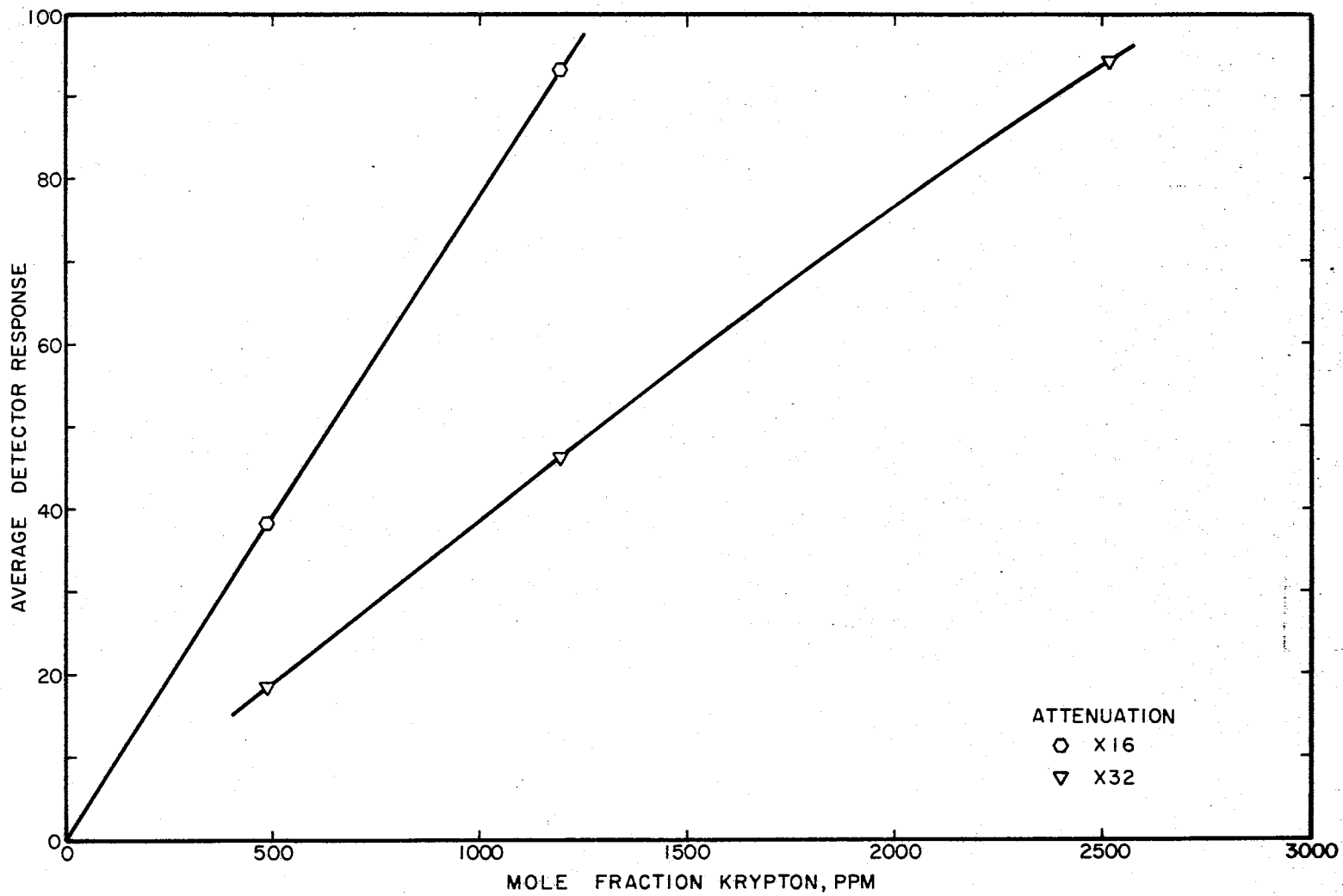

Figure 36. Detector Calibration Curves for the Helium-Krypton System

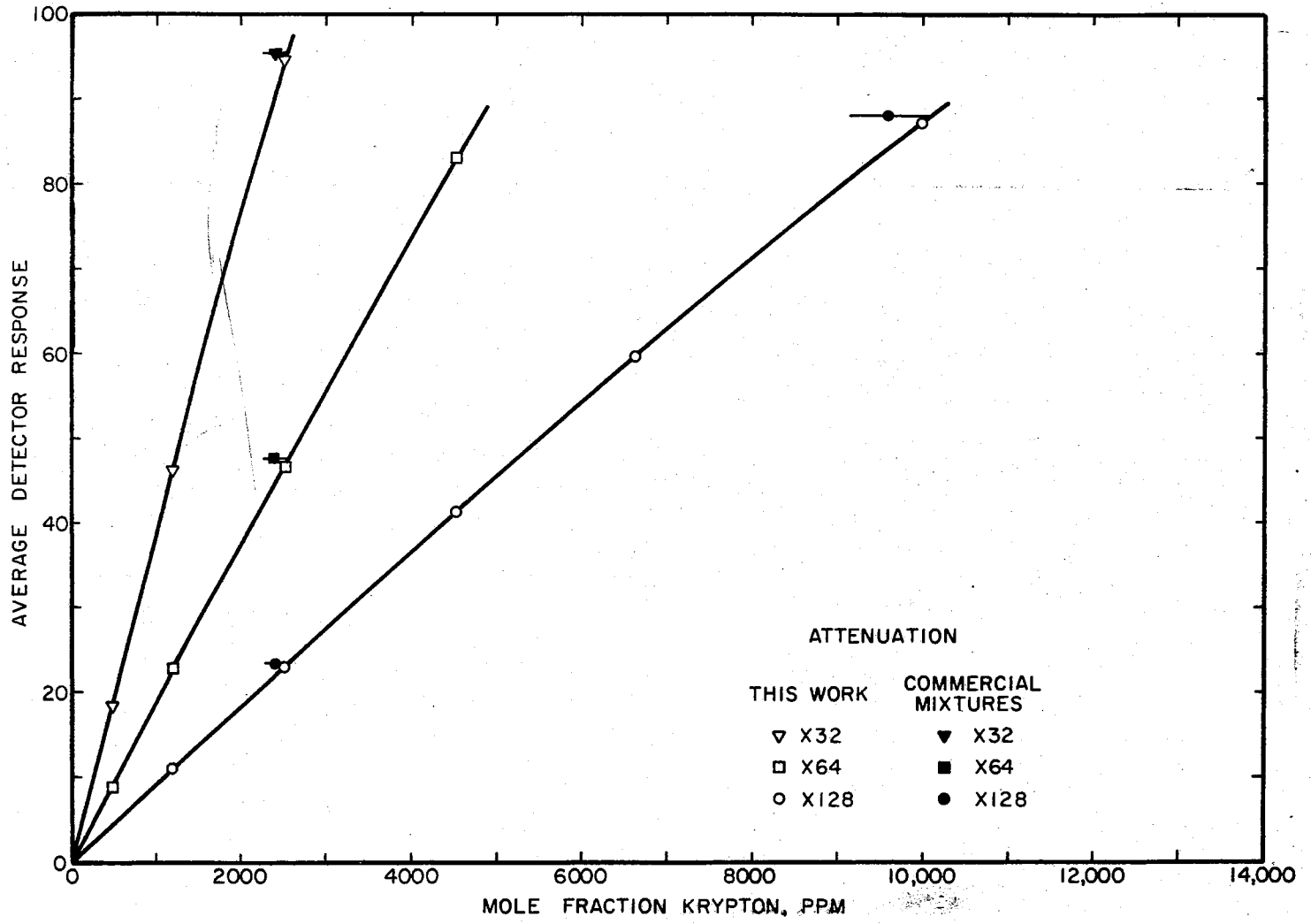

Figure 37. Detector Calibration Curves for the Helium-Krypton System

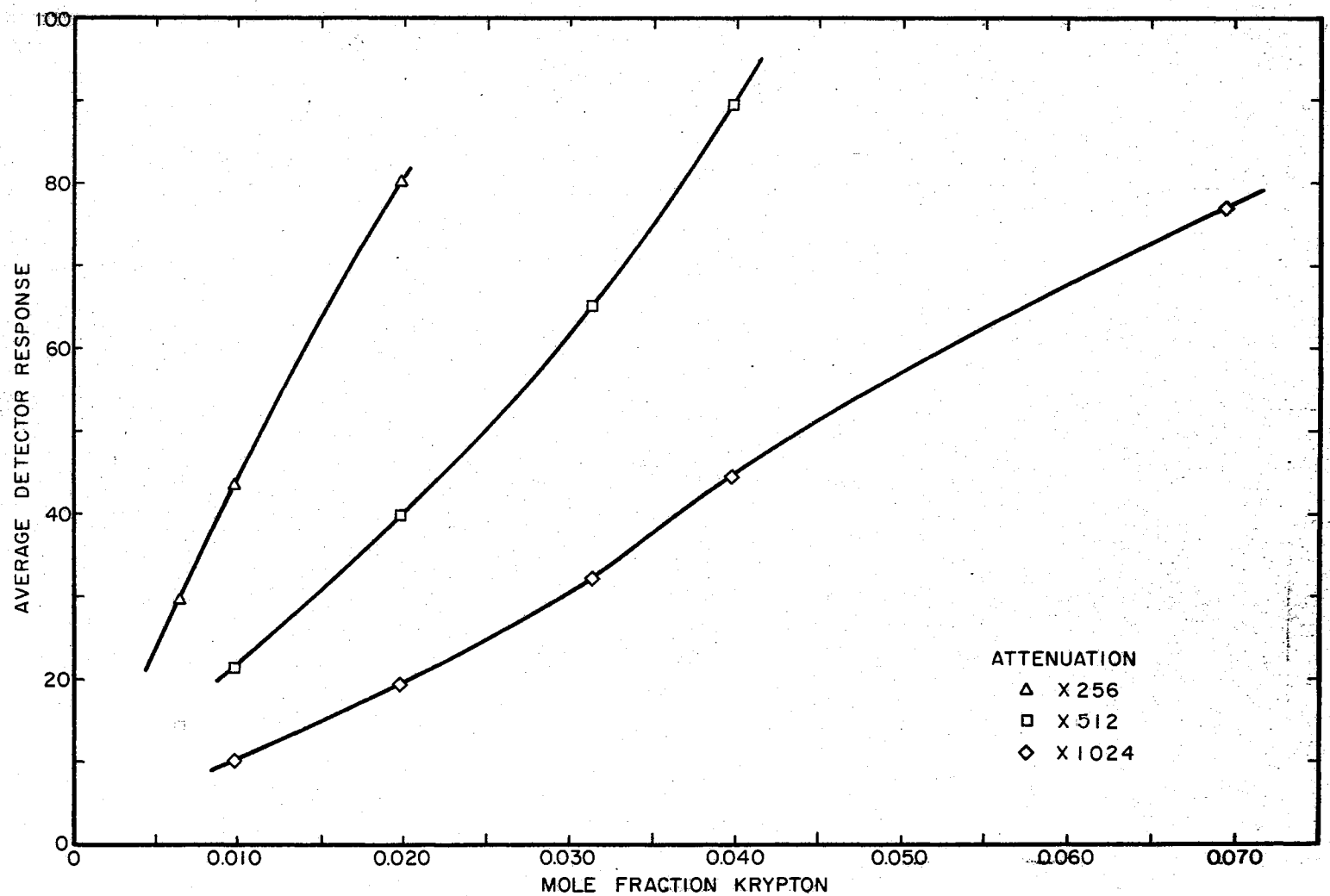

Figure 38. Detector Calibration Curves for the Helium-Krypton System

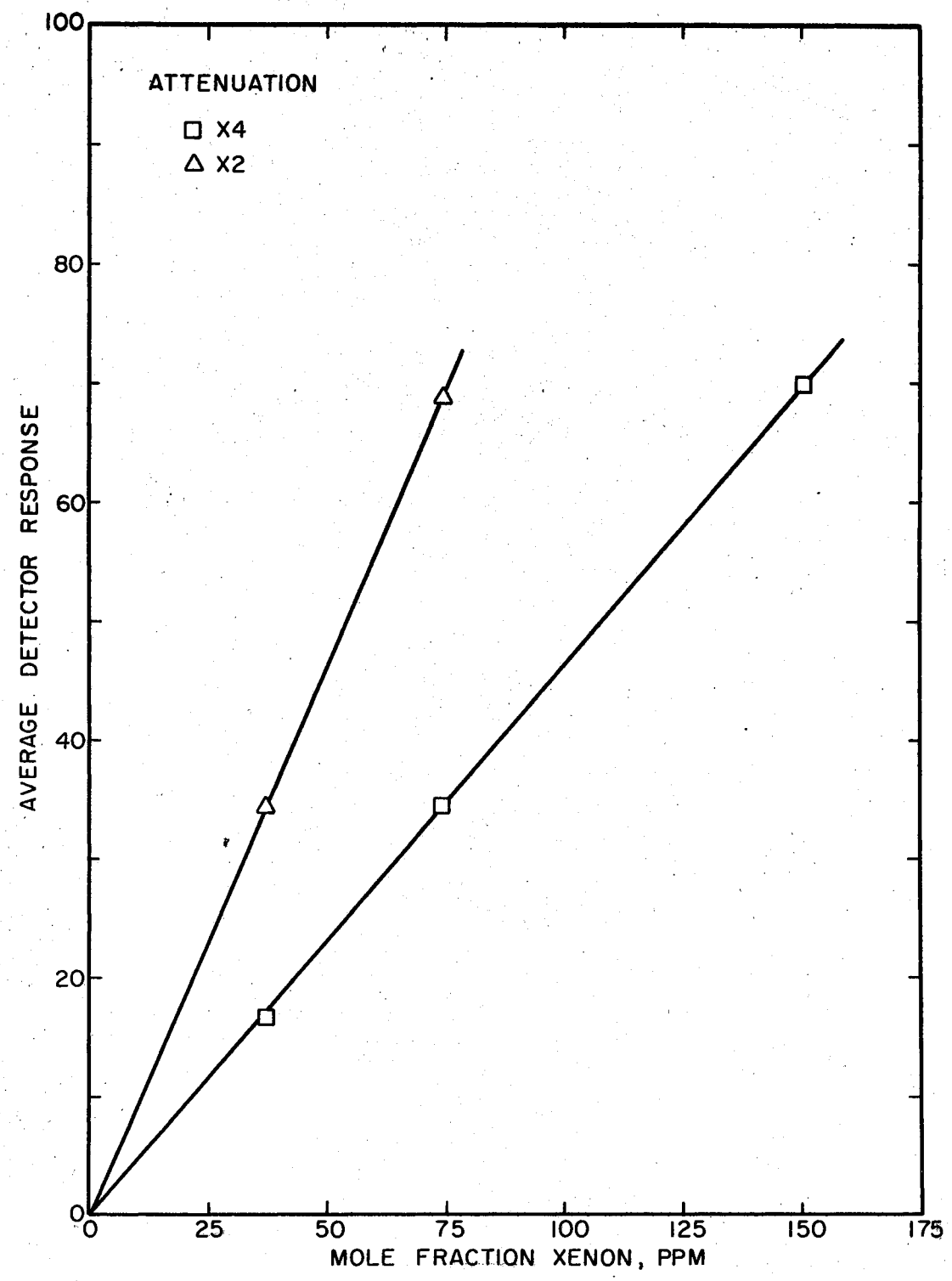

Figure 39. Detector Calibration Curves for the Helium-Xenon System

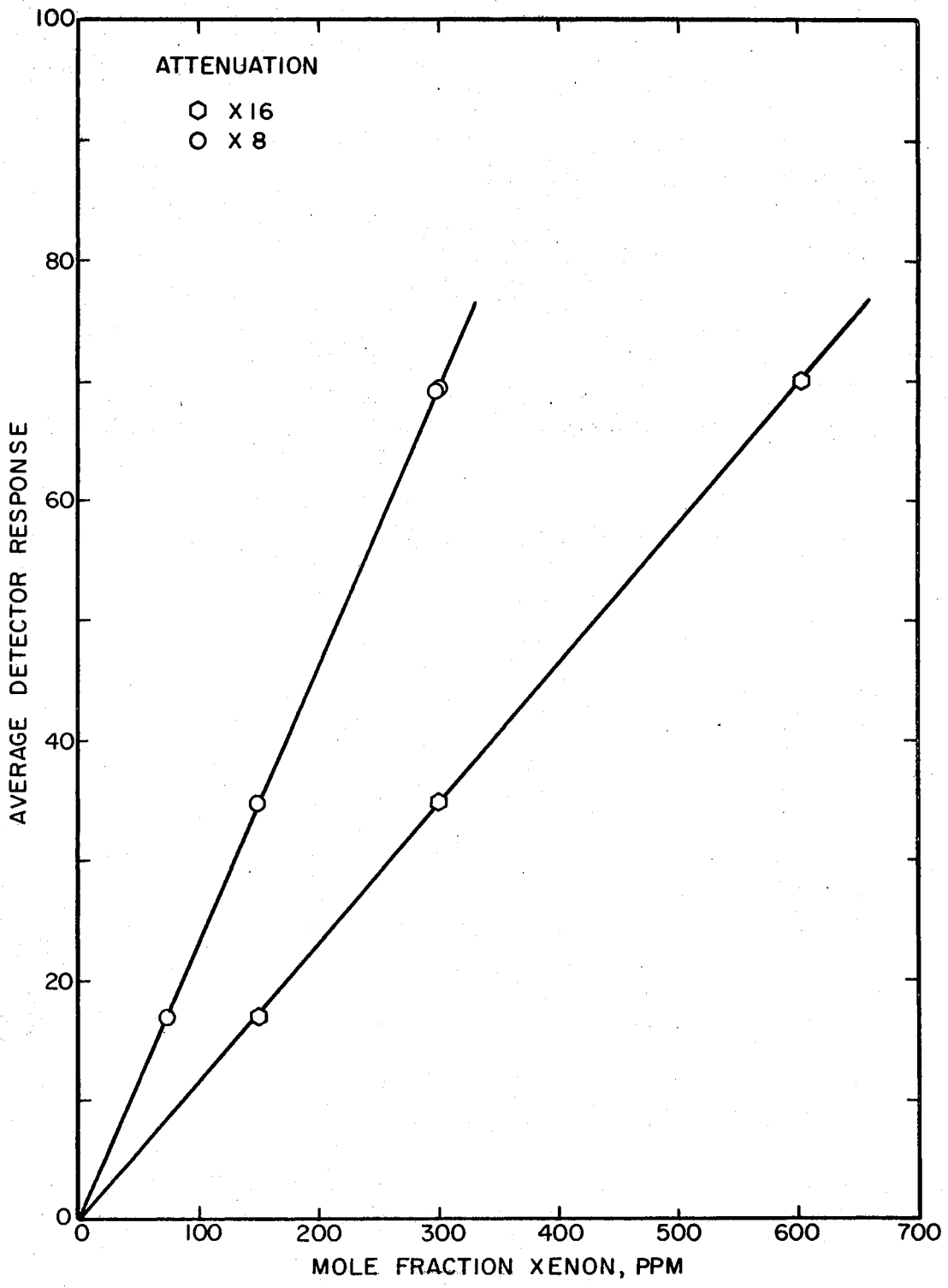

Figure 40. Detector Calibration Curves for the Helium-Xenon System

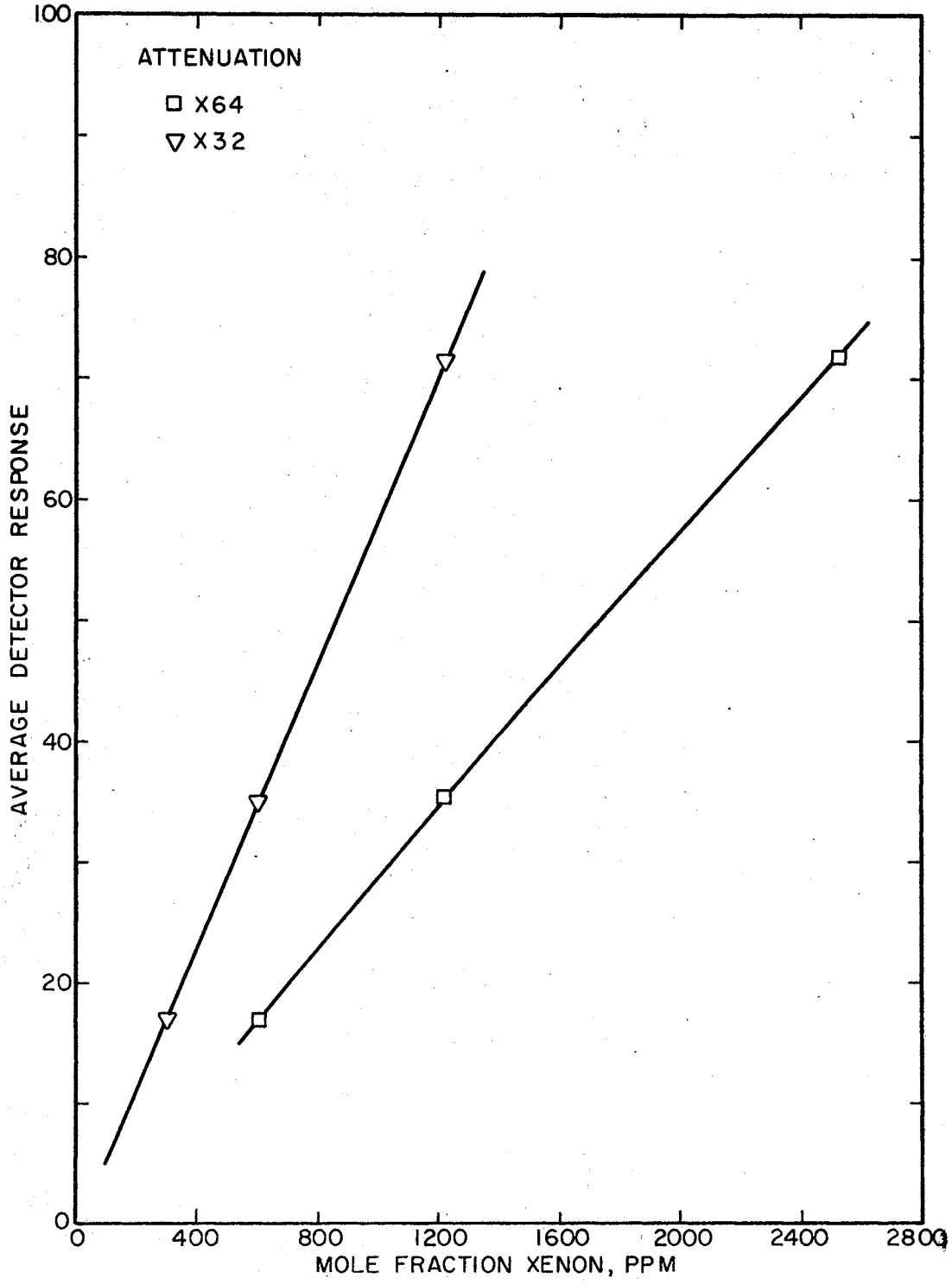

Figure 41. Detector Calibration Curves for the Helium-Xenon System

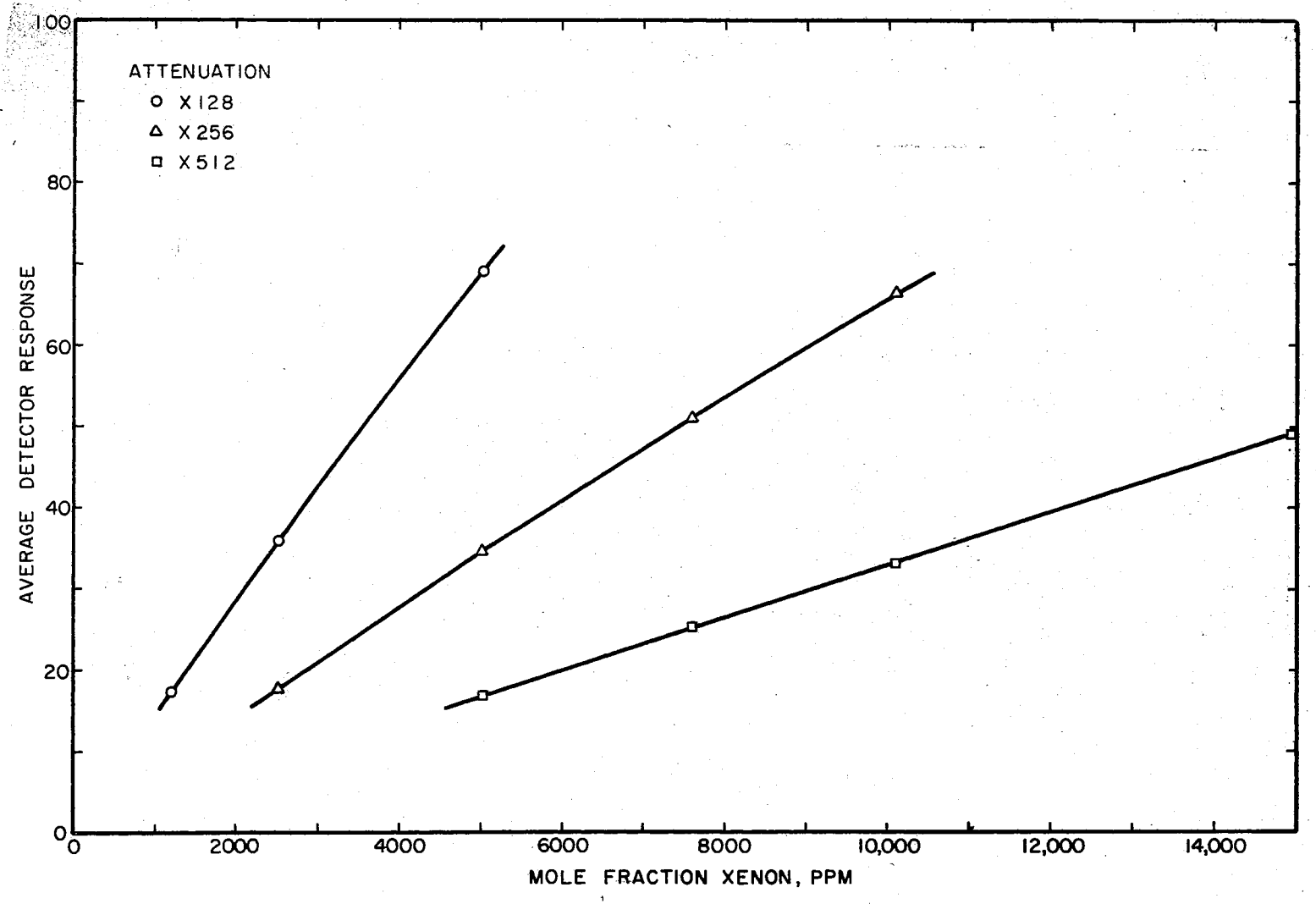

Figure 42. Detector Calibration Curves for the Helium-Xenon System

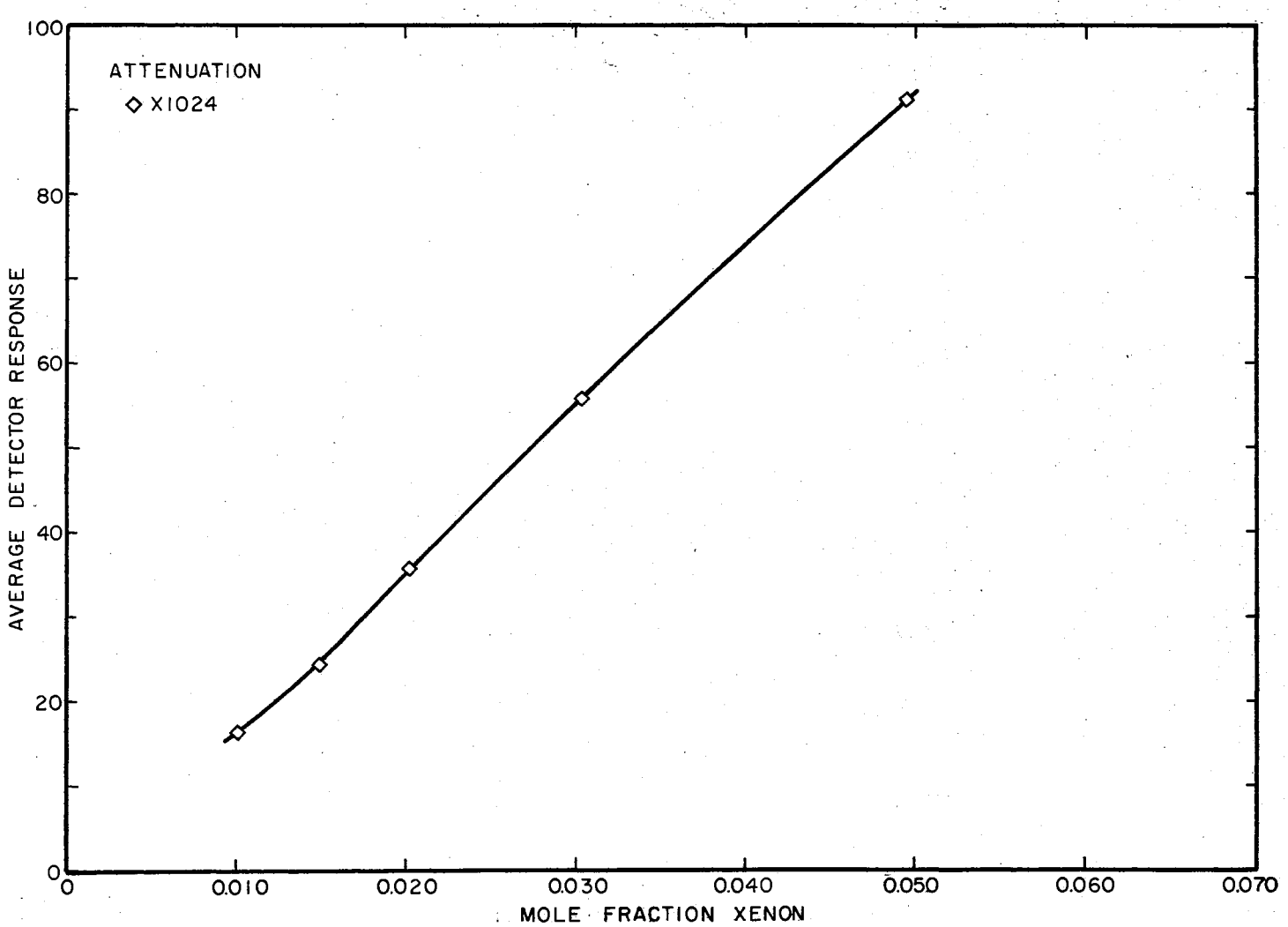

Figure 43. Detector Calibration Curve for the Helium-Xenon System

9600 PPM mole fraction krypton are shown in Figure 37. Composition error bands are included on these points. Figure 37 indicates that the results of this work agree relatively well (approximately within the uncertainty of the data) with the commercial mixture results. However, a more meaningful test of the reliability of the calibration mixture technique used in this work was provided by making liquid-vapor equilibrium measurements on the helium-argon system (discussed in Appendix E). The measurements taken in this work agreed well (nominal scatter of ±1% in argon enhancement factors) with the data of other investigators, a good indication of the reliability of the calibration mixture technique of the present study.

APPENDIX E

ARGON VAPOR PRESSURE MEASUREMENTS

Argon vapor pressure measurements were made in order to confirm the reliability of the platinum resistance thermometer. The argon used for these measurements had less than 50 ppm impurities. Measurements were made on two separate occasions, namely, before the solid-vapor equilibrium data were taken on each of the two systems studied in this work. The first argon vapor pressure data were taken before the helium-krypton solid-vapor equilibrium measurements were made. This data covered a temperature range from 100 to 116° K. The vapor pressure measurements were repeated over a temperature range of 100 to 125° K. before the helium-xenon system was studied.

Before the vapor pressure measurements were made, the equilibrium cell was flushed with argon and then well evacuated. Next, argon was loaded into the cell through the cell fill line from a transfer cylinder which contained argon at a pressure of approximately 200 psig. The argon was loaded at a cell temperature of 90° K. in order to place as much liquid as possible into the equilibrium cell. Finally, the cell was sealed off except for the line to the pressure gauges and measurements were made at various temperatures.

The vapor pressures were measured using a Heise bourdon tube pressure gauge with a pressure range of 0 to 300 psig and a precision of ±0.3 psi. The results of these measurements for each case are presented

in Tables XV and XVI where the data in this work were compared with that of Clark, et al (8). These results show that the vapor pressure measurements agree well with the other experimental data within the precision of the pressure measurements. Therefore, the platinum resistance thermometer measurements were considered to be reliable.

TABLE XV

ARGON VAPOR PRESSURE MEASUREMENTS

(1st Trial, 6/70)

Experimental Temperature ^{o}K	Experimental Vapor Pressure psia	Calculated Vapor Pressure** psia	Deviation Exp - Calc psia	Calculated Temperature** ^{o}K	Deviation Exp - Calc ^{o}K
104.99	68.66	68.73	-0.07	104.97	0.02
110.00	96.56	96.82	-0.26	109.95	0.05
116.00	140.16*	140.39	-0.23	115.97	0.03
110.00	96.76	96.82	-0.06	110.00	0.00
99.99	47.76	47.15	0.61	100.10	-0.11

*Hiza obtained 140.43 psia

**Determined from the smoothed experimental data (8)

TABLE XVI

ARGON VAPOR PRESSURE MEASUREMENTS

(2nd Trial, 11/70)

Experimental Temperature ^{o}K	Experimental Vapor Pressure psia	Calculated Vapor Pressure** psia	Deviation Exp - Calc psia	Calculated Temperature** ^{o}K	Deviation Exp - Calc ^{o}K
100.15	47.63	47.91	-0.28	100.10	0.05
105.00	68.73	68.63	0.10	105.04	-0.04
110.00	96.73	96.70	0.03	110.00	0.00
116.00	140.23*	140.39	-0.16	115.98	0.02
120.00	176.43	176.50	-0.07	120.0	0.00
125.00	229.83	229.70	-0.13	125.0	0.00

*Hiza obtained 140.43 psia

**Determined from the smoothed experimental data (8)

APPENDIX F

LIQUID-VAPOR EQUILIBRIUM MEASUREMENTS ON THE HELUIM-ARGON SYSTEM

Liquid-vapor equilibrium measurements were made on the helium-argon system as another means of establishing the reliability of the experimental equipment. Because pure argon remained in the equilibrium cell from the vapor pressure test, refilling the cell was unnecessary. The cell was cooled to 108.02° K., pressured with helium, and measurements were made at three different pressures beginning with the highest pressure first. In a similar manner, data were taken at 91.98° K. Only the vapor phase was analyzed.

The experimental results, i.e., the concentration measurements of the argon in the vapor phase, are presented in Table XVII where they are compared with the data of Mullins and Ziegler (43) and Hiza (20). A sensitive graphical comparison of these experimental data can be made by plotting enhancement factor data. The enhancement factor ϕ_i is the ratio of the partial pressure of a component in the vapor phase to the vapor pressure of that component, $y_i P/P_i^o$. The enhancement factors obtained in this work are compared with those of other investigators in Figures 44 and 45. The agreement of all the data appears to be quite good indicating that the experimental equipment was functioning properly.

TABLE XVII

LIQUID-VAPOR EQUILIBRIUM DATA FOR THE HELIUM-ARGON SYSTEM

Temp., °K	Press., atm	Vapor Phase Mole Fraction of Argon		
		This Work	Hiza (20)	Mullins and Ziegler (43)
108.02	102.75	0.0856		
	102.68	0.0856		
	100.7			0.0877
	91.7		0.0960	
	80.50	0.1042		
	80.43	0.1043		
	80.00		0.106	0.1034
	60.00		0.131	0.129
	59.76	0.1293		
	59.65	0.1299		
91.98	119.80			0.02252
	107.99	0.0238		
	100.27			0.02535
	99.55	0.0254		
	80.20			0.02947
	79.55	0.0294		
	79.41	0.0294		
	60.30			0.03616
	59.40	0.0367		
	40.28	0.0500		
	40.14			0.0504
	19.92			0.0916
	19.84	0.0922		
	19.60	0.0942		

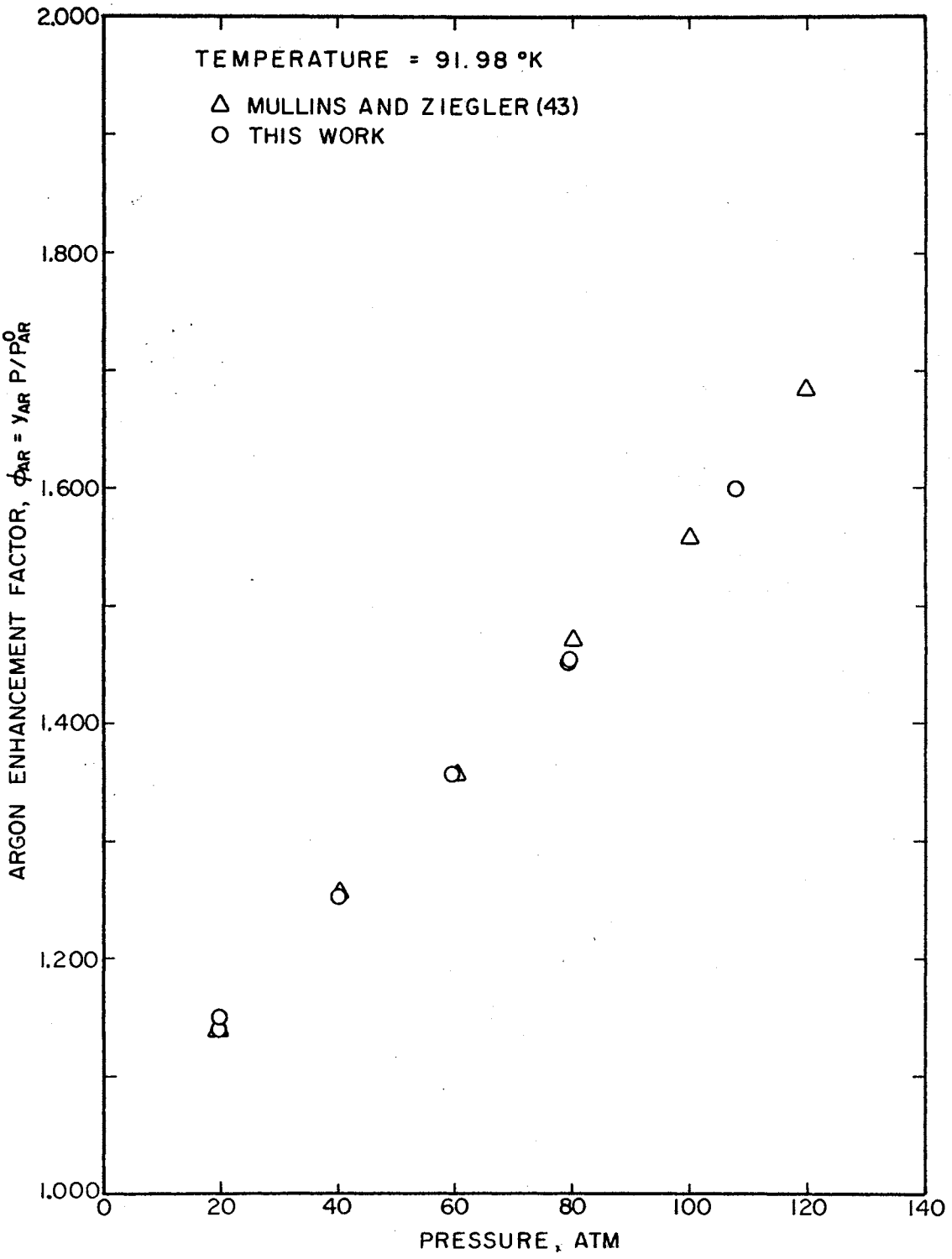

Figure 44. Argon Enhancement Factors for the Helium-Argon System

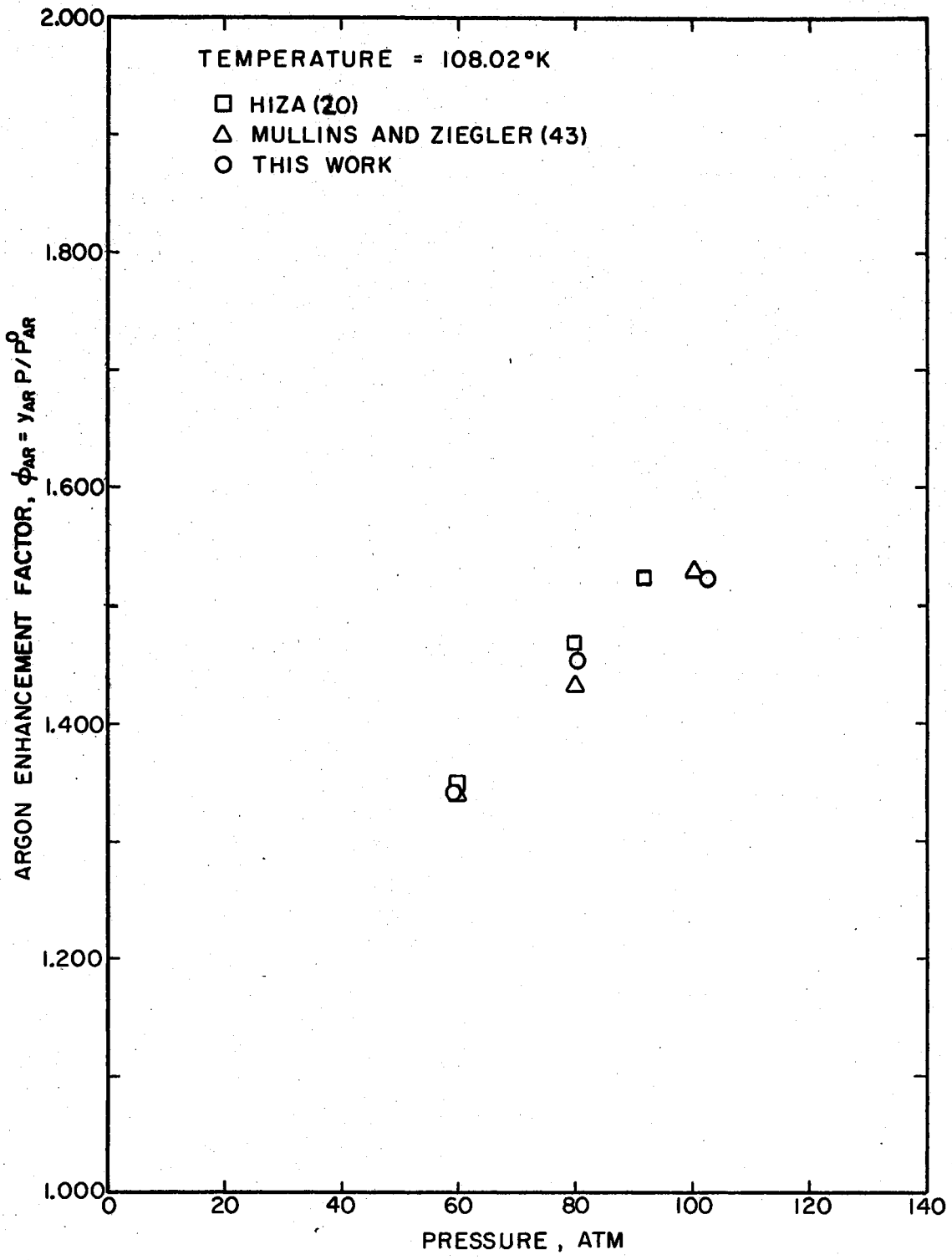

Figure 45. Argon Enhancement Factors for the Helium-Argon System

APPENDIX G

SAMPLE EXPERIMENTAL RUNS

For each experimental run the following data were recorded:

(1) the barometric pressure

(2) the G-2 Muellar Bridge resistance readings of the platinum resistance thermometer

(3) the Heise gauge readings

(4) the actual system pressure

(5) the attenuation setting and response (peak height) of the ultrasonic detector

(6) the mole fraction of the trace component in the vapor phase (determined from the detector response and detector calibration curves).

Some typical examples of experimental runs are presented in Tables XVIII through XXI.

TABLE XVIII

EXPERIMENTAL RUN NO. 16 (7/4/70)

Barometer = 743.5 mm Hg (14.38 psia)

Data Point No.	Resistance Readings of the Platinum Resistance Thermometer			Heise Gauge Reading psig	Actual System Pressure*		Detector Attenuation	Average Detector Response	Mole Fraction Krypton**
	N	R	Average		psia	atm			
1'	8.9627	8.9463	8.9545	1604	1619	110.17	X128	70.2	0.00785
2	8.9627	8.9463	8.9545	1315	1332	90.64	X128	80.7	0.00915
3'	8.9627	8.9463	8.9545	1314	1331	90.57	X128	80.8	0.00916
4	8.9627	8.9463	8.9545	1011	1028	69.95	X256	49.7	0.0115
5'	8.9627	8.9463	8.9545	694.2	709.4	48.27	X256	65.8	0.0159
6	8.9627	8.9463	8.9545	427.0	442.6	30.12	X512	49.8	0.0246
7'	8.9627	8.9463	8.9545	133.8	148.4	10.10	X1024	77.0	0.0695

Average = 8.9545; Average Temperature = 115.00±0.02° K.

'Indicates that the vapor flow leaving the equilibrium cell is at least twice the normal rate.

*Determined by adding the appropriate calibration correction and barometric pressure to the Heise Gauge reading.

**Determined from the detector response and the detector calibration curves.

TABLE XIX

EXPERIMENTAL RUN NO. 22 (7/10/70)

Barometer = 738.4 mm Hg (14.28 psia)

Data Point No.	Resistance Readings of the Platinum Resistance Thermometer			Heise Gauge Reading psig	Actual System Pressure*		Detector Attenuation	Average Detector Response	Mole Fraction Krypton**
	N	R	Average		psia	atm			
1'	6.7662	6.7500	6.7581	1642	1657	112.75	X16	60.0	0.000769
2	6.7662	6.7500	6.7581	1447	1463	99.55	X16	65.7	0.000843
3	6.7662	6.7500	6.7581	1161	1178	80.16	X16	76.7	0.000985
4'	6.7662	6.7500	6.7581	867.0	882.5	60.05	X32	47.3	0.001225
5	6.7662	6.7500	6.7581	572.8	588.2	40.02	X32	66.0	0.001712
6'	6.7662	6.7500	6.7581	280.4	295.3	20.09	X64	58.9	0.00318
7	6.7662	6.7500	6.7581	136.5	151.0	10.27	X128	54.0	0.00598

Average = 6.7581; Average Temperature = 95.00±0.03° K.

'Indicates that the vapor flow leaving the equilibrium cell is at least twice the normal rate.

*Determined by adding the appropriate calibration correction and barometric pressure to the Heise gauge reading.

**Determined from the detector response and the detector calibration curves.

TABLE XX

EXPERIMENTAL RUN NO. 34 (12/3/70)

Barometer = 744.6 mm Hg (14.40 psia)

Data Point No.	Resistance Readings of the Platinum Resistance Thermometer			Heise Gauge Reading	Actual System Pressure*		Detector Attenuation	Average Detector Response	Mole Fraction Xenon**
	N	R	Average	psig	psia	atm			
1	9.5063	9.4913	9.4988	1731	1746	118.64	X8	36.7	0.000160
2	9.5063	9.4913	9.4988	1435	1451	98.76	X8	42.7	0.0001855
3'	9.5063	9.4913	9.4988	1435	1451	98.76	X8	42.9	0.0001865
4	9.5063	9.4913	9.4988	1162	1179	80.25	X8	51.0	0.000221
5	9.5063	9.4913	9.4988	872.1	885.7	60.27	X8	66.9	0.000289
6	9.5063	9.4913	9.4988	576.8	592.3	40.30	X16	48.1	0.000414
7'	9.5063	9.4913	9.4988	574.8	590.3	40.17	X16	48.2	0.000415
8	9.5063	9.4913	9.4988	275.8	290.9	19.79	X32	46.3	0.000798
9	9.5063	9.4913	9.4988	135.6	150.2	10.22	X64	43.5	0.001500

Average = 9.4988; Average Temperature = 120.00±0.02° K.

'Indicates that the vapor flow leaving the equilibrium cell is at least twice the normal rate.

*Determined by adding the appropriate calibration correction and barometric pressure to the Heise gauge reading.

**Determined from the detector response and the detector calibration curves.

TABLE XXI

EXPERIMENTAL RUN NO. 56 (2/5/71)

Barometer = 738.0 mm Hg (14.27 psia)

Data Point No.	Resistance Readings of the Platinum Resistance Thermometer			Heise Gauge Reading	Actual System Pressure*		Detector Attenuation	Average Detector Response	Mole Fraction Xenon**
	N	R	Average	psig	psia	atm			
1	13.2699	13.2549	13.2624	1762	1777	120.94	X128	63.9	0.004625
2	13.2699	13.2549	13.2624	1456	1472	100.18	X256	37.7	0.00550
3'	13.2699	13.2549	13.2624	1456	1472	100.18	X256	37.6	0.00549
4	13.2699	13.2549	13.2624	1160	1177	80.11	X256	45.6	0.00675
5'	13.2699	13.2549	13.2624	1160	1177	80.11	X256	45.6	0.00675
6	13.2699	13.2549	13.2624	867.2	882.7	60.06	X256	59.0	0.008875
7	13.2699	13.2549	13.2624	497.3	512.7	34.89	X512	49.9	0.01513
8'	13.2699	13.2549	13.2624	497.3	512.7	34.89	X512	49.8	0.01510
9	13.2699	13.2549	13.2624	197.9	212.5	14.46	X1024	65.1	0.03525

Average = 13.2624; Average Temperature = 155.00±0.01° K.

'Indicates that the equilibrium cell outlet temperature has been increased by approximately 3-4° C.

*Determined by adding the appropriate calibration correction and barometric pressure to the Heise gauge reading.

**Determined from the detector response and the detector calibration curves.

APPENDIX H

SURVEY OF THE INFORMATION NEEDED TO ANALYZE THE SOLID-VAPOR EQUILIBRIUM DATA

The solid molar volumes of krypton and xenon for the temperatures of interest are presented in Table XXII. The krypton solid molar volumes were obtained by interpolating between experimental values of the density at 80° K. and 115.78° K. (triple point of krypton) using the volume expansivity, $\beta = (\partial V/\partial T)_P/V$. The experimental solid densities and volume expansivity were obtained from the tabulations of Cook (9). The xenon solid molar volumes were obtained from the experimental data of Packard and Swenson (46) as tabulated in an article by Trefny and Serin (58).

The experimental helium second and third virial coefficient data of several investigators are presented in Figures 46 and 47. Also appearing in these figures are values from the work of Levelt-Sengers, et al (34) who have performed an extensive compilation of second and third virial coefficient data. In order to obtain second and third virial coefficients at the appropriate temperatures, smooth curves through the experimental data were drawn by inspection.

The second virial coefficients of krypton and xenon at the temperatures of interest were obtained from the Dymond-Alder potential (12) using the krypton and xenon potential parameters obtained in the work of Lin and Robinson (35). These predicted krypton and xenon second virial coefficients obtained from Figure 46 are presented in Table XXIII.

TABLE XXII

SOLID MOLAR VOLUMES OF KRYPTON AND XENON

Krypton			Xenon	
Temperature ^{o}K	Density g/cm^3	Molar Volume cc/g-mole	Temperature ^{o}K	Molar Volume cc/g-mole
90	2.900	28.92	120	37.25
95	2.886	29.06	130	37.58
100	2.872	29.20	140	37.91
105	2.858	29.34	155	38.31
110	2.844	29.49		
115	2.829	29.64		

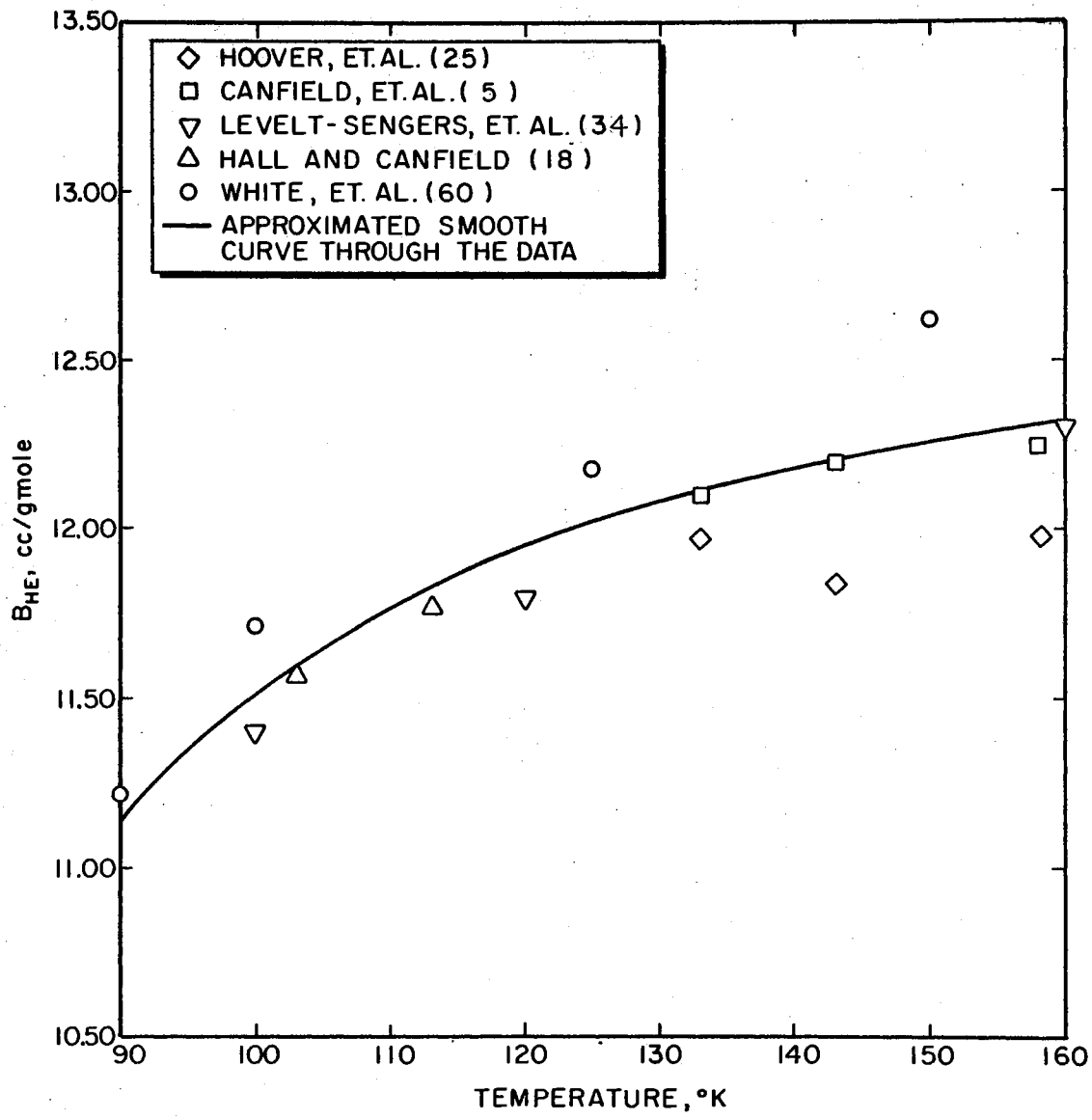

Figure 46. Second Virial Coefficients for Helium

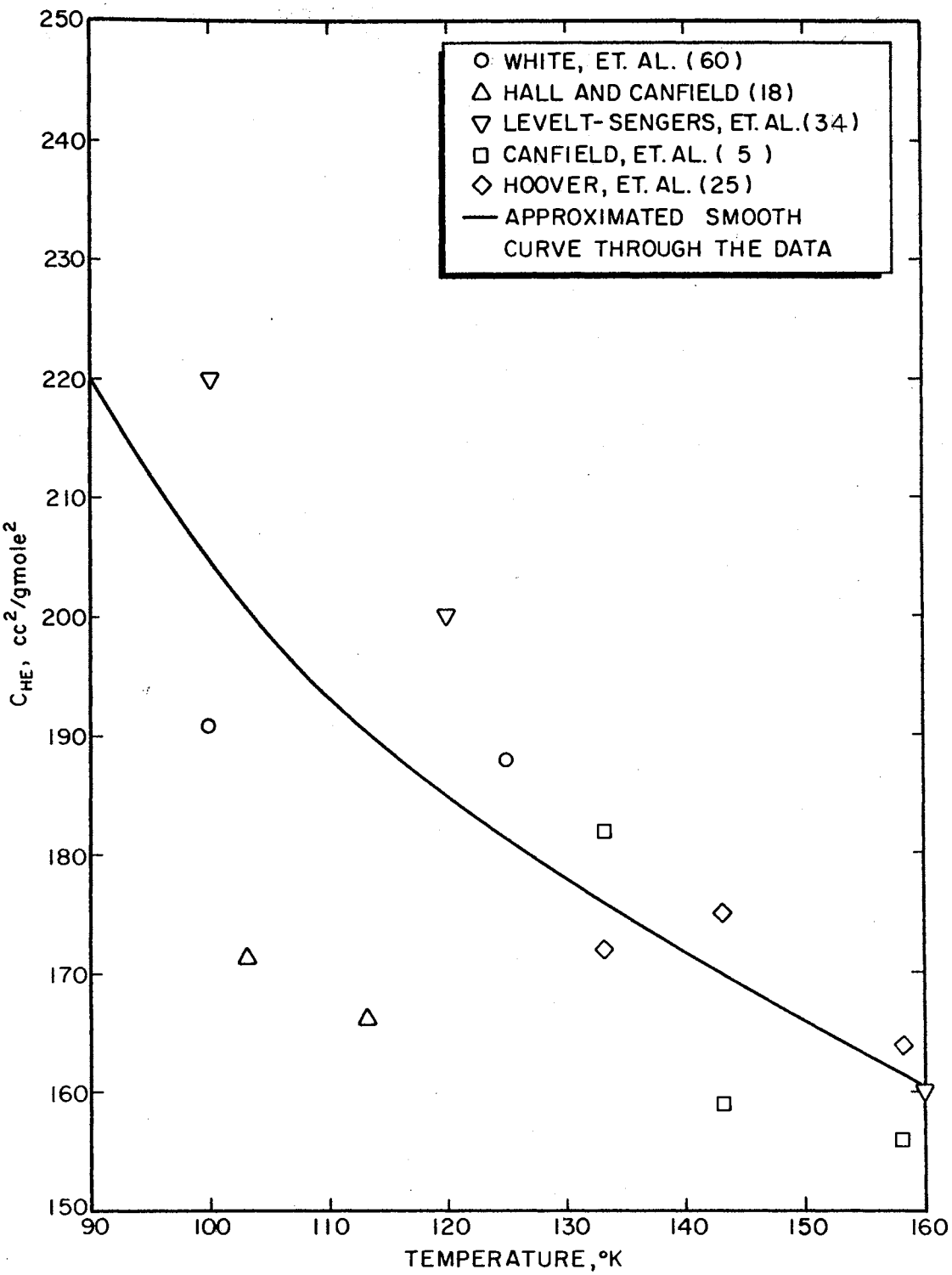

Figure 47. Third Virial Coefficients for Helium

TABLE XXIII

SECOND VIRIAL COEFFICIENTS

Temperature °K	Second Virial Coefficient, B_{12} cc/g-mole		
	He	Kr	Xe
90	11.14	-560.44	
95	11.35	-498.16	
100	11.52	-447.55	
105	11.66	-403.21	
110	11.77	-367.64	
115	11.87	-335.13	
120	11.95		-780.86
130	12.08		-657.13
140	12.18		-561.57
155	12.29		-456.75

The third virial coefficients of pure krypton and xenon, the interaction virial coefficient, C_{122}, and the first guess for the interaction virial coefficient, C_{112}, were all obtained from the tabulated reduced third virial coefficients for the Lennard-Jones potential presented by Sherwood and Prausnitz (54). The L-J parameters for krypton and xenon were obtained from Sherwood and Prausnitz (55) and the parameters for helium were obtained from Hirschfelder, Curtiss, and Bird (19). All the third virial coefficient data, including the values of the helium third virial coefficient which were obtained from Figure 47, are summarized in Table XXIV.

Several sources of krypton and xenon vapor pressure data were used in this study. Ziegler, et al have developed an excellent calculational technique for determining the vapor pressure of krypton (61) and xenon (62) which agrees relatively well with most of the experimental data of other investigators through 1964. Recently, Leming and Pollack (32) have experimentally determined krypton and xenon vapor pressures over a wide temperature range in the solid phase region.

In order to avoid relying on the available experimental vapor pressure data, the experimental solid-vapor equilibrium data were also used to determine the value of the vapor pressure in addition to the values of the interaction virials, B_{12} and C_{112}. A non-linear regression technique (discussed in detail elsewhere) was used to obtain the values of the vapor pressure, B_{12}, and C_{112}, that would give the best fit of the experimental solid-vapor equilibrium data to Equation (12). All the vapor pressure data used in this study are presented in Table XXV.

TABLE XXIV

THIRD VIRIAL COEFFICIENTS

Helium-Krypton

Temperature °K	C_{111} $(cc/g\text{-}mole)^2$	C_{112}* $(cc/g\text{-}mole)^2$	C_{122} $(cc/g\text{-}mole)^2$	C_{222} $(cc/g\text{-}mole)^2$
90	220.	286.	577.	-74750
95	212.	287.	617.	-51250
100	205.	288.	637.	-31500
105	199.	289.	650.	-20000
110	193.	290.	655.	-11920
115	189.	291.	655.	- 5900

Component "1" = helium

Component "2" = krypton

Helium-Xenon

Temperature °K	C_{111} $(cc/g\text{-}mole)^2$	C_{112}* $(cc/g\text{-}mole)^2$	C_{122} $(cc/g\text{-}mole)^2$	C_{222} $(cc/g\text{-}mole)^2$
120	185.	467.	2698.	-114,800
130	178.	455.	2450.	- 57,600
140	172.	442.	2233.	- 26,300
155	163.	428.	2013.	- 4,080

Component "1" = helium

Component "2" = xenon

*This value serves as a first guess for C_{112} in the iterative solution of Equation (12).

TABLE XXV

VAPOR PRESSURE DATA

Krypton

Temperature °K	Ziegler, et al Data atm.	Leming and Pollack Data* atm.	Best Fit of Solid-Vapor Equilibrium Data to Equation (35) atm.
90	0.02653	0.02645	0.02668
95	0.05811	0.05823	0.05844
100	0.1175	0.1178	0.1181
105	0.2217	0.2225	0.2230
110	0.3947	0.3960	0.3970
115	0.6682	0.6708	0.6721

Xenon

Temperature °K	Ziegler, et al Data atm.	Leming and Pollack Data* atm.	Best Fit of Solid-Vapor Equilibrium Data to Equation (35) atm.
120	0.01485	0.01520	0.01495
130	0.04951	0.04994	0.04964
140	0.1383	0.1392	0.1382
155	0.5015	0.5036	0.4990

*Interpolated values

APPENDIX I

ERROR ANALYSIS

In this study, the solid-vapor equilibrium data were used to regress the interaction virial coefficients (B_{12} and C_{112}) from the following equation form

$$Y = -BX - CX^2 \tag{35}$$

where

$$Y = \ln \phi_2 - \bar{V}_{2S}(P - P_2^o)/RT - B_{22}P_2^o/RT - \ln Z_m + 2y_2B_{22}/\bar{V}_m + (6y_1y_2C_{122} + 3y_2^2C_{222})/2\bar{V}_m^2$$

$$X = y_1/\bar{V}_m$$

$$B = 2B_{12}$$

$$C = 3C_{112}/2$$

In the least squares regression each experimental value of Y was weighted by its associated standard error, ε_Y.

When a quantity Q is a function of several experimentally determined quantities,

$$Q = Q(x_1, x_2, \ldots, x_n)$$

then the effect of the independent random error in these quantities on Q is given by

$$\varepsilon_Q^2 = \sum_{i=1}^{n} \left(\frac{\partial Q}{\partial x_i} \varepsilon_i\right)^2 \tag{I-1}$$

All the experimental errors in this study are assumed to be independent errors.

In order to determine the value of ε_Y, the equation for Y is written in the form

$$Y = A - B - C - D + E + F \qquad (I\text{-}2)$$

where

$$A = \ln \phi_2$$

$$B = \ln Z_m$$

$$C = \bar{V}_{2S}(P - P_2^o)/RT$$

$$D = B_{22}P_2^o/RT$$

$$E = 2y_2B_{22}/\bar{V}_m$$

$$F = (6y_1y_2C_{122} + 3y_2^2C_{222})/2\bar{V}_m^2$$

By applying Equation (I-1) to Equation (I-2), the following expression is obtained.

$$\varepsilon_Y^2 = \varepsilon_A^2 + \varepsilon_B^2 + \varepsilon_C^2 + \varepsilon_D^2 + \varepsilon_E^2 + \varepsilon_F^2 \qquad (I\text{-}3)$$

Thus, the problem of determining the error in Y must be subdivided into determining the error associated with each of the terms in Equation (I-2).

Applying Equation (I-1) to the term A of Equation (I-2) yields

$$\varepsilon_A^2 = (\varepsilon_{\phi_2}/\phi_2)^2$$

But there are two errors associated with the quantity ϕ_2, namely, the random error in ϕ_2 and the error in ϕ_2 associated with the error in the composition, y_2, which arises from the calibration of the chromatograph. Therefore,

$$\varepsilon_A^2 = [(\varepsilon_{\phi_2}/\phi_2)^2]_{RANDOM} + [(\varepsilon_{y_2}/y_2)^2]_{CALIB} \qquad (I\text{-}4)$$

The overall random error in ϕ_2 was determined by

(1) fitting the experimental data to Equation (12) using an unweighted least squares regression technique

(2) determining the value of $\phi_2^{EXP} - \phi_2^{CALC}$ from step (1) and assuming this value equal to ε_{ϕ_2}

(3) plotting $(\varepsilon_{\phi_2}/\phi_2)^2$ versus pressure and examining the plot for the overall average value of $(\varepsilon_{\phi_2}/\phi_2)^2$.

The results of this analysis for the helium-krypton and helium-xenon systems are shown in Figures 48 and 49, respectively. Careful examination of these figures shows that there is no apparent pressure or temperature influence on the value of $(\varepsilon_{\phi_2}/\phi_2)^2$.

The error in y_2 (and ϕ_2) which arises from the error in the compositions of the mixtures used to calibrate the chromatograph is derived by examining the equation

$$y_2 = (P_2/Z_2)/(P_m/Z_m) \qquad (I\text{-}5)$$

where

"2" indicates the trace component (krypton or xenon)

"m" indicates the mixture.

Applying Equation (I-1) to Equation (I-5) yields

$$[(\varepsilon_{y_2}/y_2)^2]_{CALIB} = (\varepsilon_{P_2}/P_2)^2 + (\varepsilon_{P_m}/P_m)^2 + (\varepsilon_{Z_2}/Z_2)^2 + (\varepsilon_{Z_m}/Z_m)^2 \qquad (I\text{-}6)$$

The errors in the individual measurements are as follows:

$\varepsilon_Z = \varepsilon_{Z_m}$ ±0.001 (worst case)

ε_{P_m} = ±3 psia (for a 3000 psig Heise gauge)

ε_{P_2} = ±0.1mm Hg = ±0.002 psia (for the T.I. gauge)

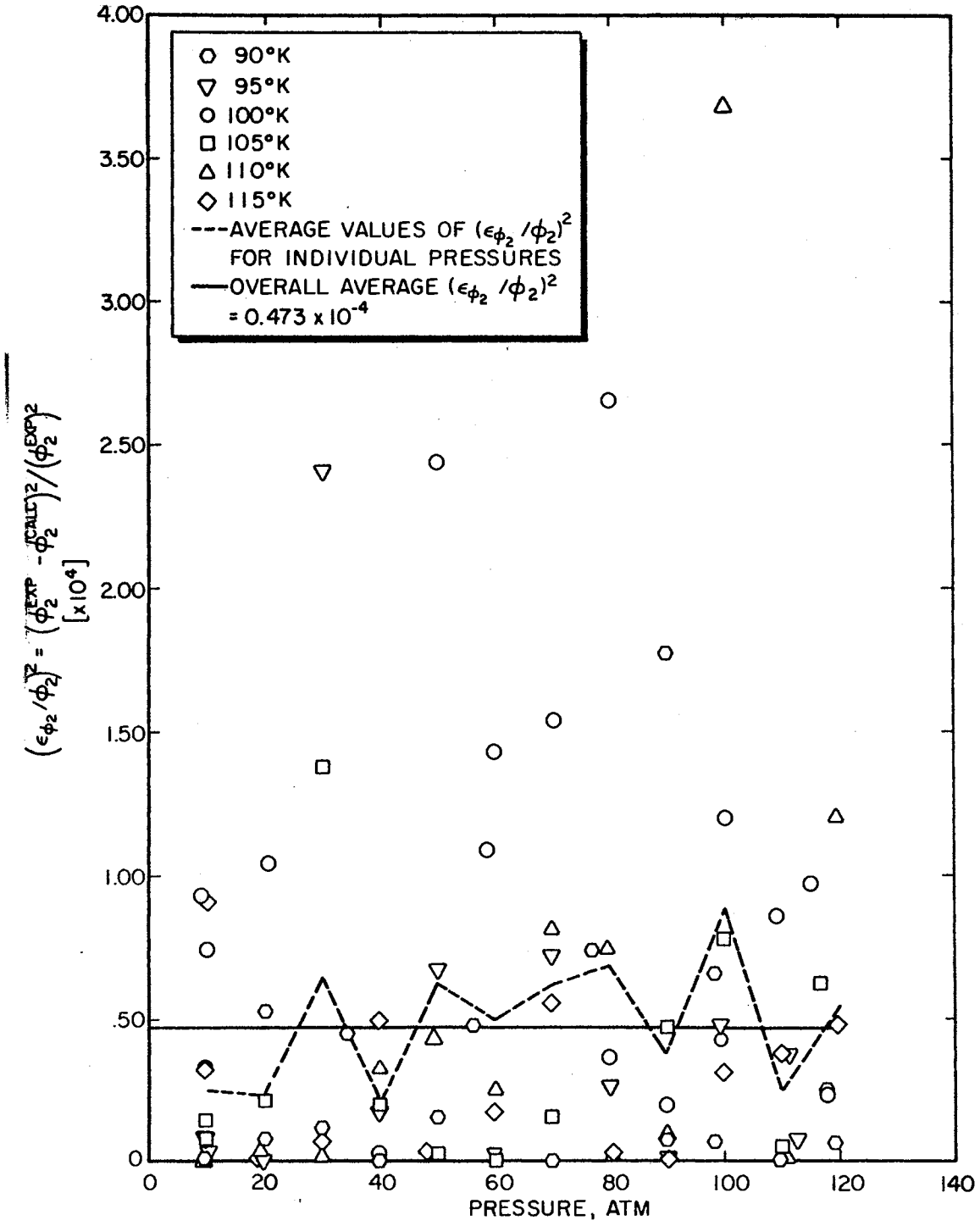

Figure 48. Determination of the Random Error in ϕ_2 from the Experimental Data for the Helium-Krypton System

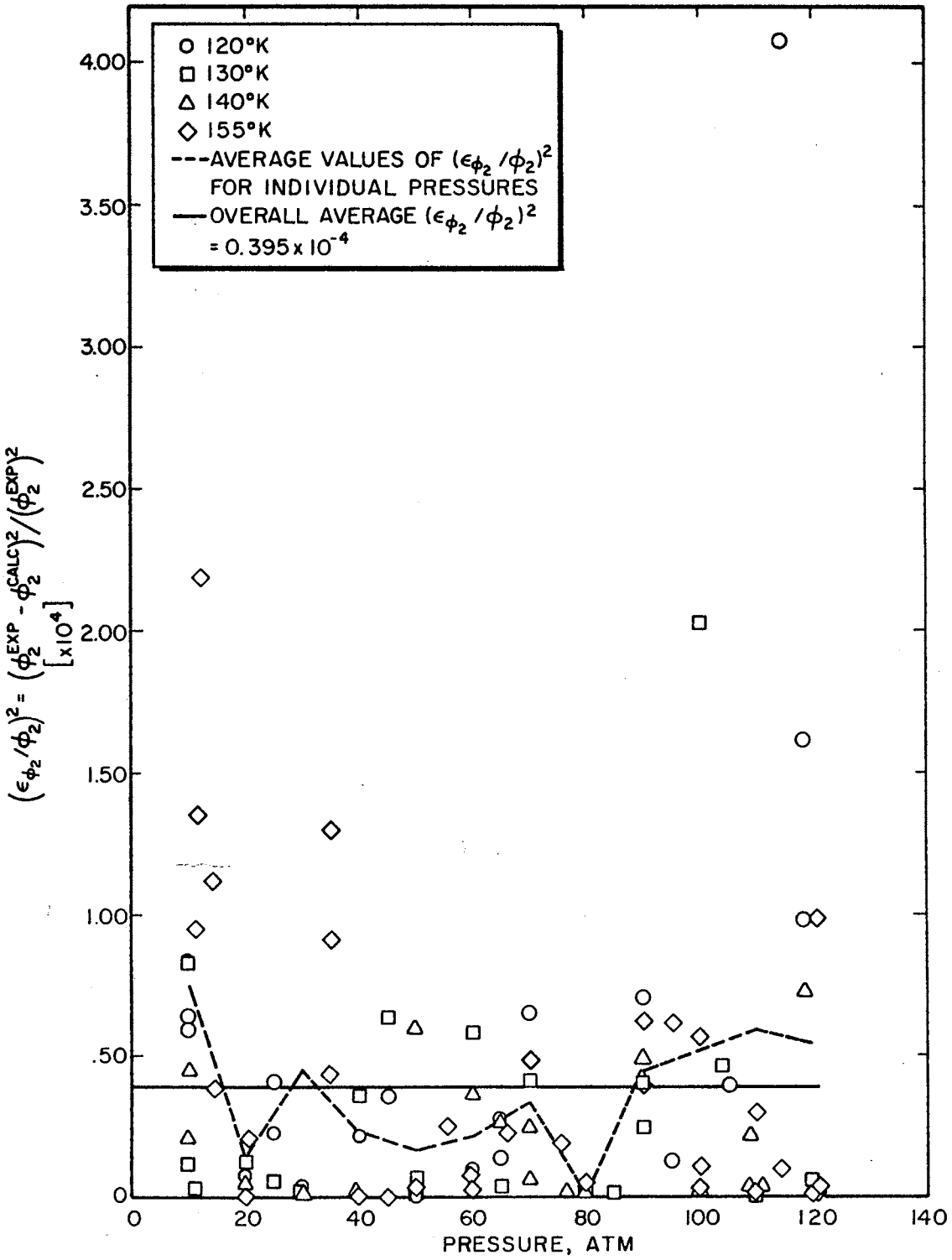

Figure 49. Determination of the Random Error in ϕ_2 from the Experimental Data for the Helium-Xenon System

ε_{p_2} = ±0.12 psia (for the 100 psig Heise gauge).

Because the temperature never varied more than ±0.05° K. in 300° K., the error in the above variables due to temperature errors is negligible.

The values of $[(\varepsilon_{y_2}/y_2)^2]_{CALIB}$ calculated from Equation (I-6) are plotted versus composition (y_2) in Figures 50 and 51 for the helium-krypton and helium-xenon systems, respectively. For mole fractions (y_2) greater than 0.001, the $[(\varepsilon_{y_2}/y_2)^2]_{CALIB}$ values were fitted to a straight line function of y_2 and for mole fractions (y_2) less than 0.001, an average value of $[(\varepsilon_{y_2}/y_2)^2]_{CALIB}$ was determined. These results are given in Figures 50 and 51 and Table XXVI.

Applying Equation (I-1) to the term B of Equation (I-2) yields

$$\varepsilon_B^2 = (\varepsilon_{Z_m}/Z_m)^2 \tag{I-7}$$

The value of Z_m must be determined from the virial equation

$$Z_m = 1 + B_m/\bar{V}_m + C_m/\bar{V}_m^2 + \ldots \tag{I-8}$$

Because Z_m and $\bar{V}_m$ are inter-related, the error in Z_m is assumed to arise only from errors in B_m and C_m. Thus, applying Equation (I-1) to Equation (I-8) gives

$$\varepsilon_{Z_m}^2 = (\varepsilon_{B_m}/B_m)^2 + (\varepsilon_{C_m}/C_m)^2$$

The values of B_m and C_m are determined from Equations (40) and (41). Applying Equation (I-1) to these equations yields

$$\varepsilon_B^2 = y_1^4\varepsilon_{B_{11}}^2 + 4y_1^2y_2^2\varepsilon_{B_{12}}^2 + y_2^4\varepsilon_{B_{22}}^2 \tag{I-9}$$

$$\varepsilon_C^2 = y_1^6\varepsilon_{C_{111}}^2 + 9y_1^4y_2^2\varepsilon_{C_{112}}^2 + 9y_1^2y_2^4\varepsilon_{C_{122}}^2 + y_1^6\varepsilon_{C_{222}}^2 \tag{I-10}$$

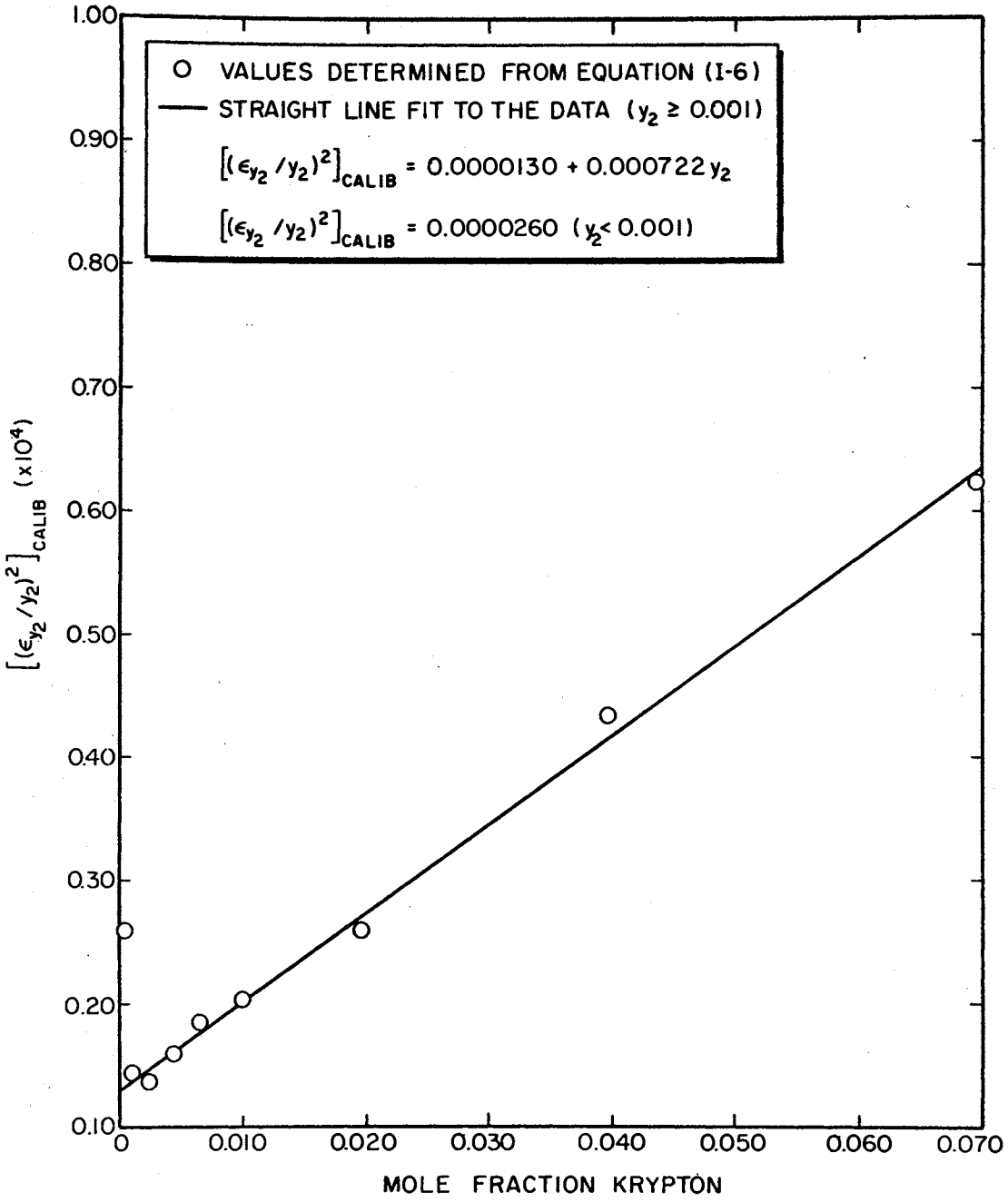

Figure 50. Determination of the Error, $[(\epsilon_{y_2}/y_2)^2]_{CALIB}$, for the Helium-Krypton System

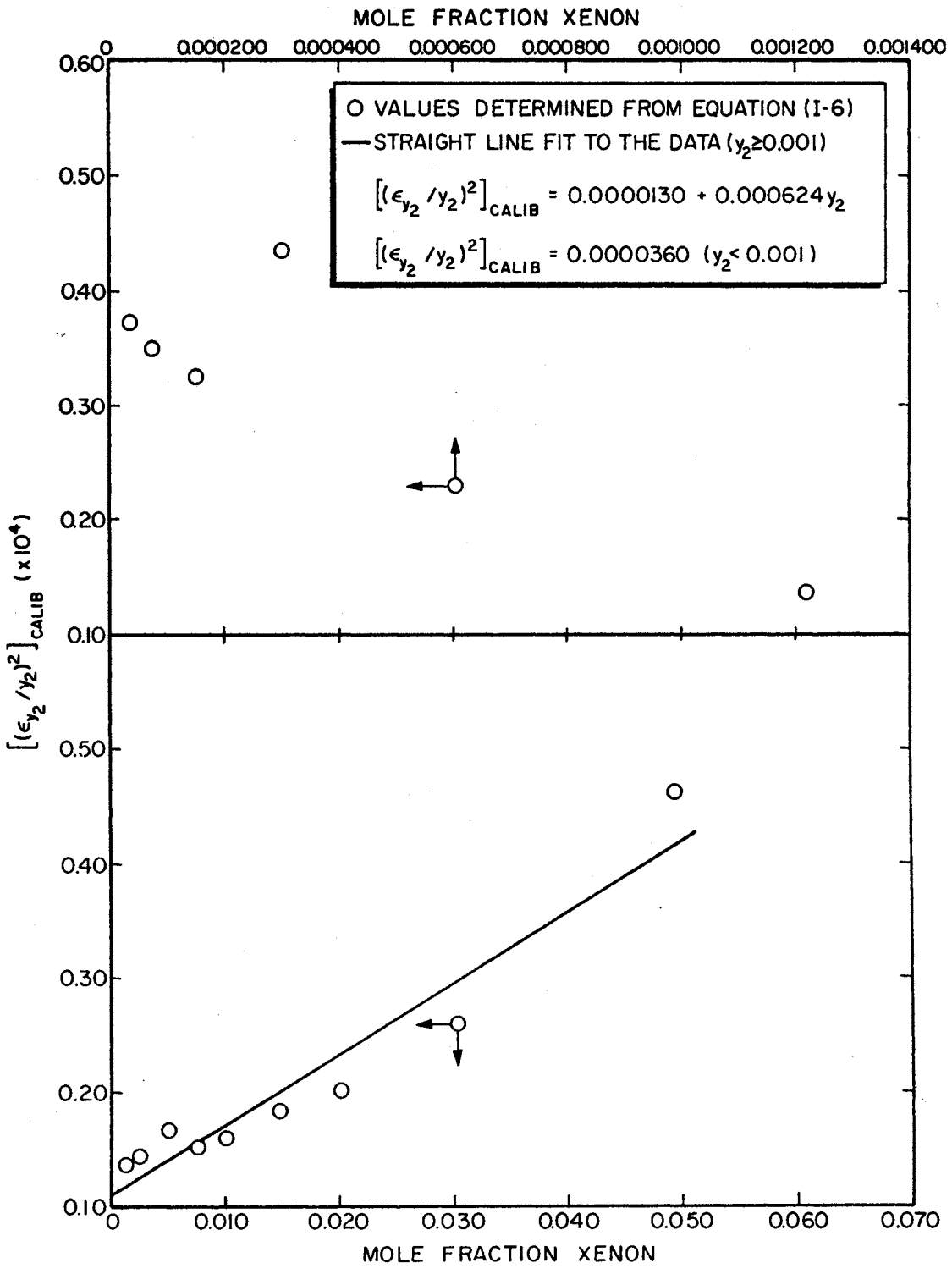

Figure 51. Determination of the Error, $[(\epsilon_{y_2}/y_2)^2]_{CALIB}$, for the Helium-Xenon System

Combining Equations (I-7), (I-8), (I-9), and (I-10) gives

$$\varepsilon_B^2 = [(y_1^4\varepsilon_{B_{11}}^2 + 4y_1^2y_2^2\varepsilon_{B_{12}}^2 + y_2^4\varepsilon_{B_{22}}^2)/\bar{V}_m^2 + (y_1^6\varepsilon_{C_{111}}^2 + 9y_1^4y_2^2\varepsilon_{C_{112}}^2 + 9y_1^2y_2^4\varepsilon_{C_{122}}^2 + y_2^6\varepsilon_{C_{222}}^2)/\bar{V}_m^4]/Z_m^2 \quad \text{(I-11)}$$

Applying Equation (I-1) to term C of Equation (I-2) yields

$$(\varepsilon_C/C)^2 = [(\varepsilon_{\bar{V}_{2S}}/\bar{V}_{2S})^2 + \varepsilon_P^2/(P - P_2^o)^2 + \varepsilon_{P_2^o}^2/(P - P_2^o)^2] \quad \text{(I-12)}$$

where the temperature error term has been ignored because $(\varepsilon_T/T)^2$ is negligible compared to the other error terms. Applying Equation (I-1) to term D of Equation (I-2) gives

$$(\varepsilon_D/D)^2 = (\varepsilon_{B_{22}}/B_{22})^2 + (\varepsilon_{P_2}/P_2)^2 \quad \text{(I-13)}$$

where the temperature error term has again been neglected.

By applying Equation (I-1), the error in term E of Equation (I-2) is given by

$$(\varepsilon_E/E)^2 = (\varepsilon_{y_2}/y_2)^2 + (\varepsilon_{\bar{V}_m}/\bar{V}_m)^2 + (\varepsilon_{B_{22}}/B_{22})^2 \quad \text{(I-14)}$$

where the error term $(\varepsilon_{y_2}/y_2)^2$ is obtained from

$$(\varepsilon_{y_2}/y_2)^2 = [(\varepsilon_{y_2}/y_2)^2]_{\text{RANDOM}} + [(\varepsilon_{y_2}/y_2)^2]_{\text{CALIB}} \quad \text{(I-15)}$$

The term $[(\varepsilon_{y_2}/y_2)^2]_{\text{CALIB}}$ has been discussed previously and the $[(\varepsilon_{y_2}/y_2)^2]_{\text{RANDOM}}$ term was back-calculated from the value of $[(\varepsilon_{\phi_2}/\phi_2)^2]_{\text{RANDOM}}$ and is presented in Table XXVI. At a given pressure and temperature, the value of $\bar{V}_m$ can be obtained directly from the value of Z_m and thus,

$$(\varepsilon_{\bar{V}_m}/\bar{V}_m)^2 \simeq (\varepsilon_{Z_m}/Z_m)^2$$

TABLE XXVI

SUMMARY OF THE ERRORS ASSOCIATED WITH THE EXPERIMENTAL QUANTITIES IN EQUATION (34)

Helium-Krypton System			Helium-Xenon System		
Term	Symbol	Value	Term	Symbol	Value
Random error in ϕ_2	$(\varepsilon_{\phi_2}/\phi_2)^2$	0.0000473	Random error in ϕ_2	$(\varepsilon_{\phi_2}/\phi_2)^2$	0.0000395
Random error in y_2	$[(\varepsilon_{y_2}/y_2)^2]_{RANDOM}$	0.0000200	Random error in y_2	$[(\varepsilon_{y_2}/y_2)^2]_{RANDOM}$	0.0000200
Calibration error in y_2	$[(\varepsilon_{y_2}/y_2)^2]_{CALIB}$	for $y_2 > 0.0010$; $0.0000130 + 0.000722y_2$ for $y_2 < 0.0010$; 0.0000260	Calibration error	$[(\varepsilon_{y_2}/y_2)^2]_{CALIB}$	for $y_2 > 0.0010$; $0.0000130 + .000624y_2$ for $y_2 < 0.0010$; 0.0000360
Error in system	ε_p	±0.204 atm for P > 65 atm ±0.068 atm for 27 < P < 65 ±0.020 atm for p < 27 atm	Same as helium-krypton system		
Error in solid vapor pressure	$(\varepsilon_{P_2^o}/P_2^o)^2$	0.000050	Same as helium-krypton system		
Error in solid molar volume	$(\varepsilon_{\bar{V}_{2S}}/\bar{V}_{2S})^2$	0.000100	Same as helium-krypton system		

TABLE XXVI (CONTINUED)

Helium-Krypton System			Helium-Xenon System		
Term	Symbol	Value	Term	Symbol	Value
Error in krypton second virial	$\varepsilon_{B_{22}}$	±10 cc/g-mole	Error in xenon second virial	$\varepsilon_{B_{22}}$	±25 cc/g-mole
Error in krypton third virial	$\varepsilon_{C_{222}}$	$\pm C_{222}$ (cc/g-mole)^2	Error in xenon third virial	$\varepsilon_{C_{222}}$	$\pm C_{222}$ (cc/g-mole)^2
Error in helium second virial	$\varepsilon_{B_{11}}$	±0.20 cc/g-mole	Same as helium-krypton system		
Error in helium third virial	$\varepsilon_{C_{111}}$	±30(cc/g-mole)^2	Same as helium-krypton system		
Error in helium-krypton second interaction virial	$\varepsilon_{B_{12}}$	±1 cc/g-mole	Error in helium-xenon second interaction virial	Same as helium-krypton system	
Error in helium-krypton third interaction virials	$\varepsilon_{C_{112}}$ $\varepsilon_{C_{122}}$	$\pm C_{112}/2$ $\pm C_{122}/2$ (cc/g-mole)^2	Error in helium-xenon third interaction virials	Same as helium-krypton system	

Finally, applying Equation (I-1) to term F of Equation (I-2) yields

$$\varepsilon_F^2 = [(6y_1y_2C_{112} + 3y_2^2C_{222})/\bar{V}_m^2]^2 \, (\varepsilon_{\bar{V}_m}/\bar{V}_m)^2 + (3y_1y_2/\bar{V}_m)^2\varepsilon_{C_{122}}^2 \quad \text{(I-16)}$$

$$+ (1.5y^2/\bar{V}_m^2)^2\varepsilon_{C_{122}}^2 + (1.5y_2/\bar{V}_m^2)^2[2(1-2y_2)C_{122} + 2y_2C_{222}]^2(\varepsilon_{y_2}/y_2)^2$$

The values of each of the individual experimental errors are summarized in Table XXVI. The information summarized in Table XXVI together with the analysis presented above was used to determine the overall error in the function Y.

At this point, a brief explanation is presented concerning the apparent inconsistency of inserting assumed values for the standard error in B_{12} and C_{112} ($\varepsilon_{B_{12}}$ and $\varepsilon_{C_{112}}$) into the error analysis for ε_Y and then using this value of ε_Y in calculating the standard errors in B_{12} and C_{112} based on the fit of the experimental data to Equation (34). This inconsistency arises from linearizing the non-linear problem associated with fitting experimental data to Equation (34), a technique which was discussed earlier. Fortunately, the problem is resolved by the fact that the values of $\varepsilon_{B_{12}}$ and $\varepsilon_{C_{112}}$ have a negligible effect on the value of ε_Y and thus, the assumed values of $\varepsilon_{B_{12}}$ and $\varepsilon_{C_{112}}$ have a negligible effect on their calculated values.

APPENDIX J

COMPUTER PROGRAM FOR THE REDUCTION OF SOLID-VAPOR EQUILIBRIUM DATA BY LEAST SQUARES REGRESSION

```
      IMPLICIT REAL*8(A-H,O-Z)
      DIMENSION T(10),B11(10),C111(10),B22(10),VO2(10),RT(10),PO2(10),P(
     170),Y2(70),Z(70),DENS(70),ZLN(70),PHI2(70),PHI2LN(70),B(10),C(10),
     2B12(10),Y(70),SQERY(70),B12ASS(10),C112(10),C122(10),C222(10),Y1(7
     30),X(70),SQERA(70),SQERB(70),SQERC(70),SQERE(70),SQERF(70),SQEY2C(
     470),ED(70),FD(70),DEVVP(10)
  100 FORMAT(F10.6,F10.3,I3)
  101 FORMAT(F10.2,F10.4,F10.3,F10.2,F10.3,I3,F10.6)
  102 FORMAT(F10.3,F10.7)
  103 FORMAT(F10.3,3F10.0)
  104 FORMAT(F10.3)
  200 FORMAT(1H1,12HTEMPERATURE=,F7.2,2X,23HKRYPTON VAPOR PRESSURE=,F8.6
     1,2X,27HKRYPTON SOLID MOLAR VOLUME=,F7.3//)
  201 FORMAT(1X,14HITERATION NO.=,I3,3X,32HINTERACTION VIRIAL COEFFICIEN
     1TS:,3X,4HB12=,F9.3,3X,5HC112=,1X,D15.8//50X,5HBDIF=,1X,D15.8,3X,5H
     2CDIF=,1X,D15.8/)
  202 FORMAT(1X,8HPRESSURE,5X,2HY2,6X,4HZMIX,7X,7HDENSITY,11X,4HYEXP,11X
     1,5HYCALC,12X,4HYDEV,11X,6HSQYDEV,5X,7HPHI2EXP,2X,6HPHICLC,3X,4HXEX
     2P/)
  203 FORMAT(1X,F8.3,1X,F9.6,1X,F8.5,1X,D15.8,1X,D15.8,1X,D15.8,1X,D15.8
     1,1X,D15.8,1X,F7.4,1X,F7.4,F9.6/)
  204 FORMAT(1HO,15HSUM OF SQUARES=,1X,D14.8,1H;3X,20HMEAN SUM OF SQUARE
     1S=,1X,D14.8)
  205 FORMAT(1X,8HPRESSURE,6X,5HSQERA,11X,5HSQERB,11X,5HSQERC,11X,5HSQER
     1D,11X,5HSQERE,11X,5HSQERF,11X,5HSQERY,9X,3HERY/)
  206 FORMAT(1X,F8.3,1X,D15.8,1X,D15.8,1X,D15.8,1X,D15.8,1X,D15.8,1X,D15
     1.8,1X,D15.8,1X,F9.6/)
  207 FORMAT(1HO,32HESTIMATED STANDARD ERROR OF B12=,1X,D15.8,1H;,33HEST
     1IMATED STANDARD ERROR OF C112=,1X,D15.8//24H ROOT MEAN SQUARE ERRO
     2R=,1X,D15.8)
      READ(5,100) A,XB,NT
      DO 10 I=1,NT
      READ(5,101) T(I),B11(I),C111(I),B22(I),VO2(I),NP,PO2(I)
      READ(5,103) B12ASS(I),C112(I),C122(I),C222(I)
      RT(I)=82.0567*T(I)
      VO2DM=VO2(I)/RT(I)
      B22DM=B22(I)*PO2(I)/RT(I)
      SQEVPT=0.000050
      SQESVT=0.00010
      SQERD=(625.0/B22(I)**2+SQEVPT)*B22DM**2
      WRITE(6,200) T(I),PO2(I),VO2(I)
      DO 20 J=1,NP
      READ(5,102) P(J),Y2(J)
      Y1(J)=1.0-Y2(J)
      IF(P(J).GT.65.0) GO TO 21
      IF(P(J).LT.27.0) GO TO 22
      ERP=0.068
      GO TO 25
   21 ERP=0.204
      GO TO 25
   22 ERP=0.020
   25 IF(Y2(J).LT.0.001) GO TO 26
      SQEY2C(J)=0.0000130+0.000624*Y2(J)
      GO TO 27
```

```
26 SQEY2C(J)=0.0000360
27 SQERA(J)=0.0000395+SQEY2C(J)
   SQERC(J)=(SQESVT+(ERP/(P(J)-PO2(I)))**2+(PO2(I)/(P(J)-PO2(I)))**2*
  1SQEVPT)*(VO2DM*(P(J)-PO2(I)))**2
20 CONTINUE
   DO 60 K=1,10
31 SUMX2=0.0
   SUMX3=0.0
   SUMX4=0.0
   SUMXY=0.0
   SUMX2Y=0.0
   DO 40 J=1,NP
   BM=Y1(J)*Y1(J)*B11(I)+2.0*Y1(J)*Y2(J)*B12ASS(I)+Y2(J)*Y2(J)*B22(I)
   BP=BM/RT(I)
   CM=Y1(J)**3*C111(I)+3.0*Y1(J)**2*Y2(J)*C112(I)+3.0*Y1(J)*Y2(J)**2*
  1C122(I)+Y2(J)**3*C222(I)
   CP=(CM-BM*BM)/RT(I)**2
   Z(J)=1.0+BP*P(J)+CP*P(J)**2
   DENS(J)=P(J)/(Z(J)*RT(I))
   X(J)=Y1(J)*DENS(J)
   PHI2(J)=Y2(J)*P(J)/PO2(I)
   ZLN(J)=DLOG(Z(J))
   PHI2LN(J)=DLOG(PHI2(J))
   SQERB(J)=((0.04*Y1(J)**4+4.0*(Y1(J)*Y2(J))**2+625.*Y2(J)**4)*DENS(
  1J)**2+(400.*Y1(J)**6+2.25*Y1(J)**4*Y2(J)**2*C112(I)**2+2.25*Y1(J)*
  2*2*Y2(J)**4*C122(I)**2+Y2(J)**6*C222(I)**2)*DENS(J)**4)/Z(J)**2
   E=2.0*Y2(J)*DENS(J)*B22(I)
   ED(J)=E
   SQERE(J)=(0.000020+SQEY2C(J)+SQERB(J)+625.0/B22(I)**2)*E**2
   F=1.5*DENS(J)**2*(2.0*Y1(J)*Y2(J)*C122(I)+Y2(J)**2*C222(I))
   FD(J)=F
   DENSDS=(1.5*DENS(J)**2)**2
   SQERF(J)=4.0*F**2*SQERB(J)+DENSDS*((Y1(J)*Y2(J))**2*C122(I)**2+Y2(
  1J)**4*C222(I)**2)+DENSDS*Y2(J)**2*(2.0*(1.0-2.0*Y2(J))*C122(I)+2.0
  2*Y2(J)*C222(I))**2*(0.000020+SQEY2C(J))
   SQERY(J)=SQERA(J)+SQERB(J)+SQERC(J)+SQERD+SQERE(J)+SQERF(J)
   Y(J)=PHI2LN(J)-ZLN(J)-B22DM-VO2DM*(P(J)-PO2(I))+E+F
   SUMX2=SUMX2+X(J)**2/SQERY(J)
   SUMX3=SUMX3+X(J)**3/SQERY(J)
   SUMX4=SUMX4+X(J)**4/SQERY(J)
   SUMXY=SUMXY+X(J)*Y(J)/SQERY(J)
   SUMX2Y=SUMX2Y+X(J)**2*Y(J)/SQERY(J)
40 CONTINUE
   SUMDM=SUMX4*SUMX2-SUMX3*SUMX3
   B12CLC=(SUMX3*SUMX2Y-SUMX4*SUMXY)/SUMDM
   C112CL=(SUMX3*SUMXY-SUMX2*SUMX2Y)/SUMDM
   BDIF=DABS(B12ASS(I)-B12CLC/2.0)
   CDIF=DABS(C112(I)-C112CL/1.5)
   IF(BDIF.LT.0.0001.AND.CDIF.LT.1.0) GO TO 61
   B12ASS(I)=B12CLC/2.0
   C112(I)=C112CL/1.5
60 CONTINUE
   K=11
61 BDM=B12CLC/2.0
```

```
      C0M=C112CL/1.5
      WRITE(6,201) K,B0M,C0M,B0IF, C0IF
      WRITE(6,205)
      DO 50 J=1,NP
      ERY=SQERY(J)**0.5
      WRITE(6,206) P(J),SQERA(J),SQERB(J),SQERC(J),SQERD,SQERE(J),SQERF(
     1J),SQERY(J),ERY
   50 CONTINUE
      WRITE(6,202)
      SUMSQ=0.0
      DO 30 J=1,NP
      YCALC=-1.0*B12CLC*X(J)-C112CL*X(J)**2
      YDEV=Y(J)-YCALC
      SQYDEV=YDEV**2/SQERY(J)
      SUMSQ=SUMSQ+SQYDEV
      PHICLN=YCALC+ZLN(J)+B22DM+V02DM*(P(J)-P02(I))-ED(J)-FD(J)
      PHICLC=DEXP(PHICLN)
      PHIDEV=PHI2(J)-PHICLC
      WRITE(6,203) P(J),Y2(J),Z(J),DENS(J),Y(J),YCALC,YDEV,SQYDEV,PHI2(J
     1),PHICLC,X(J)
   30 CONTINUE
      XNP=NP
      XNPDM=NP-2
      XMSSQ=SUMSQ/XNP
      STSQE=SUMSQ/XNPDM
      ESEB12=(SUMX4*STSQE/SUMDM)**0.5
      SEC112=(SUMX2*STSQE/SUMDM)**0.5
      RMSER=STSQE**0.5
      WRITE(6,204) SUMSQ,XMSSQ
      WRITE(6,207) ESEB12,SEC112,RMSER
   10 CONTINUE
      CALL EXIT
      END
```

APPENDIX K

EFFECT OF THE PARAMETERS IN EQUATION (34) ON THE REGRESSED VALUES OF B_{12}

The effect of the parameters in Equation (34) on the regressed values of B_{12} was determined by changing the value of each variable by an incremental amount and noting the effect on the B_{12} values. The vapor pressure and solid molar volume were varied by ±2%. The value of B_{22} was varied by ±5% and the value of B_{11} was varied by ±1%. These incremental changes are all larger than the assumed imprecision of the individual variables and should give a good test of the effect of each variable on B_{12}.

The results of this analysis are presented in Table XXVII. These results indicate that the only variable that has any significant effect on the value of B_{12} is the vapor pressure. A two percent change in the vapor pressure gives rise to a change in B_{12} of approximately 3 cc/g-mole, whereas the effects on B_{12} upon incrementing any of the other variables are all less than 0.5 cc/g-mole. This is well within the stated imprecision of the regressed B_{12} values of ±1 cc/g-mole. The effect of the variables, C_{111} and C_{222}, on the values of B_{12} were not tested because B_{11} and B_{22} had no significant effect on B_{12} and C_{222} should have even less effect.

TABLE XXVII

EFFECT OF CERTAIN PARAMETERS IN EQUATION (34) ON THE REGRESSED VALUE OF B_{12} FOR THE HELIUM-KRYPTON SYSTEM

Temperature = 90° K.		Temperature = 115° K.	
Vapor Pressure atm.	B_{12} cc/g-mole	Vapor Pressure atm.	B_{12} cc/g-mole
0.02600	-2.246	0.6548	3.953
0.02653*	0.853	0.6682*	7.502
0.02706	3.890	0.6816	10.970
B_{11} cc/g-mole	B_{12} cc/g-mole	B_{11} cc/g-mole	B_{12} cc/g-mole
11.03	0.800	11.75	7.446
11.14*	0.853	11.87*	7.502
11.25	0.916	11.99	7.558
Solid Molar Volume cc/g-mole	B_{12} cc/g-mole	Solid Molar Volume cc/g-mole	B_{12} cc/g-mole
28.338	0.572	29.050	7.202
28.916*	0.853	29.643*	7.502
29.494	1.134	30.236	7.802
B_{22} cc/g-mole	B_{12} cc/g-mole	B_{22} cc/g-mole	B_{12} cc/g-mole
-588.46	0.871	-351.89	7.739
-560.44*	0.853	-335.13*	7.502
-532.42	0.835	-318.37	7.265

*Experimental value

NOMENCLATURE

A	=	attractive potential term constant
A, B	=	constants in Equation (42)
A,B,C,D,E,F	=	dummy variables in Equation (I-2)
B	=	second virial coefficient (Leiden form)
B'	=	second virial coefficient (Berlin form)
B_{12}	=	second interaction virial coefficient
B_I, B_{II}, B_o	=	quantum corrections to the second virial coefficient
B, C	=	constants in Equation (35)
C	=	repulsive potential term constant
C	=	third virial coefficient (Leiden form)
C'	=	third virial coefficient (Berlin form)
C_{112}, C_{122}	=	third interaction virial coefficients
C_P	=	molar heat capacity
c	=	velocity of light
c_1	=	velocity of light in an unmoving gas
D	=	gas diffusion coefficient
E	=	excess virial coefficient
ERT	=	term defined by Equation (15)
F	=	term in Equation (16)
f	=	frequency of a sound wave
f	=	pure component fugacity
$\hat{f}$	=	fugacity of a component in a mixture
h	=	Planck's constant

I = ionization potential

k = empirical parameter in combination Rule VIII

k = Boltzmann's constant

k_{ij} = geometric mean correction factor defined by Equation (30)

M = molecular weight

m = electronic mass

m, n = exponents in empirical potential form [Equation (17)]

$\tilde{N}$ = Avagadro's number

n = number of moles

P = pressure

P^o = vapor pressure

P_{oe} = optimum extrapolation pressure

R = universal gas constant

r = distance

T = temperature

$U(r)$ = intermolecular potential

V = volume

$\bar{V}$ = molar volume

v_g = gas flow rate through ultrasonic detector cell

X, Y = variables in Equation (35)

y = mole fraction

Z = compressibility factor

Greek Symbols

α = static polarizability

β = constant in Equation (43)

χ = diamagnetic susceptibility

Δ = change in a quantity

ε = intermolecular potential energy parameter

ε = error in a quantity

γ = ratio of the constant pressure heat capacity to the constant volume heat capacity

Λ = quantum correction parameter

μ = reduced mass

$\Omega^{(1,1)}$ = collision integral

ϕ = enhancement factor

ρ = density

$\sum$ = summation sign

σ, σ_o = intermolecular potential distance parameters

Θ = phase angle

Subscripts

calc = calculated value

exp = experimental value

ij = interaction of molecules i and j

m = mixture property

s = solid

tp = triple point

v = vapor

1 = component "1" property

2 = component "2" property

Superscripts

* = reduced quantity

exp = experimental quantity

calc = calculated quantity

Miscellaneous

log	=	logarithm
ℓn	=	natural logarithim
∂	=	partial operator
$\equiv$	=	identity sign, denotes a definition
$\simeq$	=	approximately equal to
∞	=	infinity
$\lvert\ \rvert$	=	absolute value sign
$\int$	=	integral sign

VITA

Frederick Henry Kate, Jr.

Candidate for the Degree of

Doctor of Philosophy

Thesis: THE STUDY OF SOLID-VAPOR EQUILIBRIUM IN THE HELIUM-KRYPTON AND HELIUM-XENON BINARY SYSTEMS

Major Field: Chemical Engineering

Biographical:

Personal Data: Born in Centralia, Illinois, December 9, 1942, the son of Frederick H. and Lois M. Kate; married Martha Ann Boettger, December 26, 1965.

Education: Attended elementary school in Oklahoma City, Oklahoma; graduated from Putnam City High School in 1960; received the Bachelor of Science degree from Oklahoma State University, with a degree in Chemical Engineering in May, 1966; received the Master of Science degree in Chemical Engineering from Oklahoma State University in May, 1968; completed the requirements for the Doctor of Philosophy degree in May, 1972.

Professional Experience: Employed as a research engineer by Continental Oil Company during the summer of 1965. Employed as a technical service engineer by Monsanto Company during the summer of 1966. Presently employed by E. I. du Pont de Nemours Company as an engineer in research and development.